POLITECNICO DI MILANO

Facoltà di Ingegneria Industriale

Corso di Laurea in
Ingegneria Energetica

Experimental and Numerical Investigation of Confined Parallel Jets

Advisor: Prof. Fabio Inzoli

Co-Advisor: Ing. Riccardo Mereu

Tesi di Laurea di:

Matteo Rivolta Matr. 784375

Anno Accademico 2012 - 2013

"Penso infatti che Dio ci abbia dato, per una buona ragione, l'amore per certi luoghi speciali, per un focolare e per una terra natia. [...] Voglio dire che se c'è una casa per me in Cielo, questa avrà un lampione verde e una siepe, o qualcosa di concreto e inequivocabile come un lampione verde e una siepe. Quello che voglio dire è che Dio mi ha offerto di amare e servire un determinato luogo, e che mi ha fatto fare, per onorare questo luogo, un sacco di cose… diciamo così… bizzarre, in modo che io potessi testimoniare, contro tutti gli infiniti e contro tutti i sofismi, che il Paradiso è in un certo luogo, e non dovunque, e che è qualcosa di preciso e non qualsiasi cosa. E io, dopo tutto questo, non sarei affatto sorpreso di scoprire che, se dovesse esserci una casa in cielo per me, questa dovrebbe avere davvero un lampione verde"

G. K. Chesterton

Alla mia famiglia, a Michela, ai miei cugini, a tutti i miei cari amici

e soprattutto a Nostro Signore che ha messo in piedi la baracca…

INDEX

Introduction 1

1. Experimental and numerical review on free and confined jets 5

   1.1. Free round jet 5
   1.2. Role of confinement in entrainment phenomenon 13
   1.3. Wall-Jet interaction: Coanda effect on an offset wall 15
   1.4. Jet-Jet interaction: multiple parallel jets 18
   1.5. Numerical approach on jets simulation 25
   1.6. Symmetry breaking and oscillation in jets phenomena 27

2. Experimental techniques and numerical approaches 31

   2.1. LDV technique and Laser System 31
   2.2. Procedure and parameters for laser system 33
   2.3. Error estimation for average velocity and turbulence 35
   2.4. Alignment operations 38
   2.5. Numerical approach 39
      2.5.1. RANS models
      2.5.2. Large Eddy Simulation

3. Physical and numerical problem setting 49

   3.1. Facility structures 49
   3.2. Plenum parameters 50
   3.3. Numerical domain 54

4. Results 57

   4.1. Notation 57
   4.2. Uncertainty 58
   4.3. Symmetry, stability and merging 59

4.4. Oscillations 72
4.5. Experimental VS. Numerical 73

5. Conclusions 99

References 101

ABSTRACT

Free and confined jets are phenomena largely used in many engineering applications: turbogas engine combustors, ejectors in fuel cell/microturbine hybrid cycles, cooling systems for turbine blades or, in general, heat exchangers.

The aim of this thesis is to investigate the fluid dynamics behavior of a confined parallel jets flow map, in order to carry out the most important characteristics, such as velocity decay and spreading ratio.

In order to reach this goal, an experimental campaign and a series of numerical simulations (CFD) was performed.

The results have shown a completely stable and symmetric flow map. The spectra analysis has shown no oscillations. No deflection of jets was detected.

The velocity decay resulted to be higher than in case of a non confined single jet.

Concerning the numerical simulation, LES method has shown very good results in terms of velocity and turbulence. Regarding Rans models, only RSM seemed to predict satisfactorily the behavior of the flow map, although the fluctuation results have shown a large diffusivity.

SOMMARIO

Questo lavoro ha come obiettivo quello di studiare il campo fluidodinamico di una configurazione a cinque getti paralleli e in seguito confrontarli con i risultati ottenuti tramite simulazioni CFD svolte con l'utilizzo del codice commerciale ANSYS Fluent. La geometria è rappresentata nei seguenti schemi (Figura (1))

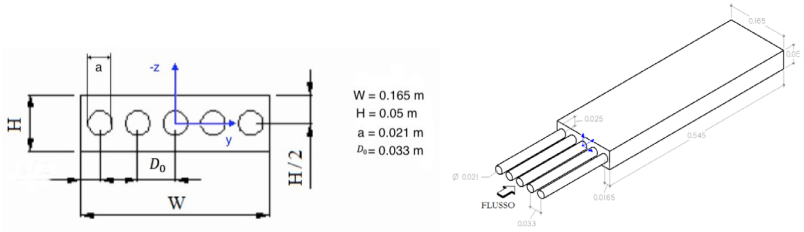

Figura 1 Geometria

I parametri termofisici e le condizioni operative, che sono stati utilizzati anche per la definizione del problema numerico sono riportati nella seguente tabella.

Fluido	*Acqua*	
Temperatura	*20*	*°C*
Viscosità dinamica	*0,001*	$Kg/m \cdot s$
Velocità media nel pipe	*0,48*	m/s
Diametro del pipe	*0,021*	m
Densità	*998*	Kg/m^3

Lo studio si è quindi suddiviso in due parti principali. Nella prima è stata svolta la campagna sperimentale di misura tramite tecnica Laser doppler velocimetry su un modello, in parte in vetro ottico, della geometria desiderata.

Gli obiettivi fondamentali di questa prima fase sono:

1. Verificare che i getti non vengano deflessi in qualche direzione preferenziale per avere una distribuzione uniforme di portata all' interno della camera.

2. Verificare la simmetria della mappa di flusso rispetto agli assi di simmetria geometrici del sistema. Questo permetterebbe di impostare problemi numerici con geometrie semplificate che rappresentano solo la simmetria minima del sistema (un quarto di getto) con condizioni al contorno di tipo periodico.
3. Verificare che non vi siano fenomeni di oscillazione periodica.
4. Verificare la stabilità della mappa di flusso verificando che il sistema fluidodinamico fosse sempre il medesimo in ogni singola sessione sperimentale.
5. Stimare il decadimento della velocità nella direzione del flusso durante il fenomeno di mescolamento dei getti.

L'apparato sperimentale è stato settato in modo da garantire due condizioni fondamentali: la circolazione dell' acqua in modo che la portata sia equi distribuita tra i tubi e il degassaggio dell' acqua stessa per evitare la formazione di bolle che distorcerebbero i fasci laser facendo perdere di valore le misure ottenute.

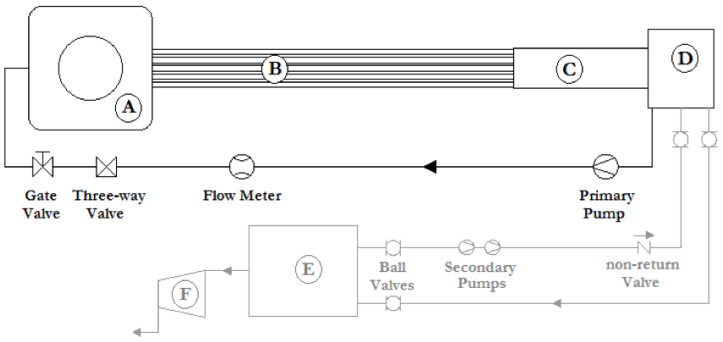

Figura 2 Facility

La facility (Figura 2) è costituita da due circuiti, uno atto alla circolazione, l'altro al degassaggio. Il primo, il circuito principale che è approssimativamente a pressione atmosferica, tramite una pompa da 25 W, genera la circolazione. Attraverso un distributore presente nel serbatoio (A), l'acqua è equi distribuita e viene convogliata al plenum di vetro dove avvengono le misure.
Il circuito secondario è collegato a un serbatoio (E) che è mantenuto a pressione sub-atmosferica. Esso preleva acqua dal primario sfruttando il ΔP e la reimmette nel circuito tramite delle pompe ausiliarie. In questo passaggio, l' acqua essendo a pressione sub-atmosferica rilascia una parte sufficiente di gas per l' equilibrio chimico.

Nella seconda parte del lavoro sono state svolte una serie di simulazioni con i modelli qui riportati.

- $k-\omega\ SST$
- $k-\varepsilon\ RNG$
- V^2f
- $k-\varepsilon\ Low\ Reynolds\ Lam-Bremhorst$
- $k-\varepsilon\ Low\ Reynolds\ Launder-Sharma$
- $k-\varepsilon\ Realizable$
- $Non-Linear\ model\ performed\ by\ Politecnico\ di\ Milano$
- $Reynolds\ Stress\ Model$
- $Large\ eddy\ simulation$

L'obiettivo di questa seconda parte è di verificare le performance dei seguenti modelli implementati da ANSYS e verificare le prestazioni della simulazione Large eddy per verificare se il maggiore costo computazionale era giustificato da una rappresentazione più precisa dello sviluppo del fenomeno fluidodinamico.

I risultati sperimentali hanno mostrato che:

1. I getti non sono deflessi in direzioni preferenziali ma ognuno ha uno sviluppo uguale all' altro (Figura 3 e 4).
2. La mappa di flusso non ha mostrato asimmetrie apprezzabili, ovvero superiori alle incertezze di misura.

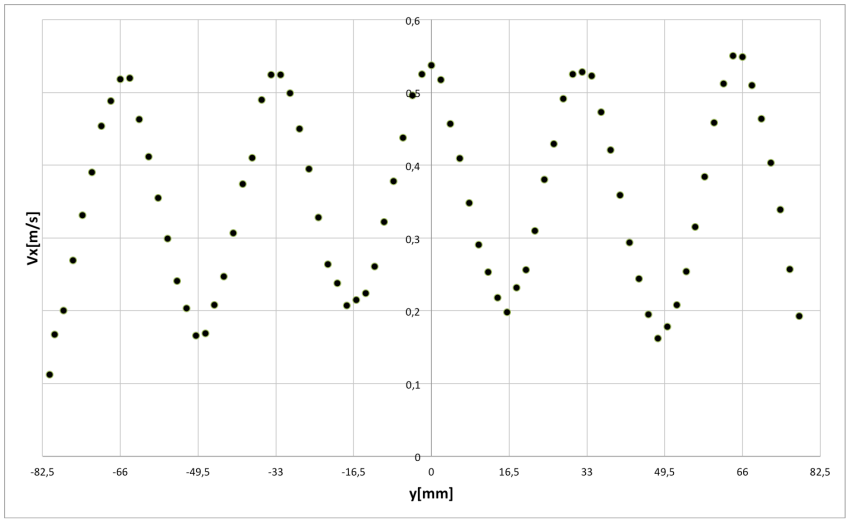

Figura 3 Vx at 5D

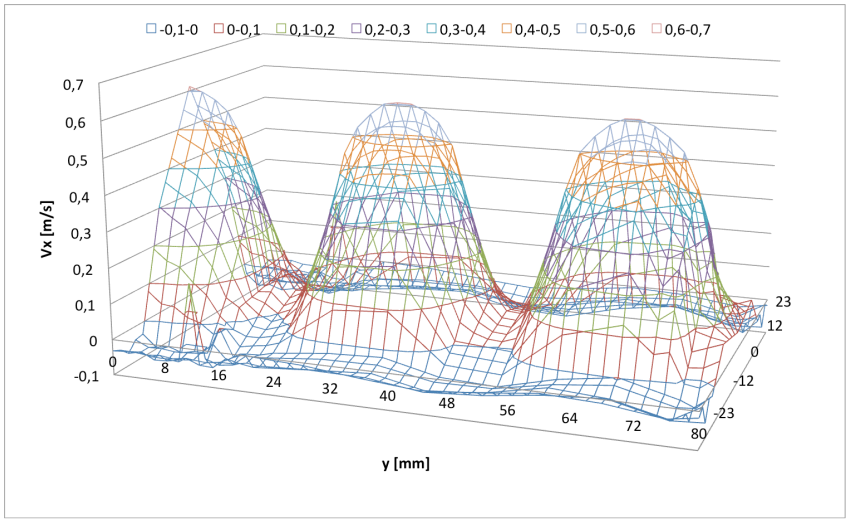

Figura 4 Vx at 1D

3. Un' analisi in frequenza (Figura 5) in vari punti ha mostrato che almeno fino alla soglia di 50 Hz non vi sono fenomeni periodici. Questo risultato va paragonato con una frequenza attesa di oscillazione per le scale integrali del sistema di 25 Hz.

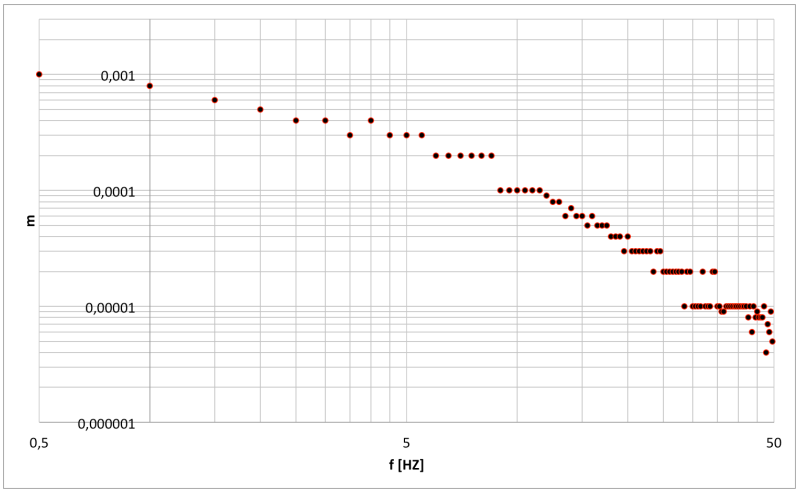

Figura 5 Spectral Analysis

4. Il sistema si è mostrato stabile dal momento il monitoraggio di alcuni punti precedentemente stabiliti ha mostrato le medesime stime delle velocità e turbolenze in sessioni di misura differenti.
5. Si è stimato un decadimento che segue la legge iperbolica

$$\frac{U_i}{U_c(x)} = \frac{1}{K}\left(\frac{x - x_0}{a}\right)$$

con U_i, velocità di picco all' ingresso, $U_c(x)$ velocità sulla linea centrale del getto, x coordinata nella direzione del flusso, a diametro del pipe e x_0 origine virtuale del decadimento.
Il valore ottenuto è $K = 68{,}42$.

I risultati numerici hanno mostrato che *RSM* e *Les* replicano molto correttamente i risultati delle velocità (Figura 5).

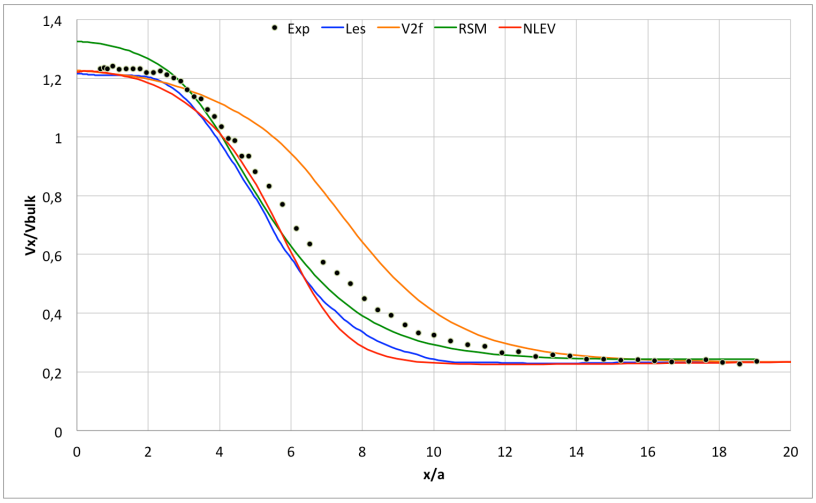

Figura 4 Velocity Decay

Per quanto riguarda le turbolenze la simulazione Large eddy ottiene dei buoni risultati almeno fino a cinque diametri di distanza dall' ingresso (Figura 6 e 7).

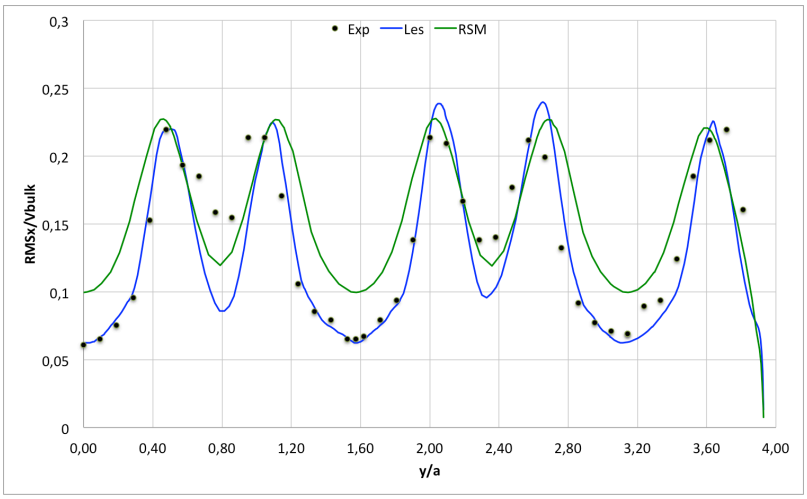

Figura 5 Turbolenza a 1D

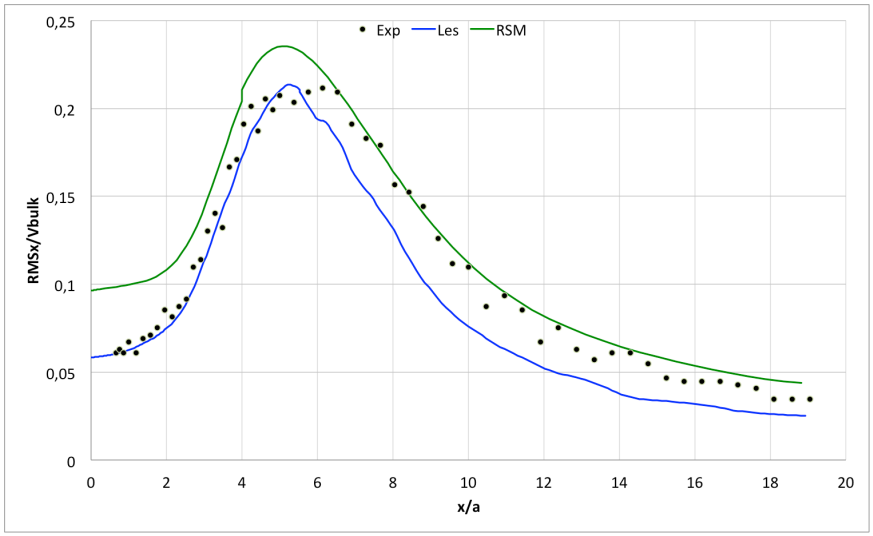

Figura 6. Turbolenza sulla linea centrale del getto

La possibile spiegazione dell'errata riproduzione delle turbolenze potrebbe essere ricercata nella riproduzione non sufficientemente accurata delle strutture coerenti oltre a una certa distanza dall'inlet (Figura 8)

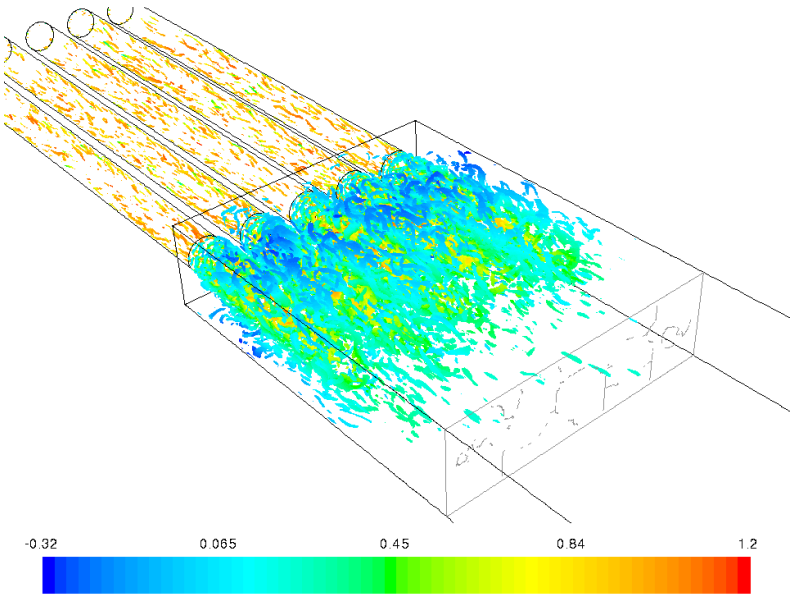

Figura 7. Strutture coerenti nella simulazione LES

Introduction

Free and confined jets are phenomena largely used in many engineering applications: turbogas engine combustors, ejectors in fuel cell/microturbine hybrid cycles, cooling systems for turbine blades or, in general, heat exchangers.

Even if jets are present in many industrial applications, further investigations are necessary in order to fully understand the interaction of confined parallel jets configuration. The spatial periodicity and uniform distribution of the fluid dynamics is, indeed, a mandatory condition to reduce the pressure drop, increase the mixing, and obtain a uniform and homogeneous heat transfer over the whole surface, improving the exchanger performance.

This work is part of an international project in which CFDLab@Energy group of the Department of Energy (Politecnico di Milano) was in charge of analyzing the fluid dynamics of IRIS, a new generation modular nuclear reactor. Specifically, the analysis of confined parallel jets behavior is related to the downcomer structure, composed by an annular array of parallel pipes, pouring the cooling fluid into an annulus, as shown in Figure (1).

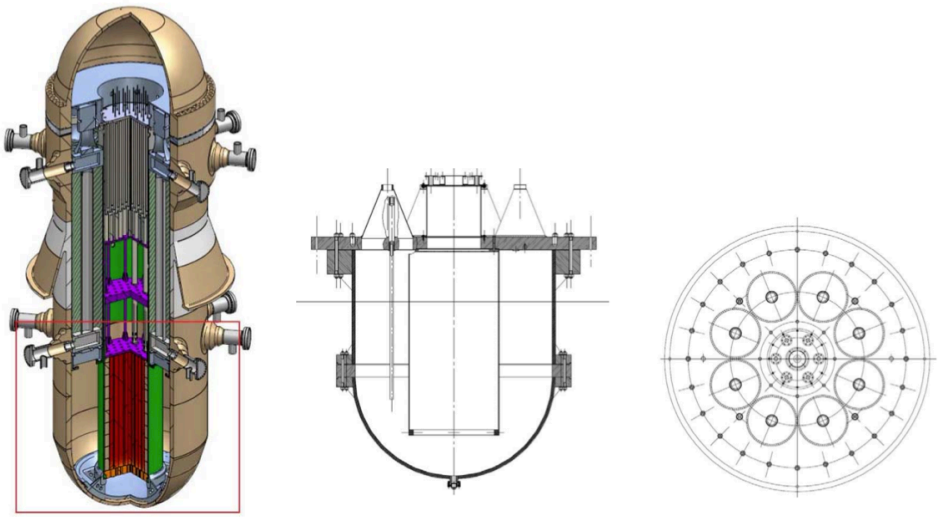

Figure 1. IRIS internal view, frontal and top view of the reactor with annular disposition of pipes

The principal goals of this analysis are:

- to deeply understand the flow map of confined parallel jets in order to define the performance of the analyzed geometrical configuration
- to validate the numerical approaches

This implies a study of the interaction between jets and the interaction between jets and walls, in order to observe the presence of possible fluid dynamics instabilities and asymmetries.

To reach these goals two strategies are adopted: an experimental measurements campaign, and a Computational Fluid Dynamics (CFD) analysis, using the ANSYS Fluent code.

In order to carry out experimental measurements, an unlimited-like array of jets is used, instead of the original annular disposition. This is due to the difficulties in using the LDV (Laser Doppler Velocimetry) technique with non-planar surfaces.

In order to reproduce this kind of configuration, avoiding the direct influence of the side walls on the central jets, an experimental five-parallel-pipe facility has been realized, as shown in Figure (2).

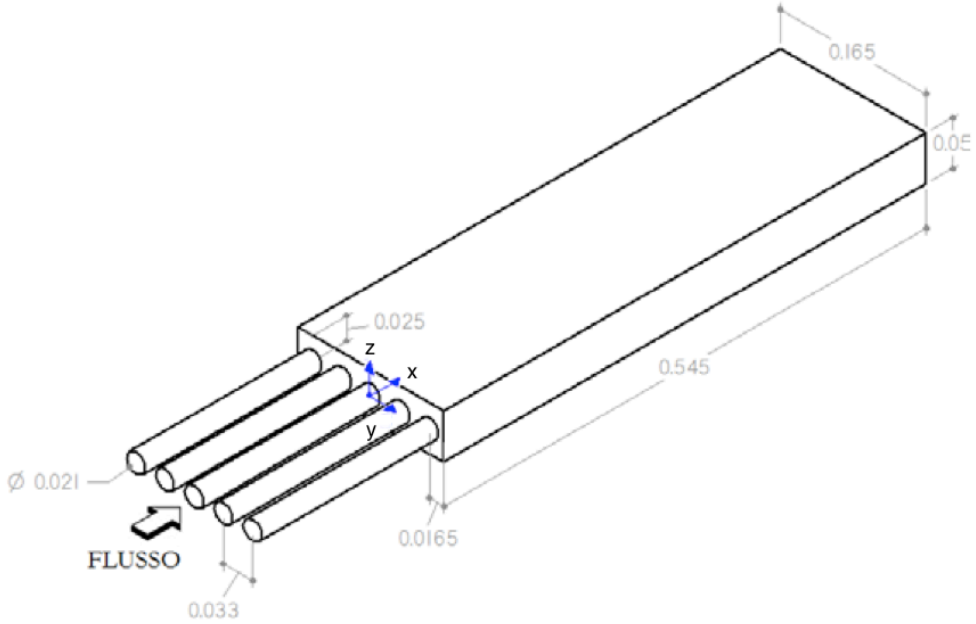

Figure 2. System geometry (cm)

In the first part of this work, the concept of free round jet and confined parallel round jets is briefly presented via an historical review of both experimental and numerical approaches. The second part presents the experimental and numerical techniques, while in the third part are reported the description of the experimental facility and its numerical modeling. Finally, in the last part the analysis of obtained results and conclusions are presented.

1. Experimental and Numerical review on free and confined jets

This chapter reports an overview about free and confined jet studies analyzing the peculiarities of free round, jet-wall interaction, jet-jet interaction, examining phenomena such as oscillations and symmetry breaking.

1.1. FREE ROUND JET

Free jet is a flow entering in a semi-infinitive three-dimensional space through an orifice, (Figure (1.1)).

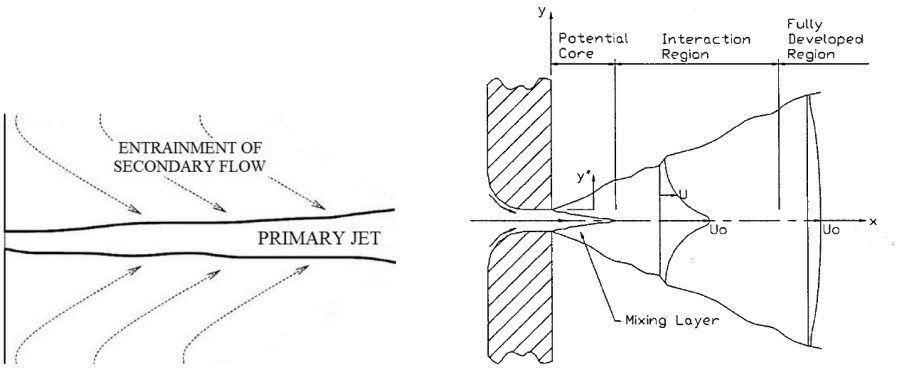

Figure 1.1 Representation of free jet (left) and related regions (right)

Despite the several works presented on this theme, many aspects still remain to be clarified. This is testified by scientific papers published in the last years about this argument (*1-4*). As shown in Figure (1.1) the jet, flowing into the unlimited plenum, drags on the surrounding fluid due to the viscous effect. The jet grows carrying more and more fluid, through the phenomenon called entrainment. From a mathematical point of view this is related to the diffusion term of momentum equation, which is proportional to the gradient of velocity.

The characteristic variables of this phenomenon are: the pipe diameter a, the cinematic viscosity of the fluid ν, and the bulk velocity of the fluid V_{bulk} (if the velocity profile in the pipe is fully developed). The only integral characteristic number of the flow is a combination of these parameters: the diameter Reynolds Number

$$Re_D = \frac{V_{bulk} a}{\nu} \tag{1.1}$$

Unfortunately the relation between Reynolds number and flow development is still not clear and additional empirical synthetic parameters are used in order to better characterize the jet. Since the very first works on shear layer turbulence (*5*), the literature identifies three different zones: the near-field, the intermediate-field and the far-field zone. The first one is located near the nozzle and contains the so-called potential core. The far-field zone, far from the nozzle (*1*), is also called establishment zone (*2*) and starts when the flow becomes self-similar, as described by Pope (*16*). The intermediate zone contains all the transitional phenomena between these two states. The potential core extends till $x/a \cong 2$ and the far-field zone starts approximately from $x/a > 30$ (*1*).

Defining the velocity at the jet center line $U_c(x) = \overline{u(x,t)}\big|_{center-line}$, and the half width of the jet $r_{1/2}(x)$ as the radial distance from the center line at which the velocity is half of $U_c(x)$ it is possible to obtain the following characteristic relations

$$\frac{U_i}{U_c(x)} = \frac{1}{K}\left(\frac{x - x_0}{a}\right) \tag{1.2}$$

$$\frac{r_{1/2}}{a} = K_r \frac{x - x_{0r}}{a} \tag{1.3}$$

$$\beta = \arctan\left(\frac{1}{K_r}\right) \tag{1.4}$$

Where $U_i = U_c(x = 0)$, K and K_r are the proportionality coefficients named velocity decay and spreading rate coefficient respectively, and x_0, x_{0r} the hypothetical origins

of the flow, found with the best fitting line (*1-7*). Tab. (1.1) collects some literature values for these variables and provides information on the diagnostic used for the experiment (HWA= hot wire anemometer, LDA= laser doppler anemometer, PIV= particle image velocimetry).

Reference	Re_D	x/a	K	x_0/a	K_r	Diagnostic
Wyagnasky and Fielder(*8*)	100000	<50 - >50	5 - 5.7	3 - 7	0.086	HWA
Boguslawski and Popiel(*9*)	100000	<12	5.9	0.5	0.08	HWA
Capp(*10*)	100000	<100	5.8	4		LDA
Lumely(*11*)	11000	<150	6.06			HWA
Hussein(*12*)	95500	<120	5.8	4	0.094	HWA
Hussein(*12*)	95500	<120	5.9	2.7	0.102	LDA
Malmstrom(*13*)	1300	<40	5.94	-2.0		HWA
Xu and Antonia(*14*)	86000	<75	6.5	2.6	0.086	HWA
Xu and Antonia(*14*)	86000	<75	5.6	3.7	0.095	HWA
Kwon and Seo(*15*)	5000	<75	5.5		0.11	PIV
Fellouah and Pollard(*3*)	30000	<29	5.59	2.5		HWA
Vourus(*1*)	550000	<60	5.7	2.65	0.078	LDA

Tab. 1.1 Vourus and Panidis review of free jet data

As confirmed by many experiments, the equation (1.2) for the center line velocity is valid since a precise value of $x/a \cong 10$ for free round jets (*1, 3*).
Tab. (1.1) reports values of the characteristic coefficients included in the following ranges

$$5 < K < 6.5$$

$$0.8 < K_r < 0.12$$

The K-Reynolds dependence reveals that the entrainment phenomenon saturates at a

critic Reynolds $Re_{Dcr} \cong 2 \cdot 10^4 \div 3 \cdot 10^4$ as shown in Tab. (1.2) and Figure (1.2) (*17, 18*).

Re_D	k	x_0/a
305000	5.92 - 6.17	1.0 – 2.5
127000	5.87	2.5
51000	5.42 – 6.17	1.0-2.6
25000	4.19 – 5.65	1.5 – 2.6
18000	3.72	2.6
5000	2.66	3.2

Tab. 1.2 Re-K dependency

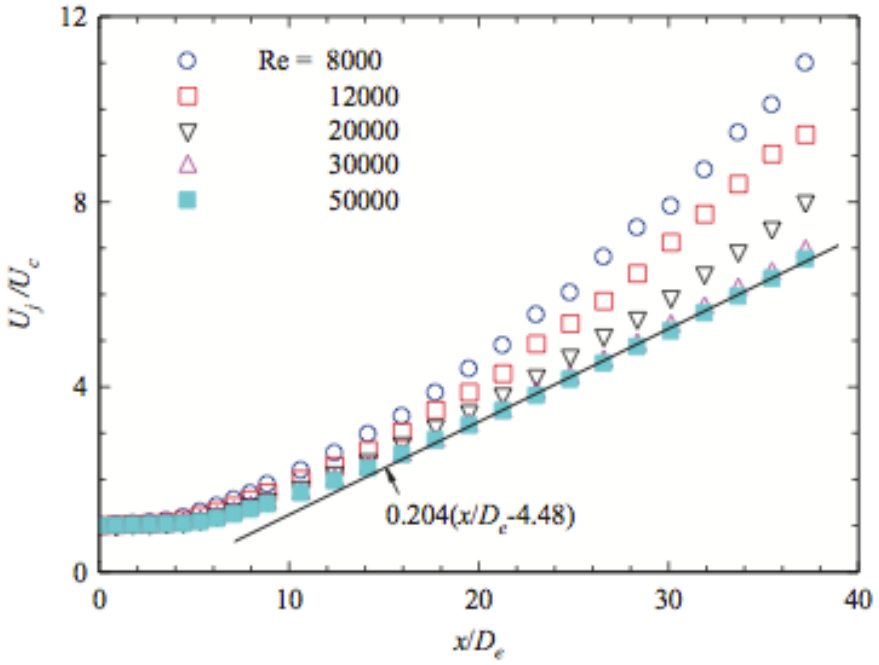

Figure 1.2 Velocity decay convergence (*20*)

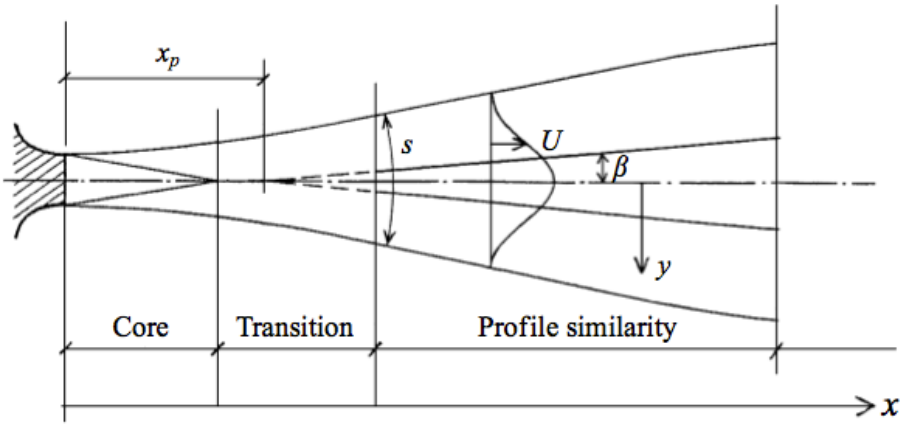

Figure 1.3 Half-width spread angle (*13*)

Concerning the spreading rate, the work of Xu, Pollard, Secretain and Sadeghi (*19*) reveals that the spreading rate decreases if Reynolds number value increases till a certain critic value. A linear law has been proposed by Hussain in order to describe the behavior of β, the half-width spread angle for low Reynolds(*12*) (Figure (1.3)).

$$\begin{cases} Re_D \leq 2 \cdot 10^4 \\ \tan\beta \sim {}^{1}/_{Re} \end{cases} \tag{1.5}$$

The axial velocity profile, as we can see in Figure (1.2), in the third zone assumes a Gaussian-like shape (*13*)

$$U(\xi, x) = U_c(x) e^{-ln2(\xi)^2} \tag{1.6}$$

where $\xi = r/r_{1/2}$ is the parameter related with the jet diffusion. The half-width and the velocity decay coefficient are physically related to the momentum diffusion. The following ratio can be chosen as representative quantities

$$\frac{\dot{m}}{\dot{m}_0} = \frac{2\pi\rho \int_0^{r_{1/2}} U(r)dr}{2\pi\rho \int_0^{a} U(r)dr} \qquad (1.7)$$

where r is the radial distance from the centerline and ρ is the density of the fluid. It represents the mass flow in the circle with radius equal to the half-width radius, and the mass flow that remains inside the projection of the entrance circle of the pipe in all the sections. Vourus and Panidis (*1*) denote that this function relation remains constant till $^{x}/_{a} \cong 10$. Close to the exit, the mass flow ratio increases slightly near the end of the potential core region, while, further downstream, the increase is significant and a linear dependence with the axial distance is eventually established.

In 1997 Malmström (*13*) pointed out that there is no clear relation between Re_D and the other coefficient like K, but there seems to be a clearer relation with the peak velocity in the pipe. The reasons for this behavior are still not clear, but an analysis based only on an integral diameter Reynolds number is not sufficient. Although the Re_D is a very useful parameter, it does not take into account the velocity profile, and therefore the boundary layer $\delta_{b.l.}$amplitude in the pipe, which is an important information to know the dimension of the first eddies. The initial profile plays an important role in the near field development, which also influences the jet evolution to the self- similarity region in the far field (*1*). An important signal of this complex behavior could be found on the apparently stochastic relation between Re_D and x_0(Tab. (1.1)). Mi, Nathan and Nobes (*21*), in a study on the influence of the initial conditions on jet flow field, find well defined vortices in contraction jets flow development very close to the efflux, due to the natural instability of the thin shear layer. The same structures are not found in pipe jets, due to the thicker boundary layer. The absence of these structures delays the entrainment of ambient fluid and the mass flow rate is almost constant close to the exit. Thus, the mass flow that emanates from the pipe is probably initially redistributed to a larger radial area without affecting the center-line velocity or the jet half width until $^{x}/_{a} = 10$.

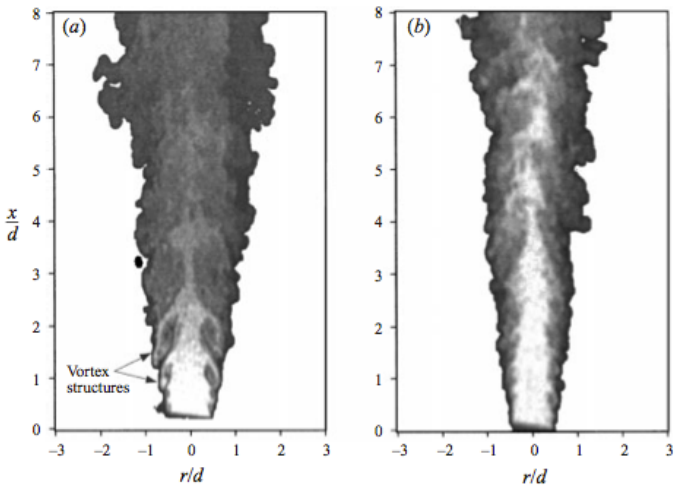

Figure 1.4 Representation of different near-field region due to different inlet conditions(*21*)

The structure of the near-field turbulence is distinctly different for the two jets as in Figure (1.4). The vortex structure is a result of the roll-up of the laminar boundary from the inner wall of the nozzle. These axis-symmetric toroidal vortices engulf both ambient and 'pure jet' fluid and 'pinch-off' the tip of the potential core of the jet. The formation of the primary vortices in a jet from a smooth contraction is known to originate from an instability within the shear layer. When the initially laminar shear layer from a smooth contraction nozzle becomes unstable, velocity fluctuations increase in amplitude, resulting in the roll-up of the shear layer into a train of azimuthal vortex elements. Any slight asymmetry in the spacing between two adjacent vortices, or inequality in their strengths, induces them to roll around each other pairing and eventually forming a single larger vortical structure. By contrast, small-scale turbulent structures dominate the near field of the emerging jet from the long pipe. This is explained clearly in a work by Xu and Antonia (*14*) where an experiment with a pipe and a contraction efflux is performed. Blausius profile, typical of a pipe, presents a lower velocity gradient near the wall than the top hat profile of a contraction. The much thicker shear layer of the pipe preserves the stability of the flow for a longer distance, delaying the instabilities till $^{x}/_{a} = 3$ as in Figure (1.4). The vortices rolling-up is the typical Kelvin-Helmotz instability (Figure (1.5)), which, due to the geometry of the problem, presents itself in a toroidal geometry (Figure (1.6)). In the near field zone it is shown that the spectrum of the transversal velocity has always a peak at a lower frequency than the contraction.

Figure 1.5 Kelvin-Helmotz instability

The thicker initial shear layer of the pipe jet produces a dimensionally lower frequency instability, resulting in longer wavelength structures, which develop and pair at larger downstream distances. The regular vortex formation and pairing are disrupted in the shear layer of the pipe jet. The stream-wise vortices, which enhance entrainment and turbulent mixing, are absent in the shear layer of the pipe jet. The formation of large-scale structures should occur much farther downstream in the pipe jet than in the contraction jet.

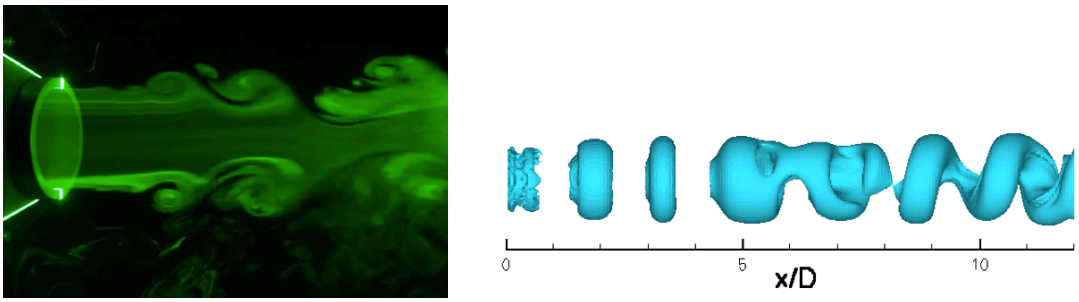

Figure 1.6 Representation of toroidal vortices (left) and second kind of instability (right)

In a recent work a modified Gaussian-like shaped function with a parameter η is proposed, in order to take into account the initial profile of the velocity at the pipe outlet (*22*).

$$U(x,\xi) = U_c(x)e^{-(ln2(\xi)^2)^{\eta(x)}} \qquad (1.8)$$

It is clear that the turbulence profile and the vortices depend on this initial condition, and the position of self-similarity can be anticipated or delayed from that. Despite of Townsend's hypothesys (*5*) that "turbulence forgets its origin" it is now clear that this is not true at all. It is observed the presence of big vortices in this last zone, which depends on the initial conditions. Another important characteristic of this kind of flow is the anisotropy of the turbulence. This is noticed in almost all the works aforementioned. A deeper analysis of turbulence goes beyond this brief on free jets. As a conclusion it could be said that all the parameters previously listed characterizing the flow are surely a function of Re_D, but also of the boundary layer thickness $\delta_{b.l.}$.

$$K = f(Re_D, \frac{\delta_{b.l.}}{a}, \dots) \tag{1.9}$$

$$K_r = g(Re_D, \frac{\delta_{b.l.}}{a}, \dots) \tag{1.10}$$

$$\frac{m}{m_0} = \frac{2\pi\rho \int_0^{r_{1/2}} U(r)dr}{2\pi\rho \int_0^{a} U(r)dr} = h(Re_D, \frac{\delta_{b.l.}}{a}, \dots) \tag{1.11}$$

1.2. ROLE OF CONFINEMENT IN ENTRAINMENT PHENOMENON

Considerable experimental effort has been devolved into the study of free round jets. There are relatively few studies on jets into a confined environment (*23-25*) despite of their presence on many practical applications. In free jets, there is a negligible effect of the surrounding enclosure on its characteristics, whereas in confined configurations the surrounding enclosure significantly affects the jet hydrodynamic characteristics. The fluid entrained in the jet from the environment needs to be substituted, but because of the limited amount of surroundings fluid this can be obtained only through a recirculation of the flow into the confined environment (*23*) as shown in Figure (1.7).

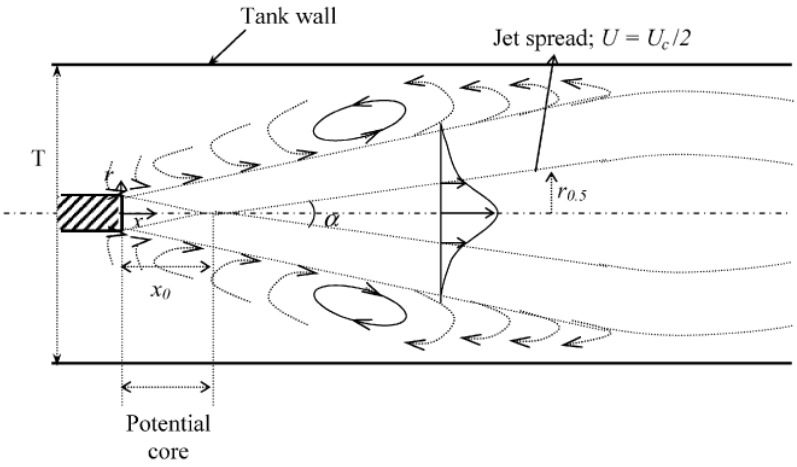

Figure 1.7 Recirculation in a confined jet system

The recirculation is characterized by two counter-rotating eddies. Although the average velocity reaches quickly the self-preserving state $x/a \cong 2$, the turbulence reaches this characteristic only at $x/a \geq 10$ (*25*). The decay rate of the confined jet is found to be almost three times more than the decay rate of the round free jet, but it is slightly lower than that of plane free jets (10–30% greater) with similar Reynolds number. The spreading rate law is found to be similar to that of the plane free jets but higher than round free jets. It is deduced from the obtained results that, although the confined jet is a three-dimensional flow in nature, the decay K and K_r found in a confined jet, are closer to two-dimensional values rather than that of a three-dimensional flow (*25*).
In fact the decay law follows more closely the following two-dimensional decay (*25*).

$$U_c \div x^{-\frac{1}{2}} \tag{1.12}$$

$$\left(\frac{U_c(x)}{U_i}\right)^2 = \frac{1}{K_d}\left(\frac{x - x_0}{a}\right) \tag{1.13}$$

The value of the coefficient K is around $20 \sim 22$ for buoyant systems. This means that the confinement strongly anticipates the velocity equilibrium, remaining function of Re_D and $\delta_{b.l.}$. as in the free jet(*25*).

1.3. WALL-JET INTERACTION: COANDA EFFECT ON AN OFFSET WALL

At the beginning of XXth century, aerodynamicist Henry Marie Coanda, discovered and applied a particular flow phenomenon later named "Coanda effect". This effect refers to the tendency of a flow to be attracted and deflected by neighbor surfaces (Figure (1.8)).

Figure 1.8 Coanda effect

In our particular case the jet deviates for the presence of an asymmetric entrainment, creating a sub-pressure zone in the bottom corner and, consequently, a pressure gradient perpendicular to the jet. For this reason the flow is pushed against the wall (*26*) (Figure (1.9)). This effect, in case of wall located near the nozzle could be relevant. The new parameter to take into account, in addition to the previous used for free jets, is the distance from the wall H (Figure (1.9)). Unfortunately all the experiments available on this theme are mainly related to plane jet configuration. In their work Lalli, Romano and Miozzi (*24*) make a precise analysis of the behavior of the flow field varying H.

$$\tilde{x} = {}^{x}/_{a} \tag{1.14}$$

$$\tilde{H} = {}^{H}/_{a} \tag{1.15}$$

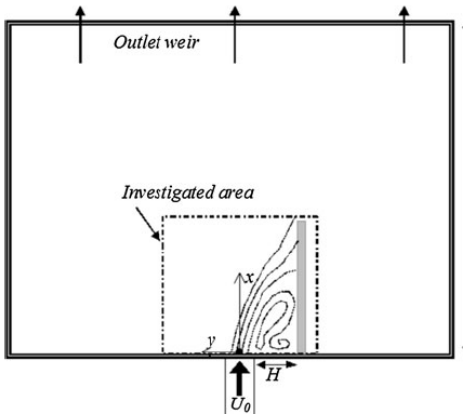

Figure 1.9 Flow deflection due to a side wall

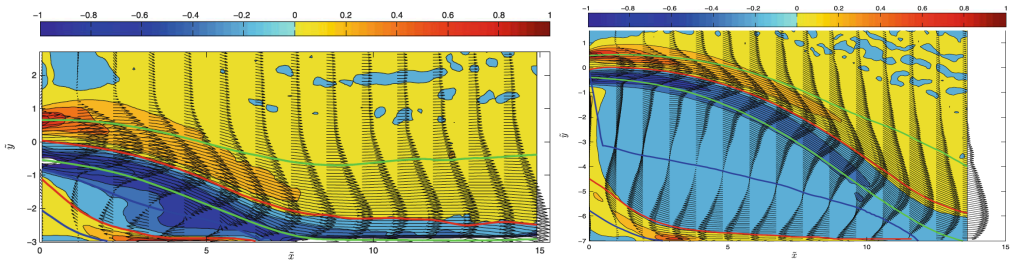

Figure 1.10 Velocity vector field for H=3 and H=7

In all configurations (Figure (1.10)) the flow is moving toward the lateral wall, generating a great recirculation upstream of the reattachment point x_r. In the recirculation zone two eddies are present: the first is the big one rotating clockwise, the second one, Moffat vortex, is pushed in the corner and rotates counter-clockwise (*27*). They find that the following relation between the reattachment point and x_r is almost linear and does not depend on Re_D number.

$$x_r/a = D_\zeta(\tilde{H})^{\delta\zeta} \qquad (1.16)$$

Where $\delta_\zeta = 0{,}851$ and $D_\zeta = 2{,}632$

Other results obtained with experiments with the offset wall jet match the coefficients of equation (1.16) (*28*). Using the upper red line as a curvilinear coordinate system (Figure (1.10)) they find a relation for a certain $\tilde{x}$ interval for the decay.

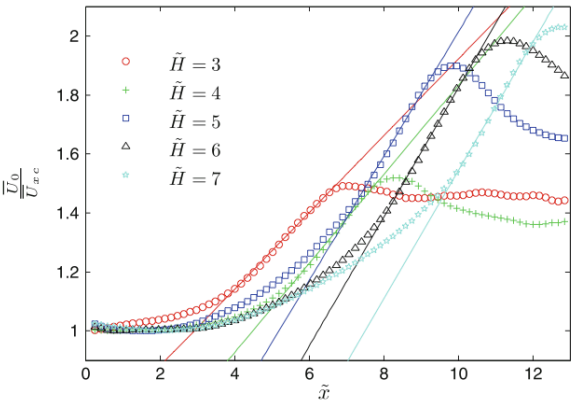

Figure 1.11 Velocity on Xc

If U_{x_c} is the velocity measured on the curvilinear coordinate, the relation for the velocity decay is

$$\frac{U_i}{U_{x_c}} = 1 + K(\tilde{x} - \tilde{x}_0) \qquad (1.17)$$

It is interesting to observe that the flow seems to change in the interval $4 \leq \widetilde{H} \leq 5$ (Figure (1.11)). The spread of the Coanda jet is of course non-symmetrical to the geometrical jet centerline, and the whole jet width does not increase as linearly as for the free jet (Figure (1.12)).

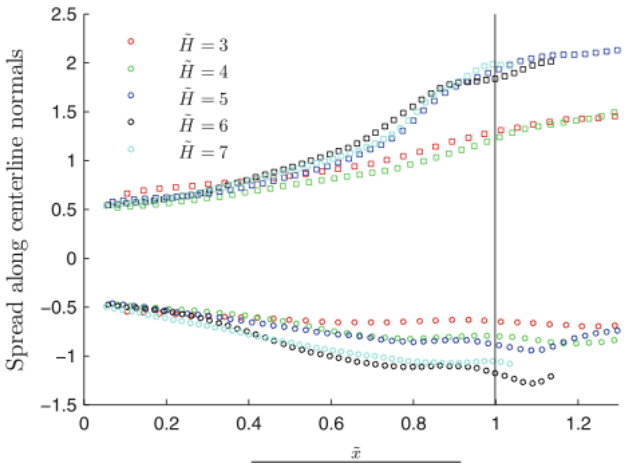

Figure 1.12 Asymmetrical spreading

The Coanda effect is one of the main reasons of asymmetries presence in a global system with symmetric geometry and boundary conditions.

1.4.JET-JET INTERACTION: MULTIPLE PARALLEL JETS

The new parameters introduced by this kind of configuration are the jet to jet distance, the mass flow ratio, the ratio between the mass flow rate of a jet divided by the mass flow of its neighbor (eq. (1.18)), and the ratio between the jets distance over the jet diameter (eq.(1.19))(*6*).

$$\lambda = \frac{\dot{m}_j}{\dot{m}_{j+1}} \tag{1.18}$$

$$\frac{D_0}{a} \tag{1.19}$$

The essential feature of this flow is the sub-atmospheric region due to the recirculation between jets. This sub-atmospheric field deflects the center line of each twin jet ($\lambda = 1$) (Figure (1.13)) in the direction of the low pressure zone and the deflection matches with an arc of a circle of radius *R* (*6*). This results in an attraction between the jets conducting to the mixing. Downstream of this zone the jets collapse and merge, creating a zone with a higher pressure than the environmental one. One of the first works on this theme, a study of the incompressible twin free jet configuration, was done by Tanaka (*4*) in 1970 (Figure (1.14)).

The experiment conditions guarantee the symmetry of the velocity field. The field could be divided into three zones: the converging region, the merging region and the combined flow region, in which the velocity and turbulence profiles become single jet-shaped, as represented in Figure (1.13)(*4, 29*). Three parameters could be used to describe the resulting flow: the merging point or stagnation point x_s, which represents the end of the recirculation, the combination point x_c, which represents where the radial profile assumes a single jet-like shape, the deflection radius *R* and the reattachment point x_r, representing the point with zero velocity at the wall.

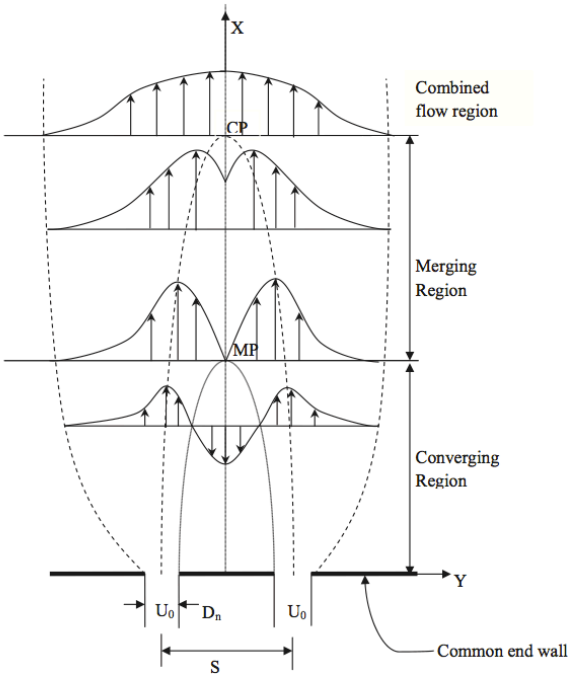

Figure 1.13 Representation of the flow regions

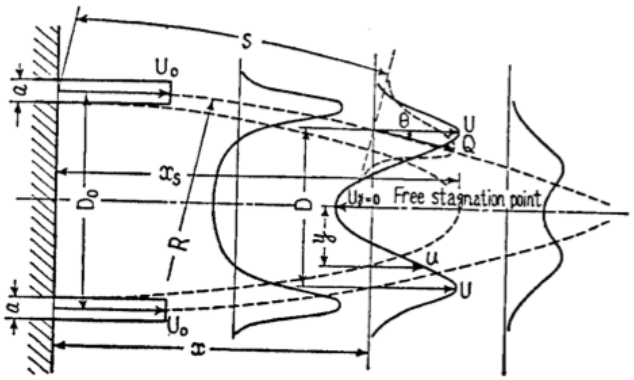

Figure 1.14 Twin jets configuration

The merging region is observed shifting upstream if the inlet velocity increases. Two big counter-rotating vortices are detected in the low-pressure zone. The velocity is negative and from the joining, represented by a stagnation point, it turns to be positive. The maximum value of the turbulence, as expected, is reached on the edges of the jet, where the velocity gradient is steepest. Anderson and Spall (*30*) in 2001

find centerline velocity and pressure profile to have the same characteristics noticed by Tanaka's first report (*4*).

In his second report (*7*), Tanaka noticed that K seems to be independent by Re_D ($23\,{}^{m}/_{s} \leq u \leq 34\,{}^{m}/_{s}$ or $4.29 \cdot 10^3 \leq Re \leq 8.75 \cdot 10^3$). Althoug there are no confirmations, it is possible that, in the operative Reynolds range, viscous forces have already saturated their effect like in the case of a single jet (*19*).

The deflection of the centerline, as previously said, matches with an arc of a circle R upstream of the stagnation point. Downstream, the centerline is no longer the one with the maximum velocity, or in other words, the centerline of the jet diverges from the arc of the circle (Figure (1.15)). As an empiric law it is found that if ${}^{D_0}/_{a} \leq 16$ the dimensionless curvature radius is constant (${}^{R}/_{a} \cong const$). For values of ${}^{D_0}/_{a} \geq 16$ the law changes and the radius increases linearly.

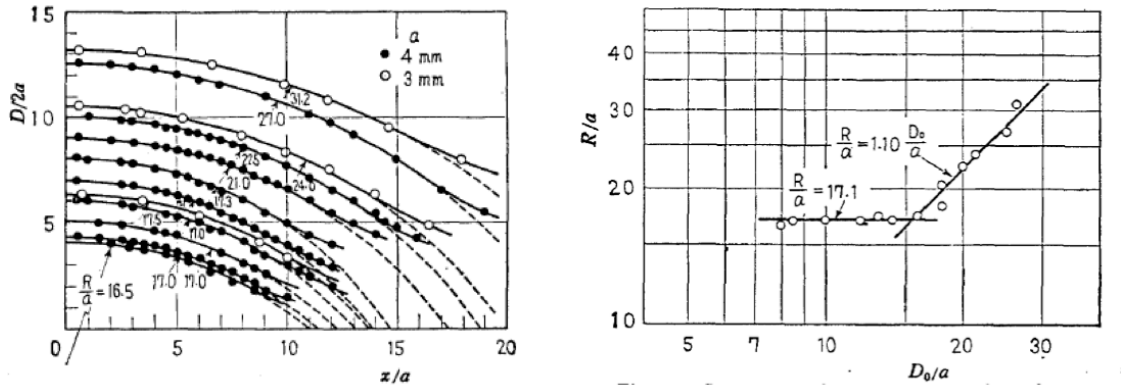

Figure 1.15 Curvature Radius with D/a variation

$$\frac{R}{a} = 17.1 \qquad \text{for } {}^{D_0}/_{a} \leq 16 \qquad (1.20)$$

$$\frac{R}{a} = 1.1\frac{D_0}{a} \qquad \text{for } {}^{D_0}/_{a} \geq 16 \qquad (1.21)$$

The relation proposed for the decay is

$$\frac{U_i}{U_c(x)} \sim \frac{1}{K}\left(\frac{x - x_0}{a}\right)^c \tag{1.22}$$

With $c = 0.055$. Also the spreading ratio is larger and, has a maximum for the same value and shows a clear non linear behavior (*6*).

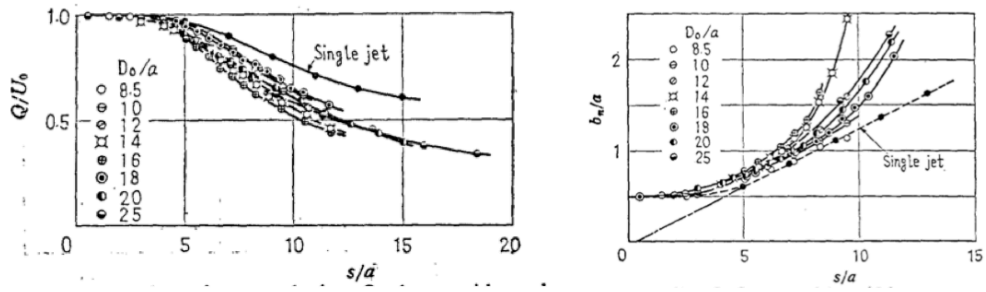

Figure 1.16 Velocity decay and Spreading rate on the center line

The jets interaction increases the turbulence as a consequence of the diffusion of the momentum (Figure (1.16)). In Figure (1.18) the velocity decay is presented for single, twin and triple jets.

Concerning the position of the stagnation point x_s shows a critic value for ${}^{D_0}/_{a} = 16$ too (*4*).

$$\frac{x_s}{a} = 5.06\left(\frac{D_0}{a}\right)^{0.27} \quad \text{for } {}^{D_0}/_{a} \leq 16 \tag{1.23}$$

$$\frac{x_s}{a} = 0.667\ \frac{D_0}{a} \quad \text{for } {}^{D_0}/_{a} > 16 \tag{1.24}$$

In two works, Sheu and Lin (*31, 32*) have found an experimental relation between the stagnation point and the nozzles spacing D_0 for plane jet interaction.

$$\frac{x_s}{a} = \frac{0.48D_0}{a} + const \quad \text{for } {}^{D_0}/_{a} \leq 30 \tag{1.25}$$

$$\frac{x_s}{a} = 1 \quad \text{for } {}^{D_0}/_{a} \geq 30 \tag{1.26}$$

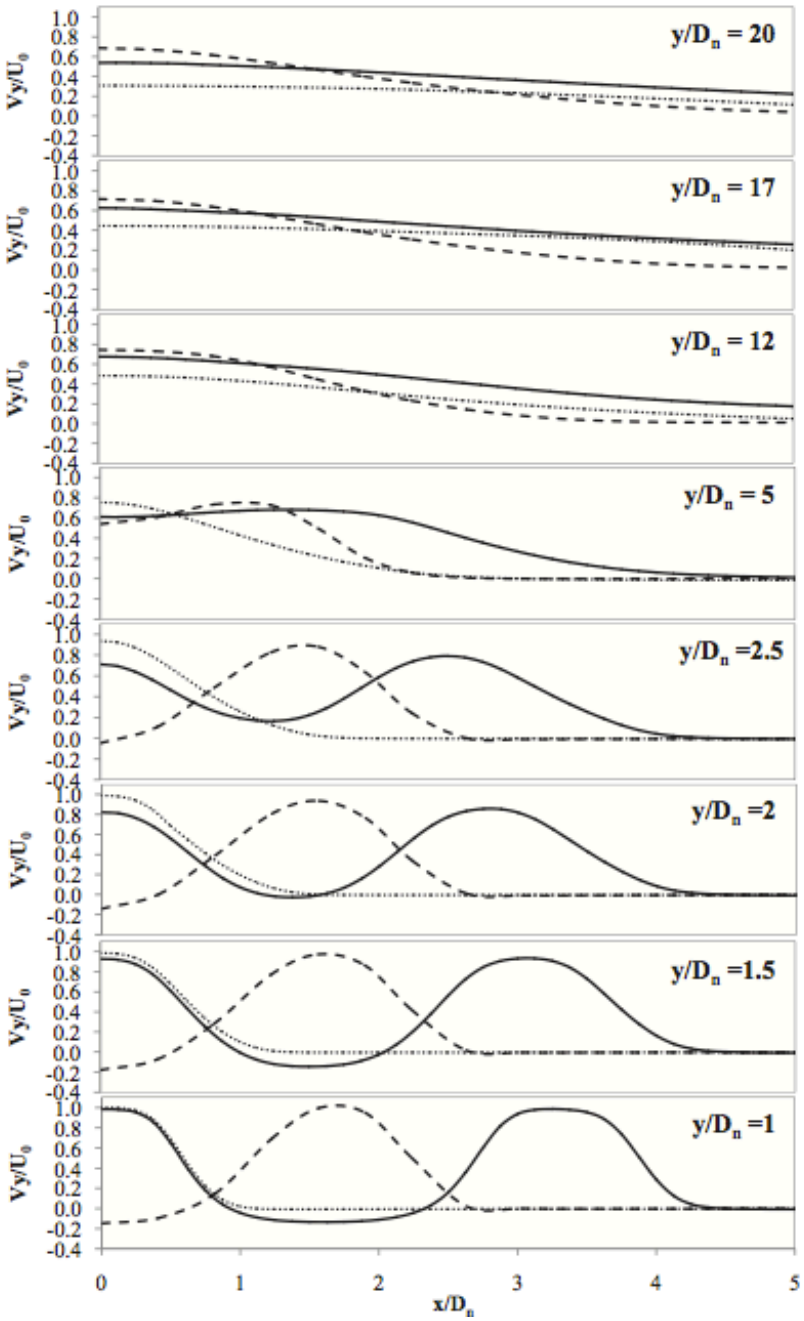

Figure 1.17 Single jet (dotted line), twin jets (dashed line) and triple jets (straight line) Velocity in stream-wise direction

These equations show a linear relation of the merging point under a critical value of D_0/a and an invariance above this value. In the second case the merge point occurs far enough from the inlet not to affect the flow development.

A regression on literature data (*33*) with a value of $D_0/a = 13$ shows a general relation for merging and combined point, showing the dependency on initial conditions, in particular on I, turbulence intensity.

$$\frac{x_s}{a} = \frac{0.721 D_0}{a} + 2.06I - 2.453 \tag{1.27}$$

$$\frac{x_c}{a} = \frac{1.231 D_0}{a} + 2.06I - 2.453 \tag{1.28}$$

In his third report, Tanaka has studied a triple jets configuration varying λ, the mass flow ratio. If the diameters of pipes and the density of the fluid is the same in all the operative conditions, the eq. (1.18) becomes (*6*).

$$\lambda = \frac{U_{l0}}{U_{c0}} \tag{1.29}$$

With U_{l0}, bulk velocity of the side jets, and U_{c0} velocity of the central one. There are three possible solutions: The first one, case A ($\lambda \leq 0.707$), where the central jet is strong and absorbs the others. In this first case, the velocity of the central jet is strong enough to overcome the opposite pressure gradient between the lateral jets, pushing the recirculation very close to the efflux between each jet. In case B ($0.707 \leq \lambda \leq 1.15$) the flow is still symmetrical but the central jet is absorbed by the boundary of the lateral ones. Finally, in case C ($\lambda \geq 1.15$), the flow turns into an asymmetrical configuration and the central jet deflects. This effect is called symmetry breaking and it is shown in Figure (1.18). The transition is described as "noisy and unstable". Nishimura *et al 2000* (*34*) observed in particular conditions a massive presence of periodic oscillation in a flow with three jets that increases strongly the diffusion. This theme will be treated in a particular paragraph.

It is reported here the experimental result for radial profile for all the three cases. The

asymmetry in the last case of Fig. (1.19) is evident.

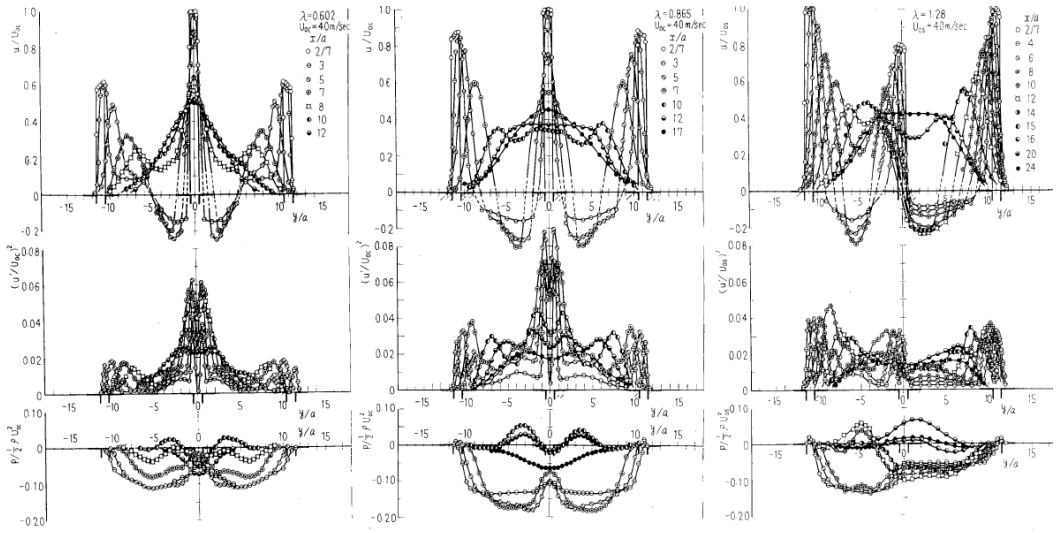

Figure 1.18 U, u', and p for A, B and C

Durve (*33*) compares twin jets with triple jets configuration and finds that the velocity decay increases with the number of the interacting jets .

Very few experiments are conducted on an array of jets flowing into a confined environment like in the present study configuration. Probably, in the whole available literature, Kunz's experiment is the most similar to the present case of study, despite the is much stronger confinement (*35*). Defining W as the distance between the upper and the lower plane, the degree confinement is equal to $W/a = 1/2$. For this reason the fluid expands when entering in a bottleneck. From their analysis, the great complexity of the flow map is evident. Many regions are characterized by negative stream-wise velocity vector showing great recirculation. Defining U_s as the streamwise velocity in the middle of two pipes, the spreading ratio is an important dimensionless index characterizing the flow

$$SR = \frac{U_C - U_s}{U_c} \tag{1.30}$$

Starting from a value of 1, it is found to increase until a certain distance from the inlet and then to start decreasing. In the case in which this value is higher than 1, it reveals

the presence of recirculation. Concerning average velocity, no symmetry breaking or oscillating solutions occur in this system. Probably the presence of the narrow confinement does not allow coherent structures to develop in the shear layer. This is confirmed by their spectral analysis, which does not show particular peaks. However this is not a general behavior. There are other cases in literature, in which parallel jets interacting create an asymmetrical flow map for the average velocity or an oscillating unsteady solution. In Nishimura's experiment, for example (*34*), as three jets flow into a free environment and the central jet sways and meanders, and the boundary of the intermittent region of the outer jets is wavy. This phenomenon is called flapping. Chiang, Sheu and Wang (*36*) found an asymmetrical average velocity configuration already at low Re ($Re \cong 2660$).

1.5.NUMERICAL APPROACH ON JETS SIMULATION

CFD, has become an important tool in industrial design. Jets, because of their importance in technical applications, are one of the most studied topics in numerical simulation, and the literature contains a lot of examples. However the results of first numerical models do not match experimental data. Wilcox (*37*) reports results for the spreading ratio in a free round jet simulation with a standard $k\varepsilon$ and for $k\omega$ and reveals that the error in the best case is around 16% confirming that standard models do not work very well. In a NASA memorandum (*38*), some results of numerical simulations are collected and performed with standard $k\varepsilon$, Wilcox $k\omega$, Menter SST and Spalart Allmaras (one and two equations models) and they showed large discrepancies. Round jets represent one of the most important examples of the lack of RANS analysis when it inserts the hypothesis of isotropic turbulence. The so called "round jet-anomaly" for $k\varepsilon$ lies in this approximation(*20*). Many papers (*14, 21*) describe the presence of vortical coherent structures, proving the presence of very complex phenomena. Errors of the order of 40% in velocity evaluation occur when a standard turbulence RANS model is used.

As represented in Figure (1.19) the predictions and the experimental data for velocity decay, for many kind of nozzle shows the opposite behavior. In general $k\varepsilon$ does not work well with high velocity gradients. All this methods for round jets tend to overestimate the diffusivity of the momentum and so the spreading rate. Obviously many coefficients could be modified in order to obtain a better fitting of the data (*39*). However, this is not an improvement in the physics reproduction. These problems of Standard RANS methods are obviously present in multiple jets configurations(*40*) and they are not solved even for *RSM* model (*30*) which not always has better performance than $k-\varepsilon$. In general for the shear layer flow the great problem consists in the simulation of the transition zones in which the shear layer instabilities occur.

Because of this lack many studies were conducted using LES method. Very impressive is the perfect reproduction of the velocity and turbulence obtained by Bogey and Bailly(*41*). However the computational cost remains very high. For this reason in the last years many improvements were operated on classical RANS methods in order to simulate shear layer flows. More advanced multiple equations methods or non-linear methods are studied (Figure (1.20)).

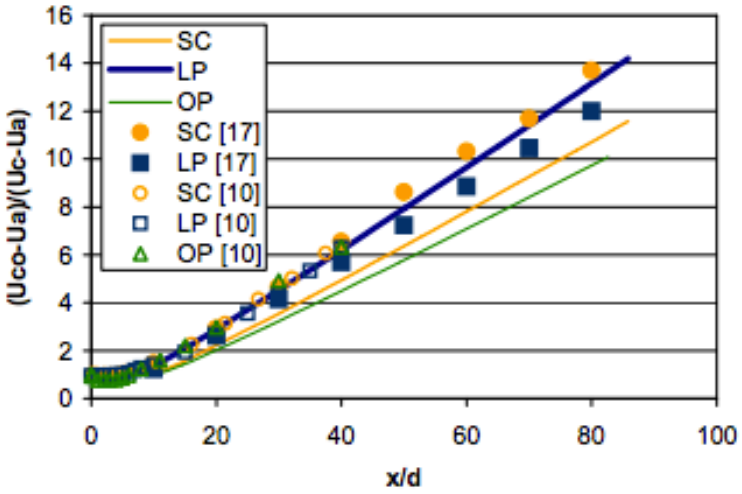

Figure 1.19 Velocity Decay experimental data and standard $k\varepsilon$ for long pipe orifice (LP), smooth contraction (SC) and sharped edge orifice plate (OP)

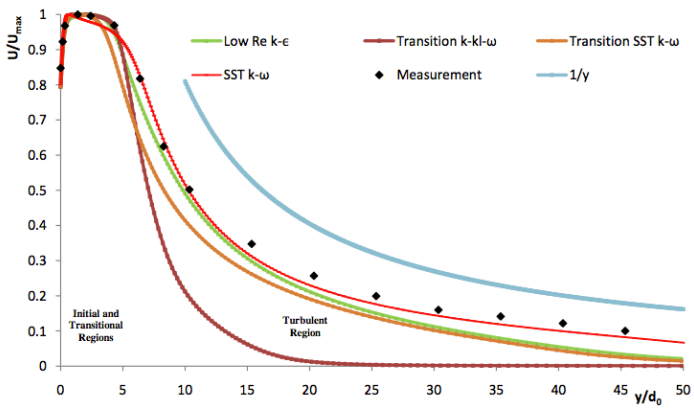

Figure 1.20 Performance of different numerical methods on prevision of velocity decay

Transition $kkl\omega$ works very well near the inlet, while $SST\ k\omega$ in the self-preserving region. $SST\ k\omega$ is the closest to the experimental data in terms of velocity decay (*42*). In a work of 2011(*43*) some linear multiple equation models, or non linear models, have been performed on many jets phenomena. The results show that, despite the simple geometry, the linear models work well only on the velocity. Concerning the turbulence, or both turbulence and velocity in case of complex geometries, non-linear models perform better.

1.6. SYMMETRY BREAKING AND OSCILLATION PHENOMENA

Navier Stokes equation is a non-linear partial differential equation, which can admit more than one solution. When it happens it is impossible to know a priori on which solution the physical system will converge. Additionally, this solution could be steady or oscillating with a precise frequency, which could be simply found with spectral analysis. The mathematical treatment of bifurcation phenomena and the stability analysis of Navier Stokes equation go beyond the subject of this work. However, some studies and experiments could let us figure out how it manifests itself. A significant work on this theme is conducted by Soong (*45*). It is observed that flow maps of twin planar confined jets vary some parameters, like Reynolds, confinement and nozzles distance. At very low Reynolds numbers the solution is steady and symmetrical. With fixed variables, at the increase of *Re* it is noticed the presence of a bifurcation. The solution turns into an asymmetrical configuration. This behavior is confirmed by Drikakis(*46*). It could be of interest to notice that the critic Reynolds for the symmetry breaking and for periodic unsteady solutions increases when the confinement is stronger. Although the previous experiments are conducted at $Re = 10 \div 100$, it is interesting to observe how in a symmetrical domain with symmetrical boundary conditions the flow map could be asymmetrical. This behavior is explained by Sobey and Drazin (*47*) using bifurcation theory. The cause of symmetry breaking are experimentally confirmed to be in the Coanda effect, which, stronger in a preferential side, causes the flow to be pushed against a wall (*48*). Chiang Sheu and Wang (*36*) have studied this phenomenon from a numerical point of view finding the same breaking beyond a critical Re (Figure (1.21) and Figure (1.22)).

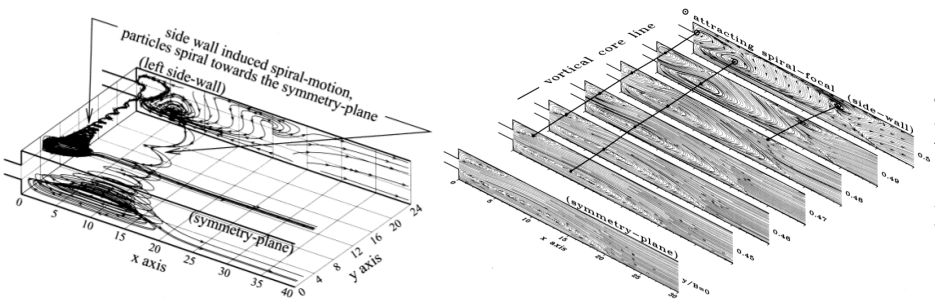

Figure 1.21 Particle path lines (left) and stream-wise parallel plane flow visualization (right)

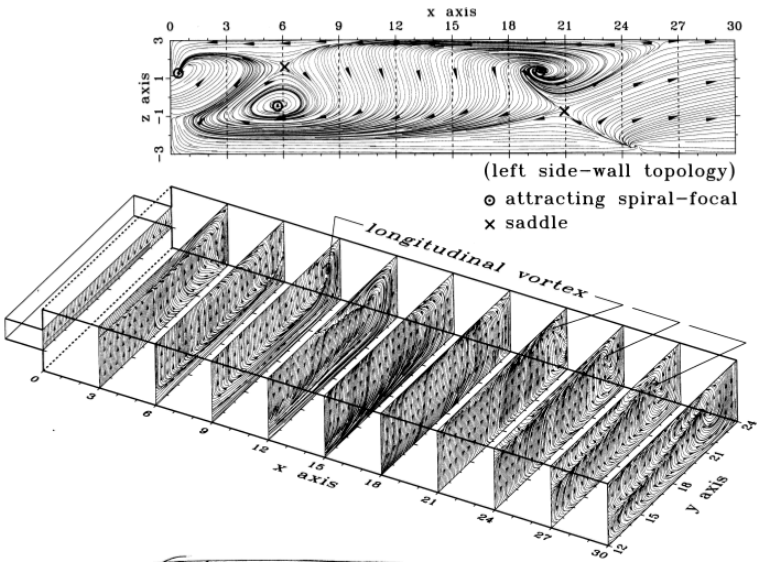

Figure 1.22 Spanwise parallel plane flow visualization

Concerning the unsteady solutions, oscillation in a spectral analysis appears like a peak in low frequencies (Figure (1.23).

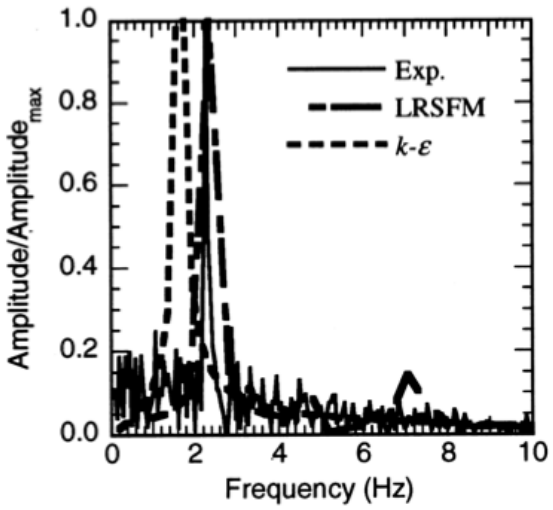

Figure 1.23 Peaks due to flapping oscillations

Kunz, in his experiment, does not find peaks (*45*), at least at a frequency low enough not to be aliased.

Concerning multiple jets, in a work of Politecnico di Milano a large eddy simulation on Kunz system has been performed (*35, 44*) and the results show that not always a steady solution exists. It is not clear if this periodical solution represents something related to the real flapping of the flow or a leak on the numerical results.

The symmetry breaking and the oscillating solution sometimes do not allow using symmetrical boundary conditions in a numerical fluid dynamics problem, in order to save computational time. Setting a numerical problem it is important to detect in advance the possibility of a symmetry breaking in a symmetric domain. With this information only a part of the domain could be simulated.

2. Experimental technique and numerical approaches

In the first part of this chapter a description of the Laser Doppler Velocimetry (LDV) technique for experimental measurement and the laser system set-up are reported. The error estimation for velocity and turbulence measurements and the description of alignment operations are also presented.

In the second part is reported an overview of the numerical approaches used, such as Reynolds Average Navier Stokes (RANS), and Large Eddy Simulation (LES).

2.1. LDV TECHNIQUE AND LASER SYSTEM

Laser Doppler Velocimetry (LDV) is a non-intrusive technique for the measurement of punctual velocity in a flow field.
The measurement is realized through the interaction between micro-particles present into the test-section, and a control volume composed by an interference fringes pattern (Figure (2.1)), created by the intersection of two monochromatic beams of a laser source.

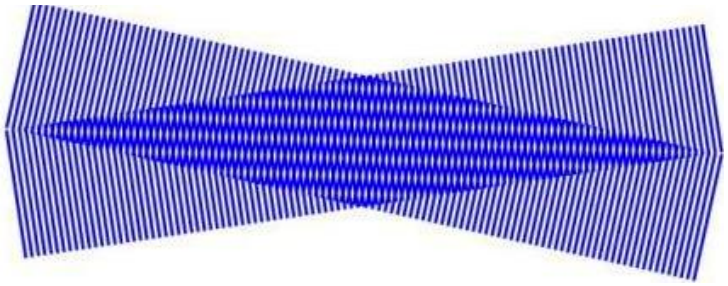

Figure 2.1 Interference Fringes

When a micro-particle, with density similar to the working fluid and reflective surface, crosses the volume, a scattered light is produced. It is captured by an optical receiver and then turned into an electric signal, as shown in the schematic of Figure (2.2). The obtained current pulse, the burst, goes through a band pass filter to minimize the noise-to-signal ratio, and, subsequently, a high

pass filter removes the pedestal with a Discrete Fourier Transform ((Figure (2.3), left). The peak of the signal spectrum represents the doppler frequency. The velocity measurement is based on the relation $f_d = \frac{V_n}{\delta_f}$ among the particle velocity normal to the fringes V_n, the fringes distance δ_f and the signal frequency f_d.

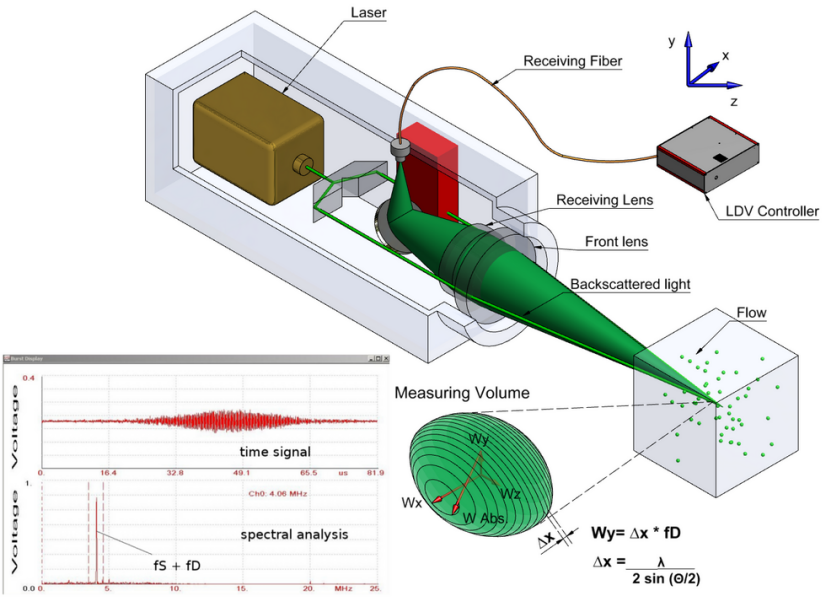

Figure 2.2 LDV schematic

The distribution of particles through the fluid is not uniform and their size and trajectory are not always the same. This causes a random occurrence and variation of the bursts in time. A low detection threshold level is chosen and above this value the signal is detected and stored, as shown in Figure (2.3), right. Lowering this limit an increase of the data rate accompanied with an introduction of noise is caused, and vice-versa.

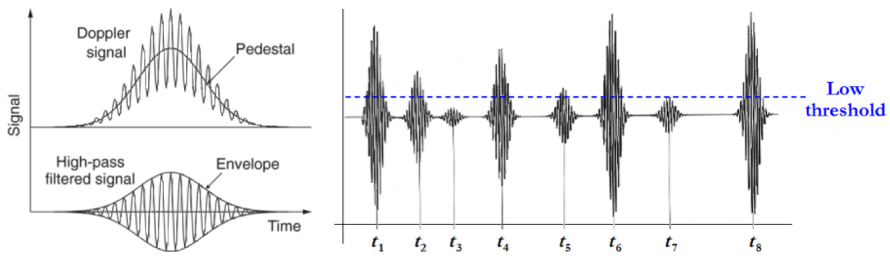

Figure 2.3 Burst signal with and without pedestal (left) and signal threshold (right)

All data are obtained by the transmitting optics Dantec Dynamics FiberFlow optical system and an Argon-Ion laser, and elaborated by Dantec's BSA Flow Software. The Dantec Dynamics FiberFlow optical system is composed by Bragg cells, fibre manipulators, optical fiber connections and a transmitting probe. Dantec Dynamics also provided for the Burst Spectrum Analyzers (BSA) used as signal processors for both the green and blue laser wavelengths. A high precision of its movements is achieved with a high resolution transverse system, on which the laser probe is installed. Figure (2.4) represents an image of the laser probe mounted on the transverse system, which is maintain fixed and stable using a mass. In order to have a more detailed description of all components refer to (*49*).

Figure 2.4 Transverse system

2.2. PROCEDURE AND PARAMETERS FOR LASER SYSTEM

Two important aspects of the measurement campaign are: the procedure for the laser system use, and the laser system parameters set-up, shown in Tab. (2.1). The procedure for the laser system use is composed by the following steps:

1. Activate the cooling system by opening the valve.
2. Switch on the power.

3. Check if power and current knobs are at lowest level and if the mode button indicates Current.
4. Open the shutter on green or blue laser source.
5. Turn the key and check if the green light "plasma on" is turned on and the red light for the cooling system is shut down. If not, increase the water flow rate.
6. Turn the button "mode" on "power".
7. Regulate the beam intensity through the power knob.
8. Turn on the BSA, the oscilloscope and the traversing movimentation system.
9. Check if the bursts are visible on the oscilloscope and then open the BSA flow software.

An important operation is the movement of the focus inside the water, since the beams deviate from the direction that they have in the air at the water interface. For this reason a correction in the coordinate system is necessary to match the real focus position with the coordinates indicated by the traversing.

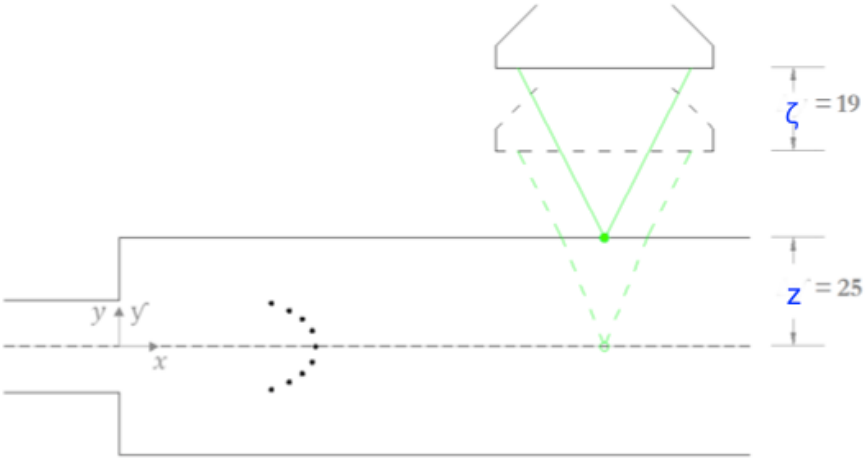

Figure 2.5 Software coordinates transformation representation

In order to simplify the operation, a transformation coefficient $\alpha = \Delta\zeta/\Delta z = 1.333$ is inserted via software as shown in Figure (2.5). Additionally, another consideration to take into account is the reflection of the top and the bottom glasses. The light flux reflected by glasses spheres is usually very low, but when the laser light is scattered from a large surface, such as the glasses of the plenum, this may increase significantly. If this happens during normal

measuring conditions, when the laser intensity is high, the beam reflected could damage the photomultiplier. This effect can be avoided keeping the laser focal far from the glasses.

OPERATIVE PARAMETERS FOR THE LASER SYSTEM

Green Wavelength	514.5	nm
Green High Voltage	904	V
Green Gain	35	dB
Blue Wavelength	488	nm
Blue High Voltage	928	V
Blue Gain	40	dB
Beam Diameter	1.35	mm
Beam Expander ratio	1	
Focal Length	310	mm

Tab. 2.1 Laser system parameters

2.3. ERROR ESTIMATION FOR AVERAGE VELOCITY AND TURBULENCE

The goal of this analysis is to estimate the error for average velocity and turbulence, collecting samples of velocity $v_{i,n}$ for selected positions into the test-section. The errors on the single measurement are divided in:

- Positioning error
- Single velocity acquisition error

The first one may be related to the deformation of the system in time, errors on the traversing handling, and not punctual focal volume size (elliptic), while the second one is related to the measurement system accuracy. Finally the systematic error of single measurement is estimated as $\varepsilon < 0.01 v_{i,n}$.

In a turbulent flow, the velocity in each point has a distribution which is obviously unknown and so the evaluation of the average velocity is affected by a statistic uncertainty. In order to treat these multiple uncertainties and give a confidence interval for velocity and turbulence, the follow hypotheses are necessary:

1. the turbulence is treated as a stochastic phenomenon.
2. the velocity in each point is a random variable which have a Gaussian distribution $v_i \sim N(V_i, \sigma_i^2)$.

For the second hypothesis the particles flowing through the volume with a velocity $v + x$ have the same frequency of those flowing with a velocity $v - x$. The value of V_i and σ_i^2 is hence unknown, but may be estimated with sample quantities.

$$V_i^{\Sigma} = \frac{1}{N}\sum_{n=0}^{N} v_{i,n} = \widehat{V_i}(v_i) \qquad (2.1)$$

$$S_{v_i}^2 = \frac{1}{N-1}\sum_{n=0}^{N}\left(v_{i,n} - V_i^{\Sigma}\right)^2 = \widehat{\sigma_i^2}(v_i) = RSM_i^2 \qquad (2.2)$$

Where V_i^{Σ} is the sample average, and S_i^2 is the sample variance.

By means of each estimator, a confidence interval for the average and variance can be computed, and the real value of the flow field average quantities can be estimated.

In this case the positioning errors are not considered, because the deformation is already taken into account time by time by a transformed coordinate system, and the traversing errors are lower than 1/100 mm. Concerning the measurement volume sizes, they are lower than 1 mm and compared with the minimum space step, which is 2 mm, it is sure that the volumes do not overlap. Considering the very slight gradients, due to the not so high Re, it could be concluded that the measurement volume errors are negligible.

A model of distribution for measurement error is the uniform distribution with error $\varepsilon \sim U(-0{,}005; 0{,}005)$.For this second distribution a stronger hypothesis is needed. Its parameters are not unknown and no estimation is necessary. So the sampled variable $D_i$is a combination of two distributions $D_i = v_i(1 + \varepsilon)$ but we are only interested in $v_i = f(D_i, \varepsilon_i) = D_i/(1 + \varepsilon_i)$.

Making the hypothesis that D_i has a Gaussian-like distribution and considering a Taylor approximation, the average of the velocity $E[v_i]$ can be defined as function of D_i.

$$E[v_i] = E[f(D_i, \varepsilon_i)] \cong f(E[D_i], E[\varepsilon_i]) = E[D_i] \tag{2.3}$$

$$v_i = f(D_i, \varepsilon_i) = v_i^0 + \frac{\partial f}{\partial D_i}(D_i - E[D_i]) + \frac{\partial f}{\partial \varepsilon_i}(\varepsilon_i - E[\varepsilon_i]) \tag{2.4}$$

In order to express a confidence interval for v_i applying a Taylor expansion around the average the $f(D_i, \varepsilon_i)$ is obtained

$$v_i = f(D_i, \varepsilon_i) = v_i^0 + \frac{\partial f}{\partial D_i}(D_i - E[D_i]) + \frac{\partial f}{\partial \varepsilon_i}(\varepsilon_i - E[\varepsilon_i]) \tag{2.5}$$

If D_i and ε_i are not correlated (no covariance), and approximating the generic variance σ with sampling variance S, the equation (2.5) could be written as

$$S_{v_i} = S_f = \sqrt{\left(\frac{\partial f}{\partial D_i}\right)^2 s_{D_i}^2 + \left(\frac{\partial f}{\partial \varepsilon_i}\right)^2 s_{\varepsilon_i}^2} \tag{2.6}$$

$$\begin{aligned} S_{v_i} &= S_f \\ &= \sqrt{\left(\frac{1}{1 + E[\varepsilon_i]}\right)^2 \frac{{S_{D_i}}^2}{N} + \left(-\frac{E[D_i]}{(1 + E[\varepsilon_i])^2}\right)^2 \frac{\sigma_{\varepsilon_i}^2}{N}} \\ &= \frac{1}{\sqrt{N}} \frac{E[D_i]}{1 + E[\varepsilon_i]} \sqrt{\frac{{S_{D_i}}^2}{{D_i}^2 \cdot N} + \frac{\sigma_{\varepsilon_i}^2}{(1 + E[\varepsilon_i])^2 \cdot N}} \end{aligned} \tag{2.7}$$

From the previous ones the following relation is obtained

$$\frac{\mathrm{RMS_i^2}}{\mathrm{D_i}^2 \cdot \mathrm{N}} \gg \frac{\sigma_{\varepsilon_i}^2}{(1+\varepsilon_i)^2 \cdot \mathrm{N}} \tag{2.8}$$

and finally $\mathrm{S_{v_i}} \cong \mathrm{S_{D_i}} = \mathrm{RMS_i}$

In this way the following intervals for average velocity $\mathrm{V_i}$ and turbulence $\sigma_{\mathrm{v_i}}$ are computed for confidence level of 95%

$$\left(\mathrm{V_i^{\Sigma}} - \frac{\mathrm{t_{N,95\%}} \cdot \mathrm{S_{D_i}}}{\sqrt{\mathrm{N}}} < \mathrm{V_i} < \mathrm{V_i^{\Sigma}} + \frac{\mathrm{t_{N,95\%}} \cdot \mathrm{S_{D_i}}}{\sqrt{\mathrm{N}}}\right) \tag{2.8}$$

$$\left(\frac{(\mathrm{N}-1) \cdot {\mathrm{S_{D_i}}}^2}{\chi^2_{\mathrm{N}-1,2.5\%}} < {\sigma_{\mathrm{v_i}}}^2 < \frac{(\mathrm{N}-1) \cdot {\mathrm{S_{D_i}}}^2}{\chi^2_{\mathrm{N}-1,97.5\%}}\right) \tag{2.8}$$

2.4. ALIGNMENT OPERATIONS

The chosen coordinates system is constituted by an origin on the center of the central jet exit (O), with stream-wise direction x positive towards the plenum, the span-wise direction (y) and wall-normal direction (z) positive with the right-hand rule and towards bottom plenum, respectively.
The handling system is based on different coordinates x^t, y^t and z^t from the physical ones x, y and z. In order to minimize this difference between the origins of the coordinate systems some velocity profiles at 1D are collected and placed at the center in the y and z coordinate of the vertex. Concerning the x-coordinate the geometrical plenum entry has been chosen as origin (x=0). In

order to align the physical system and the traversing system, a series of laser scans along x-axis have been made to verify that the plane identified by the laser beams would always be the same of the side internal walls. The oscilloscope has been used to identify if at z constant the signal of wall reflection changes or not, to evaluate if the glass is not curved. From this analysis, an angle between x and x^t in $xz - plane$ of 0.52° is detected, with a precision lower than ¼ degree. Adopting the reasonable hypothesis for which $Vx(\bar{x},\bar{y},\bar{z}) \gg Vy(\bar{x},\bar{y},\bar{z})\ \forall\ \bar{x},\bar{y},\bar{z}$, the true value of Vx can be estimated dividing the results with the coefficient $\cos(0.52°) = 0.999959 \cong 1$, showing a negligible effect of the angle on the velocity value.

2.5. NUMERICAL APPROACH

Computational Fluid Dynamics (CFD) is a branch of fluid dynamics which uses numerical algorithms in order to obtain a well approximated solution of Navier Stokes equations.
Three main different approaches for turbulence modeling are used on CFD: Direct Numerical Simulation (*DNS*), Large Eddy Simulation (*LES*) and Reynolds Average Navier-Stokes Simulation (*RANS*).
DNS numerically resolves Navier-Stokes equations, without any modeling support. For this reason, in order to capture the smallest turbulence structures, it needs high spatial grid resolution lower than characteristic turbulence length. This actually means very high computational costs, limited *Re* number values and simple geometries, far from industrial applications.
LES simulates only the larger turbulence structures and models the smaller ones requiring a lower computational cost than DNS approach.
RANS models all turbulence structures giving the main information about the average variables. It is the approach that requires the lowest computational effort, and for this reason it is widely used in industrial applications. Unsteady RANS (URANS) approach is also used for taking care of the temporal variation of average quantities.
In Figure (2.6) the main differences among *RANS*, *URANS* and *LES* are schematically represented, while the DNS approach is not reported, because able to resolve the global energy scale (Global in Figure (2.6)).

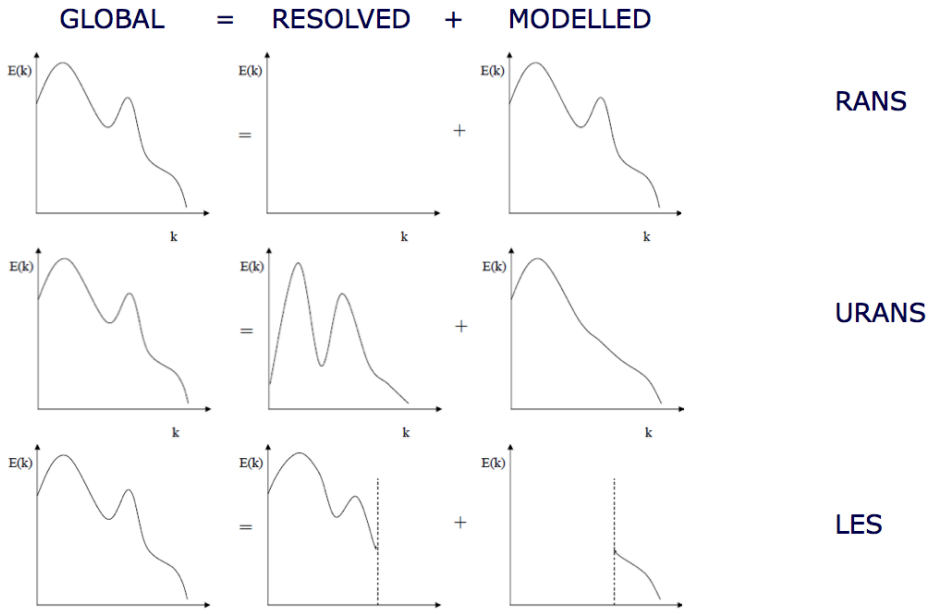

Figure 2.6 Resolved and modeled scales for RANS, URANS and LES

2.5.1. RANS MODELS

Given a case in which it is possible to assume that all the fluctuations do not have a preferential direction, the turbulence may be treated as follows. This approach requires a modeling of main physical quantities that is treated by the *RANS* closure problem, related with the covariance of the fluctuations, alias the Reynolds stress tensor. This modeling approach decreases its accuracy as the complexity of the turbulence phenomenon increases, for example in strongly anisotropic flows. Here the analytical steps to get the RANS equations are briefly recalled (*50*)

$$\varphi(x,t) = \phi(x) + \varphi'(x,t) \tag{2.9}$$

where $\varphi(x,t)$ is a generic field variable, composed by the time average value ϕ

$$\phi(x) = \lim_{\Delta t \to \infty} \frac{1}{\Delta t} \int_0^{\Delta t} \varphi(x,t)\, dt = \overline{\varphi(x,t)} \tag{2.10}$$

and the fluctuation $\varphi'(x,t)$.

From this definition some important properties are derived

$$\overline{\overline{\varphi'(x,t)}} = 0 \tag{2.11}$$

$$\overline{\overline{\varphi'(x,t)}\,\overline{\psi'(x,t)}} \neq 0 \tag{2.12}$$

And applying the ergodicity hypothesis

$$\begin{aligned} \varphi_{rms} &= \frac{1}{N-1}\sum_{n=1}^{N}\left(v_{i,n} - V_i\right)^2 = \overline{\varphi'(x,t)^2} \\ &= \lim_{\Delta t\to\infty}\sqrt{\frac{1}{\Delta t}\int_0^{\Delta t}(\varphi'(x,t))^2 dt} \neq 0 \end{aligned} \tag{2.13}$$

Finally the average kinetic energy and the turbulent energy can be defined

$$E = \frac{1}{2}(U^2 + V^2 + W^2) \tag{2.14}$$

$$E' = k = \frac{1}{2}(u_{rms}^2 + v_{rms}^2 + w_{rms}^2) \tag{2.15}$$

and splitting all the variables in the average and fluctuation components, the unsteady Navier Stokes equation can be rewritten as

$$\frac{\partial \bar{\rho}}{\partial t} + \nabla\cdot(\bar{\rho}\vec{\bar{V}}) \tag{2.16}$$

$$\begin{aligned} &\frac{\partial \bar{\rho}\vec{\bar{V}}}{\partial t} + \nabla\cdot\left(\bar{\rho}\vec{\bar{V}}\vec{\bar{V}}\right) \\ &\qquad = -\nabla\bar{P} + \nabla\cdot\left(\mu\nabla\vec{\bar{V}}\right) + \tau_{Re} + Source \end{aligned} \tag{2.17}$$

where the following notation for tensorial product $\vec{\vec{V}}\vec{\vec{V}} = \vec{\vec{V}} \otimes \vec{\vec{V}}$ is used

$$\tau_{Re} = -\begin{bmatrix} \overline{\frac{\partial \rho u'^2}{\partial x}} & \overline{\frac{\partial \rho u'v'}{\partial y}} & \overline{\frac{\partial \rho u'w'}{\partial z}} \\ \overline{\frac{\partial \rho u'v'}{\partial x}} & \overline{\frac{\partial \rho v'^2}{\partial y}} & \overline{\frac{\partial \rho v'w'}{\partial z}} \\ \overline{\frac{\partial \rho u'w'}{\partial x}} & \overline{\frac{\partial \rho v'w'}{\partial y}} & \overline{\frac{\partial \rho w'^2}{\partial z}} \end{bmatrix} = \nabla \cdot (\overrightarrow{V'V'}) \qquad (2.18)$$

The Reynolds tensor is the term which needs to be modeled in order to resolve the closure problem in the RANS approach. The resulting terms $-\overline{\rho u'_\iota u'_J}$ hide the dynamic of the fluctuation in terms of momentum, creating six additional unknowns plus the turbulent viscosity ν_t.
In order to model the Reynolds stress tensor in RANS approach the Boussinesq approximation, where the turbulent stresses are linked to the mean flow parameters, is widely used

$$\begin{aligned} -\overline{\rho u'_\iota u'_j} &= \nu_t \left(\frac{\partial \overline{u_\iota}}{\partial x_j} + \frac{\partial \overline{u_j}}{\partial x_i} \right) - \frac{2}{3} E' \delta_{ij} \\ &= \nu_t S_{ij} - \frac{2}{3} E' \delta_{ij} \end{aligned} \qquad (2.19)$$

This approximation is used in many two-equation family models, where the main difference is in the formulation of the quantity ν_t. Other models do not use this approximation basing the modeling on additional turbulence quantities transport equations or separately resolving each stress component of the tensor. In order to better understand the main characteristics and differences among the used numerical models, a brief description is reported, coherently with (*50*).

- k-ε

k-ε with its standard formulation is a very used historically for its stability. It is a two-equation model, where ε, the energy dissipation variable, is used in addition to the turbulence kinetic energy *k* to determine the turbulence length

scale. Although this model is optimized for the main test cases often it fails predicting phenomena with the presence of adverse pressure gradient or in general when the velocity gradient is very high, such as for recirculation phenomena.
The K-ε RNG and Realizable are two-equation models of the k-ε family where the modeling of the Reynolds stress model is improved for complex phenomena, such as recirculation, detachment and reattachment flows, swirl..

- k-ω

In 1988 Wilcox proposed a two-equation model with a length variable based on the turbulence frequency ω. It works better than the $k-\varepsilon$ standard formulation with adverse pressure gradients, but some issues are present in free stream boundary conditions. Differently from the $k-\varepsilon$ family models presented above the k-ω does not require any additional model for the zones close to the wall (near-wall treatment function).

- k-ω SST

This two-equation model uses the $k-\varepsilon$ formulation for the free stream zones and the $k-\omega$ approach near the wall. This coupling combines the skills of the two methods in order to improve the performance with the presence of adverse pressure gradient, to have reliable results near the wall, and to avoid any required calibration of the turbulence frequency in free stream.

- Reynolds Stress Model (RSM)

It is the most complex *RANS* model with its seven differential equations. It consists in solving directly transport equations for the Reynolds stress tensor components taking into account the directional effect of the Reynolds stress field. It is a compromise between accurate results and computational costs compared with two-equation RANS models and LES approach.

- Low Reynolds Models

These models differ from the so called "high Reynolds models" because of the wall treatment. Low Reynolds Models are based on the inclusion of the main formulation of specific damping functions able to avoid the use of wall functions by using a finer grid near the wall (dimensionless wall distance $y^+ < 1$) capturing the viscous effects dominant in this zone.

- $v^2 - f$

This model belongs to the group of low Reynolds models. It is similar to the standard $k - \varepsilon$ but aims to improve the results for anisotropic turbulence flows and for non–local pressure strain effect. Transport equation for $\overline{v^2}$, which could be thought as a velocity fluctuation normal to the streamlines, instead of k is solved. The anisotropy effects are modeled by the Helmotz elliptic equation for the relaxation factor *f*.

- Non Linear Eddy Viscosity Model

It is an advanced two-equation model that overcomes the Boussinesq approximation with a third order formulation for Reynolds stress term. This approach permits to obtain more accurate results respect to standard two-equation models for phenomena with adverse pressure gradient, secondary Taylor flows, abrupt changing of mean flow direction.

2.5.2. LARGE EDDY SIMULATION

Large Eddies Simulation (*LES*) solves the large scales of the flow, representing the anisotropic scale, and models only the small turbulence scales, typically isotropic. LES approach applies a low-pass filter G on the entire dominion in order to eliminate the events that have a scale smaller than Δ. The mathematical aspect of the filter is a convolution between φ, and G, the convolution kernel.

$$\begin{aligned}\langle\varphi\rangle(x,t;\Delta) &= \int_{\Re^3} G(r,x;\Delta)\varphi(x-r,t)dr \\ &= \int_{\Re^3} G(x-r,\Delta)\varphi(x,t)dr\end{aligned} \tag{2.20}$$

It is hence possible to decompose any field variable in the formulation

$$\varphi(x,t) = \langle\varphi\rangle(x,t;\Delta) + \varphi^{SGS}(x,t;\Delta) \tag{2.21}$$

where $\varphi^{SGS}(x,t;\Delta)$ is the filtred variable which LES method does not simulate. If the time dimension is also included the filter is reformulated as

$$\begin{aligned}\langle\varphi\rangle(x,t) &= \int_{\Re^3}\int_{t'=0}^{+\infty} G(x-r,t-t',\Delta,\bar{\tau})\varphi(r,t')drdt' \\ &= G * \varphi\end{aligned} \tag{2.22}$$

where Δ and $\bar{\tau}$ are the cut-off length in space and in time. The same definition can be obtained applying a Fourier transform using as cut-off variables k_c and ω_c, spatial wave number and frequency, respectively.

$$\langle\hat{\varphi}(k,\omega)\rangle = \hat{\varphi}(k,\omega)\hat{G}(k,\omega) \tag{2.23}$$

Assuming that these cut-off values are constant all over the domain the filtered Navier-Stokes equations for incompressible flow written in Einstein notation are

$$\frac{\partial\langle u_i\rangle}{\partial t}+\frac{\partial}{\partial x_j}\left(\langle u_i u_j\rangle\right)=-\frac{1}{\rho}\frac{\partial\langle p\rangle}{\partial x_j}+\frac{\partial}{\partial x_j}\left(2\nu\langle S_{ij}\rangle+T_{ij}\right) \quad (2.24)$$

Where $T_{ij}=\langle u_i\rangle\langle u_j\rangle-\langle u_i u_j\rangle$ is the tensor including the momentum exchange between the two scales. Like in the RANS approach an approximation made by Boussinesq is used on this approach for modeling T_{ij}defining it in term of eddy viscosity

$$T_{ij}=2\nu_t(x,t)\langle S_{ij}\rangle+\frac{1}{3}T_{ii}\delta_{ij} \quad (2.25)$$

where instead of the average tensor of the velocity the sub grid tensor is related to the over grid tensor $\langle S_{ij}\rangle$.

Defining macropressure $\langle P\rangle=\langle p\rangle-\frac{1}{3}\rho T_{ii}$ it is possible to write the final form of filtered Navier-Stokes equations with Boussinesq hypotesis.

$$\begin{aligned}\frac{\partial\langle u_i\rangle}{\partial t}+\frac{\partial}{\partial x_j}\left(\langle u_i u_j\rangle\right)&\\ =-\frac{1}{\rho}\frac{\partial\langle P\rangle}{\partial x_j}&\\ +\frac{\partial}{\partial x_j}\left((\nu+\nu_t)\left(\frac{\partial\langle u_i\rangle}{\partial x_j}+\frac{\partial\langle u_j\rangle}{\partial x_i}\right)\right)&\end{aligned} \quad (2.26)$$

The most important eddy viscosity model was proposed by Smagorinsky assuming, as in the Prantdl mixing length theory, that ν_t is proportional to a characteristic velocity and turbulence characteristic length Δx, both of the sub-grid domain.

$$\nu_t=C_s\Delta_{sgs}u_{sgs}=\left(C_s\Delta_{sgs}\right)^2\sqrt{2\langle S_{ij}\rangle\langle S_{ij}\rangle} \quad (2.27)$$

The references for this analysis are *Large eddy simulation for uncompressible flow (51)* and *Large-eddy simulations of turbulence(52).*

ON VORTEX DETECTION

In order to define a phenomenon as vortex, two main characteristics must be present (*53*):

1. a vortex core must have a net vorticity and so $\omega = \nabla \times u \neq 0$.
2. the definition of a vortex must be a Galilean Invariant.

This second point is related to the observation that in a particular translating frame system, the vortex describes a closed or swirl-shaped path. Spalart in 1988 suggested using vorticity magnitude $|\omega|$ as an indicator of the vortex presence. Although this definition could seem correct and simple, it hides a great problem: the indicator $|\omega|$ does not distinguish the vorticity due to the real swirl of the fluid and the one due to the shear layer. The classical Couette flow is an example of this limit, where the vorticity is indeed only due to the shear layer. Chong *et al* (1990) proposed to overcome the problem of the Galilean invariance evaluating the eigenvalues of ∇u, and the presence of complex values that guarantee the presence of vortices. Defining the first, second and third invariant of ∇u as

$$P = Tr(\nabla u) \tag{2.28}$$

$$Q = \frac{1}{2}(Tr(\nabla u)^2 - \nabla u \nabla u^T) \tag{2.29}$$

$$R = \det(\nabla u) \tag{2.30}$$

the eigenvalues problem can be written as

$$\Delta = \left(\frac{1}{3}Q\right)^3 + \left(\frac{1}{2}R\right)^2 > 0 \tag{2.319}$$

Hunt *et al* (1988) proposed to define the vortex as a region in which Q, the second invariant of ∇u, is positive, with the additional condition that the pressure has to be lower than the surrounding value. Another way to detect a vortex was proposed by Jeong and Hussain *et al* (1995), the criterion called $\lambda_2 - criterion$, referring to the tensor $S^2 + \Omega^2$, where S is the symmetric part of ∇u and Ω the antisymmetric one

$$S = \frac{1}{2}(\nabla u + \nabla u^T) \tag{2.32}$$

$$\Omega = \frac{1}{2}(\nabla u - \nabla u^T) \tag{2.33}$$

It is proved that, if the tensor $S^2 + \Omega^2$ has two negative eigenvalues, the region has a local minimum of the pressure in the plane of the eigenvectors associated. Because of $S^2 + \Omega^2$ is a symmetric tensor the eigenvalue are all real and it is possible to write

$$\lambda_1 \geq \lambda_2 \geq \lambda_3 \tag{2.34}$$

and a vortex is detected if $\lambda_2 < 0$.

3. Physical and numerical problem setting

This chapter reports the experimental and numerical settings for the main characteristics of the facility and of the test-section. In the last part the setting of RANS models and LES (carried out by (*49*)) are presented.

3.1. FACILITY STRUCTURE

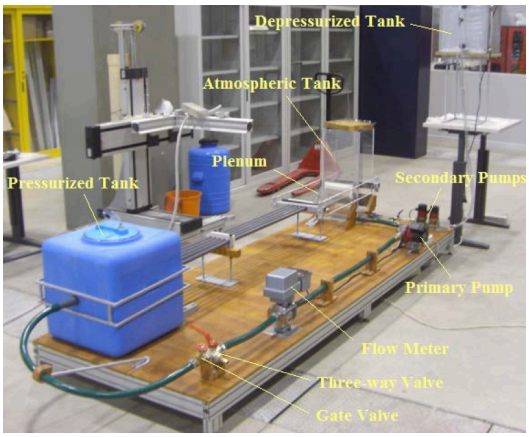

Figure 3.1 Experimental Facility

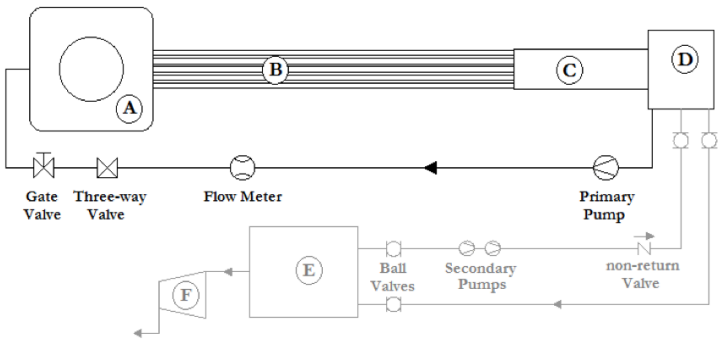

Figure 3.2 High view scheme of the hydraulic system

The facility is composed by a primary circuit (black) and a secondary one (gray) (Figure (3.1)). Primary circuit has the role to create a circulation of water which feeding the test section. It consists mainly of a primary pump, a pressurized tank (A) and an atmospheric tank (D), five pipes (B), and the test section(C). The

secondary circuit has the function to desorb and eject the air dissolved in the water to avoid the generation of bubbles in the test section, which can produce a "lens effect" on the laser beams. It consists of a dry vacuum compressor (F), a sub-atmospheric chamber with a vacuometer, and two pumps to inject the depurated water in the primary circuit, overcoming the opposite pressure gradient. In both circuits different valves are inserted in order to regulate the operative parameters, as shown in Figure (3.2).

3.2. PLENUM PARAMETERS

The plenum is characterized by the inlet wall with five holes permitting the connection with the feeding pipes, and a honeycomb outlet in order to avoid uneven influence of downstream conditions on the plenum flow map (Figure (3.3)).

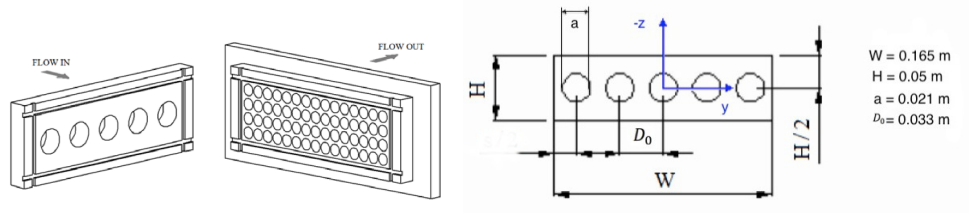

Figure 3.3 Plenum inlet, outlet representation and inlet frontal view

Two parameters are important for the inlet wall: the dimensionless distance between jets $D_0/a = 1.5714$ and dimensionless distance from the centerline to the wall $W/a = 1.1905$.

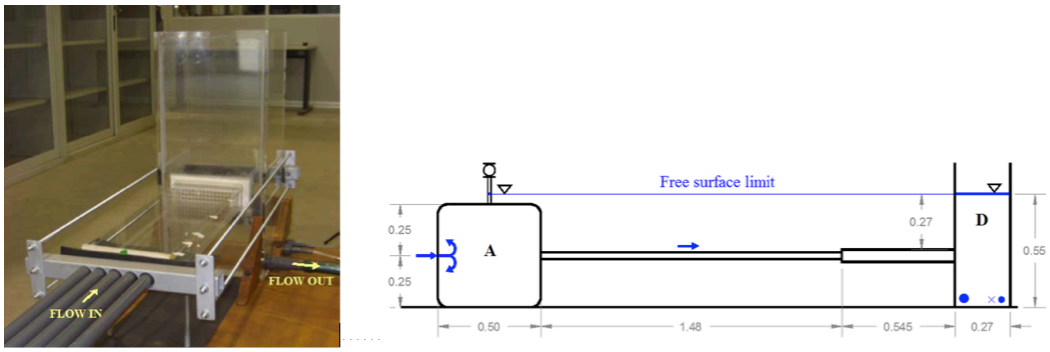

Figure 3.4 Plenum view and levels

The chosen materials are important in terms of accuracy of the measurements. The upper surface, through which light of the laser sources reflects carrying the information about the velocity of the particles, is a transparent high-purity quartz glass, optically isotropic and homogeneous avoiding the possible alterations of the reflected laser light due to the crystalline structure of the glass itself. The remaining three walls are made of basic transparent glass. The walls are assembled by silicon in order to avoid leakage. Screw tie rods are used to reinforce the plenum and keep it firmly connected to the atmospheric tank and avoid any kind of vibration, which can disturb the measurements and damage the glasses. An overall view of the plenum is represented in Figure (3.4). In general the geometrical tolerance for the plenum is lower that $1\ mm$ and the measurement accuracy is $0.1\ mm$. A vernier caliper is used for measurements.

PROCEDURE AND PARAMETERS FOR THE HYDRAULIC SYSTEM

The working fluid is water, and its density and dynamic viscosity are functions of the temperature, which depends on the ambient temperature and on the energy balance due to the work of the pump entering in the fluid.

Temperature average	293,15	K
Density	998	Kg/m^3
Viscosity	0,001	$Kg/m \cdot s$

Tab. 3.1 Water properties

Between 15°C and 25 °C the density and the viscosity of water are nearly constant (maximum variation of viscosity around 5%).

The total mass of water is around the 200 kg. In the case of adiabatic system and with the pump at nominal power, the required time in order to have an increment of 1K for the water temperature is

$$m(C\Delta T) = \dot{L}\Delta t$$

$$\Delta t = \frac{mC\Delta T}{\dot{L}} = 33488\ s = 9h\ 20\ m$$

For this reason, the temperature is steady and properties do not change significantly.

In order to know the characteristic curve of the hydraulic system a series of flow-rate measurements are taken at different power level of the primary pump operating in the head selection mode. The measurements have shown the following results averaging the mass flow rate sampling for a minute (Graph. (3.1))

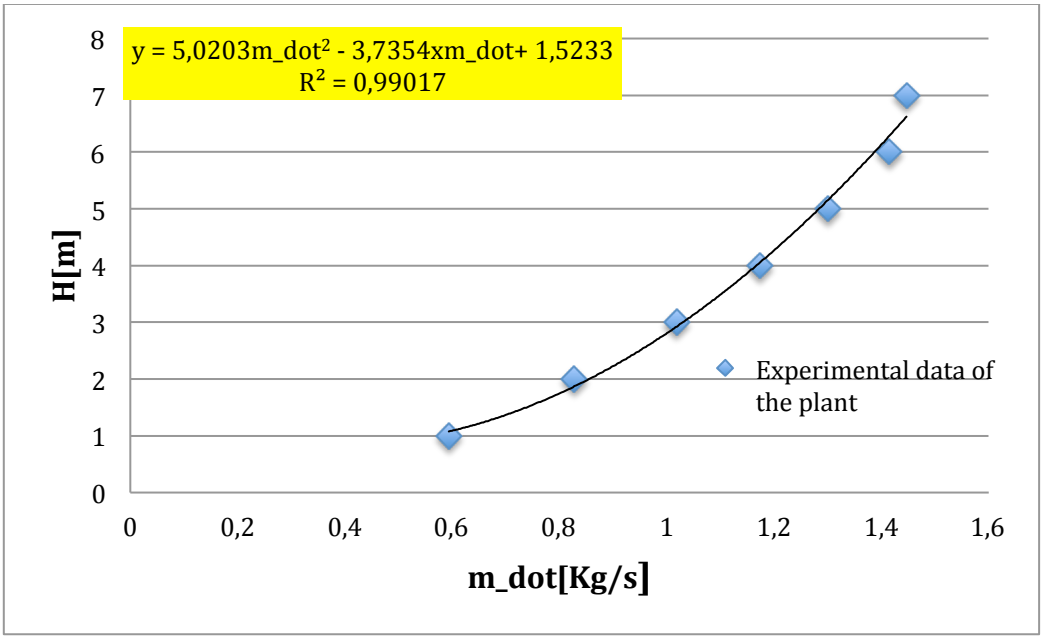

Graph. 3.1 Plant characteristic

The nominal point for the experimental campaign is for $\dot{m} = 0{,}828\ ^{kg}/_{s}$. During the experimental campaign is detected a variation of this curve which cause a flow rate of 2% of the nominal value.

Concerning the pumps, the dry vacuum compressor, and the tanks see "Experimental and Numerical Analysis of Confined Parallel Jets"(*49*).

The procedure of filling is reported here:

1. Fill the circuit with water through the atmospheric tank till the level reaches the value represented in the Figure (3.4).
2. Close the valve on the top of the atmospheric tank in order to maintain the same level inside.
3. Go on to fill the circuit till the level in atmospheric tank has grown for other 0.3 m more and than stop to fill.
4. Check if the valves, which link the primary to the secondary circuit, are closed. If they are not, close them.
5. Switch on the Dry Vacuum Compressor and wait that the vacuometer reach the value of $0{,}39\ atm$ and try to stabilize the pressure on this value acting manually on the intake valve on the top of the sub-atmospheric tank.
6. Open both suction valves, check if the water level in the sub-atmospheric tank is increasing through the graduated pipe on the left, go on till the water level is around 10 cm and than close the suction valves.
7. Open the valve in the feeding pipe, switch on the secondary pumps, check if the level of the sub-atmospheric tank is decreasing and open completely one suction valve and partially the other stabilizing the flow rate through the sub-atmospheric tank in a quasi-steady condition.
8. Switch on the primary pump on the desired level.
9. Wait till the bubbles in the plenum decrease as desired.
10. Reverse in the fluid though the atmospheric tank a certain amount of glass spheres
11. Cover the atmospheric tank with the cap in order to limit the absorption of air by water.

OPERATIVE PARAMETERS FOR THE HYDRAULIC SYSTEM

Atmospheric tank level	0,55	m
Sub-atmospheric tank level	0,1	m
Sub-atmospheric tank pressure	0,71	atm

Tab. 3.2 Levels data

It is important to note that the water level has to be around the indicated levels just for a confortable management of the operations but it is not strictly

necessary. The reason lies in the fact that after the closure of the pressurized tank valve, the level on the atmospheric tank pressurized the whole system. For this reason the test section has the same ΔP (pressure drop) for a fixed head setting, independently of water level, therefore the flow map is not modified.

3.3. Numerical Setting

RANS MESH AND COURANT NUMBER

- 1250747 cells
- $5.897064 \cdot 10^{-8} m^3$ of max cell volume
- $2.149282 \cdot 10^{-13} m^3$ of min cell volume
- 99,94% of cells have *equisize skewness* and *equiangle skewness* lower than 0,4
- the maximum *aspect ratio* is 170, with the 51,677% has AR >10.
- The *size ratio* is maintained almost everywhere lower than 1.55, with some peaks higher than 2 in the conjunction between boundary layers and the remaining part of the face mesh (Figure (3.5)).

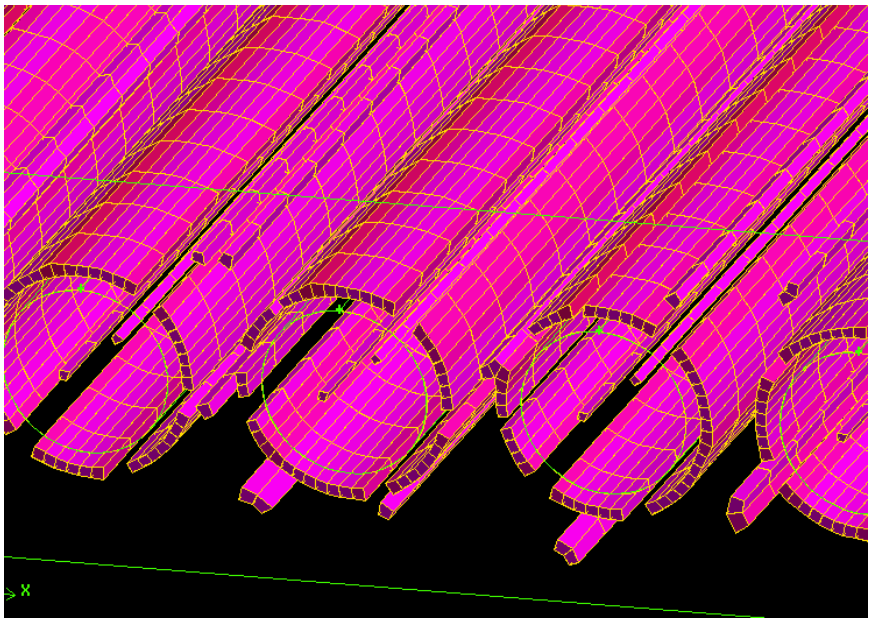

Figure 3.5 Cells with 2<SR<3

The verification of the steadiness of the solution is verified by a sensibility analysis on Courant number.

$$CFL = \frac{v\Delta t}{\Delta x} \tag{3.1}$$

For $k-\omega\ SST, k-\varepsilon\ RNG$ and V^2f is performed an unsteady *RANS* with a time steps Δt which ensures $CFL < 1$.
Other sessions of simulations are performed with a greater Δt and then in a steady case. A comparison between this three results shows that there is no appreciable difference, confirming the steadiness of numerical results. Therefore only the steady simulation results are reported.

Urans numerical settings

Solver	*Segregated*
Spatial Discretization	
Pressure	*PRESTO!*
Momentum	*Second order upwind*
Gradient	*Least squared based*
$k, \varepsilon, \omega, v^2f, u_iu_j$	*Second order upwind*
Pressure-Velocity coupling	*Fractional steps*
Temporal discretization	Δt *=0.0005 s, Second order implicit*

For *NLEVM* a *PISO* algorithm for pressure-velocity coupling is used.

Rans numerical settings

Solver	*Segregated*
Spatial Discretization	
Pressure	*PRESTO!*
Momentum	*Second order upwind*
Gradient	*Least squared based*
$k, \varepsilon, \omega, v^2, f, u'_iu'_j$	*Second order upwind*
Pressure-Velocity coupling	*Simple*

Inlet velocity conditions

For each *RANS* model, except *RSM* and V^2f, the boundary condition is an inlet velocity profile obtained through a simulation of a pipe with the same geometry with periodic boundary conditions, performed with $k-\varepsilon\ standard$.
Concerning *RSM* and V^2f, the same technique is used, but performed respectively with *RSM* and V^2f models.

LES MESH

The same mesh used in the thesis work of Viaro (*49*) is used.

Les numerical settings

Solver	*Segregated*
Spatial Discretization	
Pressure	*PRESTO!*
Momentum	*Bounded central differencing*
Gradient	*Least squared based*
$u'_i u'_j$	*Second order upwind*
Pressure-Velocity coupling	*Fractional step*
Temporal discretization	Δt *=0,00065 s, Second order implicit*
Fluctuating velocity	*Vortex method(54)*

Inlet velocity conditions

The same technique are used but performed with a Large eddy simulation in a periodic pipe.

4. Results

This chapter reports and compares the results obtained with experimental and numerical approaches. In the first part, after introducing the notation used in the chapter, experimental data are analyzed, evaluating measurement uncertainties, symmetry, stability, deflection, and oscillation presence in the phenomenon. In the second part the experimental results are compared with numerical simulations results of velocities and turbulence quantities obtained by *RANS* and *Les* models (*49*).

4.1.NOTATIONS

A specific notation is used in order to help the reader to quickly understand the physical lines where the measures are represented. For a generic coordinate X:

Xall: measures taken on the whole domain of its coordinate, i.e. [Xmin, Xmax].
Xplus and Xminus: measures taken respectively on [0, Wmax] and [Wmin, 0].

The central jet is conventionally called Jet 0, the two jets on the left looking from the entry of the pipes are Jet -1 and Jet -2, and the two jets on the right are Jet 1 and jet 2. Xji are a slot of measurements taken in front of Jet i.

The reference system with a notation example of is presented in Figure (4.1).

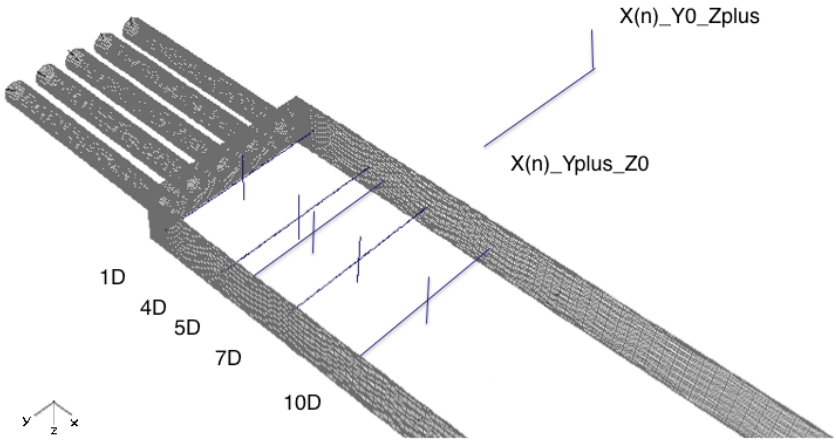

Figure 4.1 Coordinate system with examples of notation

Another notation is used for numerical model names:

- $k-\omega\ SST$ is kw_sst
- $k-\varepsilon\ RNG$ is ke_RNG
- V^2f is v2f
- $k-\varepsilon\ Low\ Reynolds\ Lam-Bremhorst$ is ke_LowRe
- $k-\varepsilon\ Low\ Reynolds\ Launder-Sharma$ is ke_LowRe_2
- $k-\varepsilon\ Realizable$ is Rea
- $Non\ Linear\ Eddy\ Viscosity\ model\ developed\ by\ Mereu\ et\ al$ is NLEV
- $Reynolds\ Stress\ Model$ is RSM
- $Large\ eddy\ simulation$ is LES

4.2. UNCERTANTY

The uncertainty analysis proposed in the second chapter shows the following maximum and average uncertainty for V_x, V_y, RMS_x, and RMS_y on each analyzed diameter. The values reported in Tab. (4.1) and Tab. (4.2) represent the percentage error referred to the bulk velocity.

MAXIMUM UNCERTANTIY

	$errV_x$ (%)	$errV_y$ (%)	$errRMS_x$ (%)	$errRMS_y$ (%)
1D	*3,65*	*5,32*	*1,91*	*2,44*
4D	*5,03*	*15,21*	*3,48*	*7,77*
5D	*3,78*	*4,92*	*2,31*	*2,48*
7D	*5,37*	*7,86*	*2,38*	*3,29*
10D	*2,6*	*6,18*	*0,84*	*1,39*
Global	*4,09*	*7,90*	*2,19*	*3,47*

Tab. 4.1 Maximum uncertainty

AVERAGE UNCERTANTIY

	$errV_x$ (%)	$errV_y$ (%)	$errRMS_x$ (%)	$errRMS_y$ (%)
1D	*1,57*	*2,33*	*0,69*	*0,83*
4D	*2,88*	*4,89*	*1,75*	*2,43*
5D	*2,10*	*2,77*	*1,29*	*1,33*
7D	*2,74*	*3,99*	*1,37*	*1,63*
10D	*1,98*	*3,33*	*0,57*	*0,77*
Global	*2,25*	*3,46*	*1,13*	*1,39*

Tab. 4.2 Average uncertainty

4.3.SYMMETRY, STABILITY AND DEFLECTION

STABILITY

In order to verify the stability, a series of measurements have been taken in X105_Y0_Zall, X105_Yplus_Z-22 for five times stopping the primary pump between one series and the following to avoid correlations. The data reported in the Graph. (4.1), (4.2), (4.3) are referred to the following Re number and coordinate system

Re_D	$Diameter$	$angle\ between\ x\ and\ x^t$	$axis\ used\ for\ graphs$
12000	5	0.52°	x^t

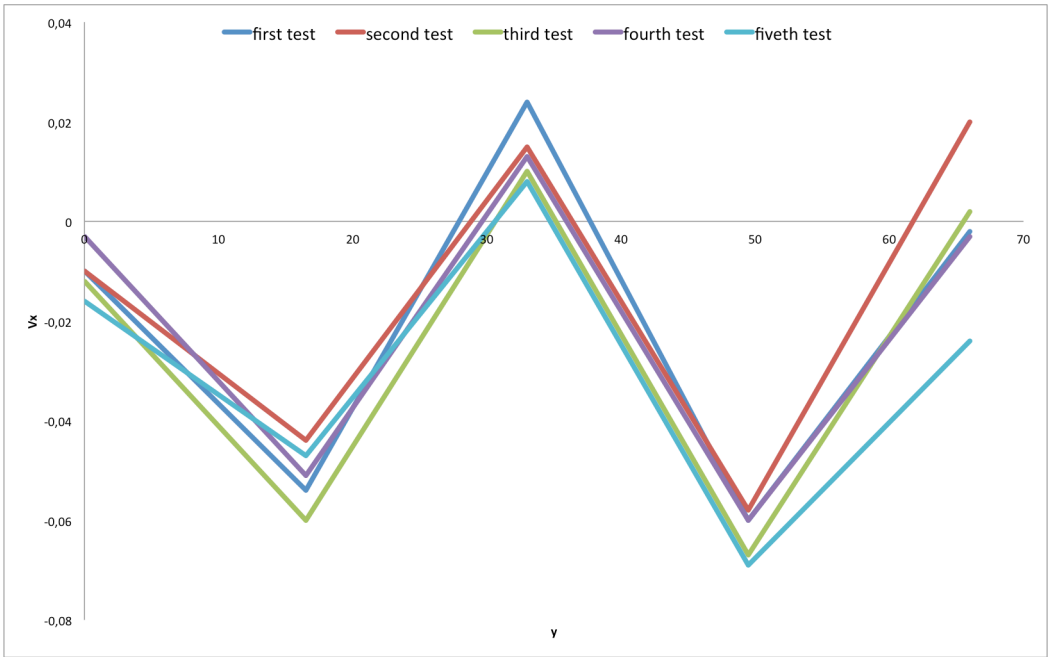

Graph. 4.1 Vx X105_Yminus_Z-22

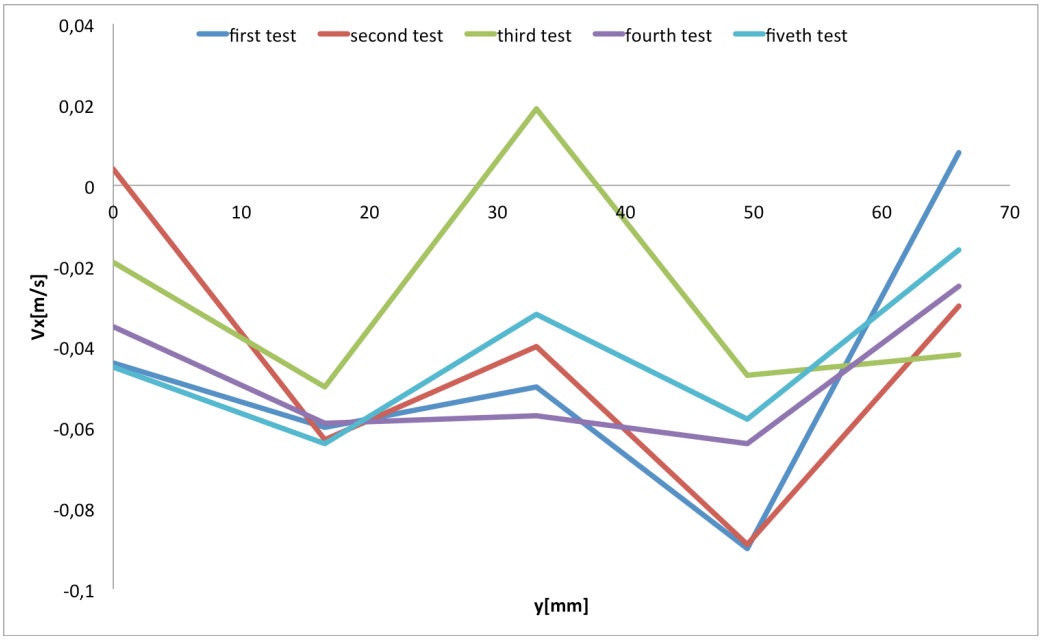

Graph. 4.2 Vx X105_Yplus_Z22

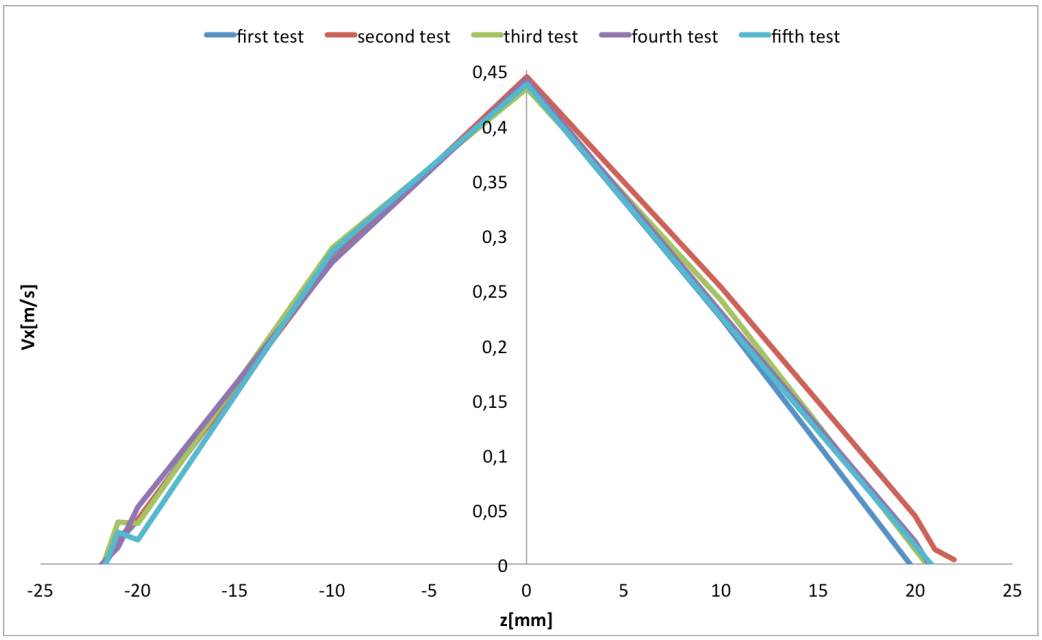

Graph. 4.3 Vx_X105_Y0_Zall

The first and the last graph (Graph. (4.1) and Graph. (4.3)) show that, in all the five cases, the flow behaves in the same way confirming the absence of physical instabilities. Even though the Graph. (4.2) shows a different behavior during the experiments, it could be caused by the very few data collected in the inferior

part of the plenum (Zplus), due to the high glass reflection in this zone. The data collected in the bottom part of the facility, Graph. (4.2), are therefore not sufficient to be taken into consideration in this analysis.

DEFLECTION

In order to evaluate if deflection happens, two sets of measurements have been taken at 1D (X21) and at 5D (X105), as shown in Graph. (4.4-8)). The positions of Vx peaks are checked and the best fitting parabola for each peak and related vertex are carried out (Tab. (4.3)). A similar method is used for Vy, which represents the expansion in y-direction of jets. The inflection of best fitting cubic has to be in the centerline of the jets in case of no deflection, and it has to present values around zero for the span-wise velocity. It would identify a position on which there is no expansion of the jets (Tab (4.4)).

Re	D	$angle\ between\ x\ and\ x^t$	$axis\ used\ for\ graphs$
12000	1	0.52°	x^t

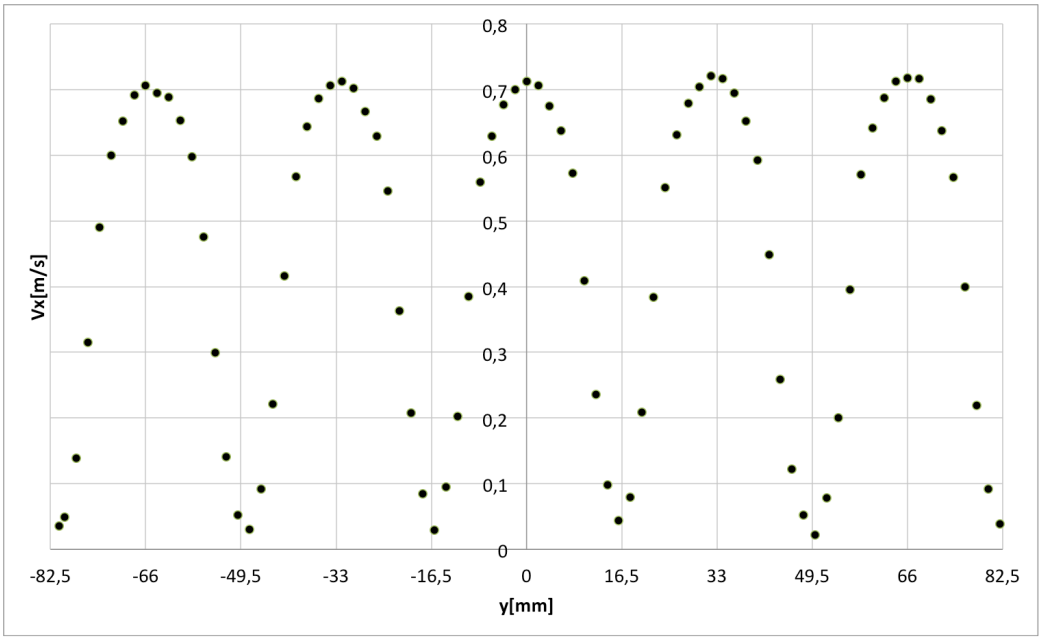

Graph. 4.4 Vx X21_Yall_Z0

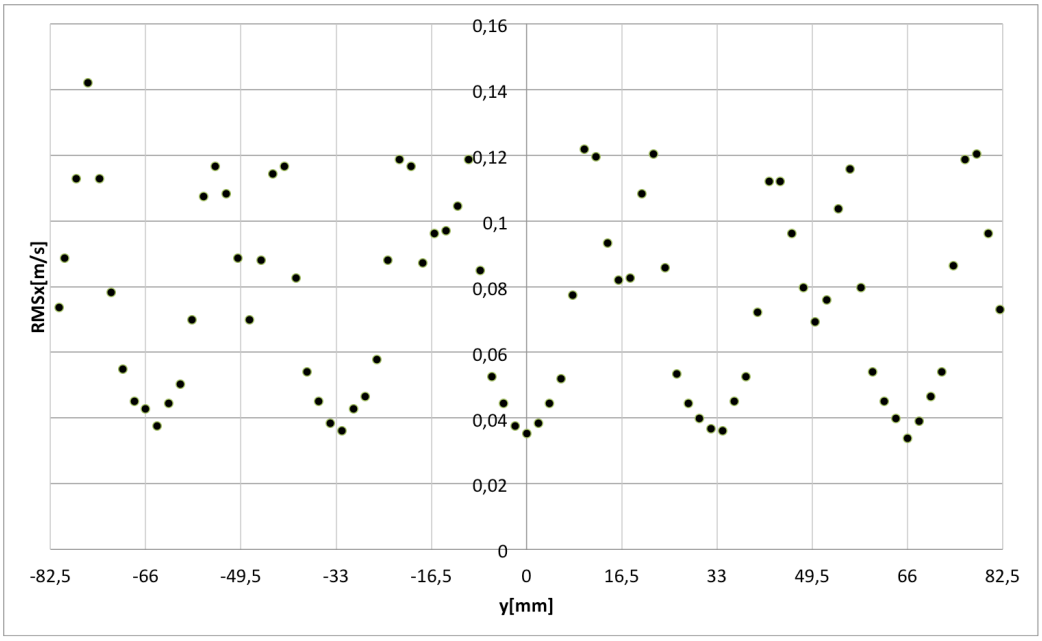

Graph. 4.5 RMSx X21_Yall_Z0

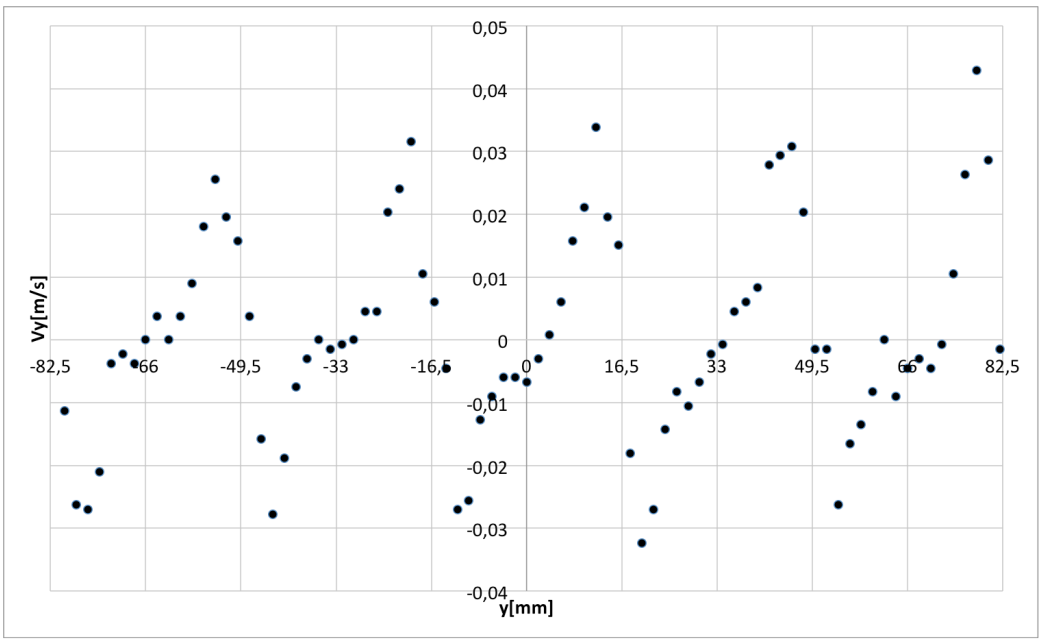

Graph. 4.6 Vy X21_Yall_Z0

Re	D	$angle\ between\ x\ and\ x^t$	$axis\ used\ for\ graphs$
12000	5	0.52°	x^t

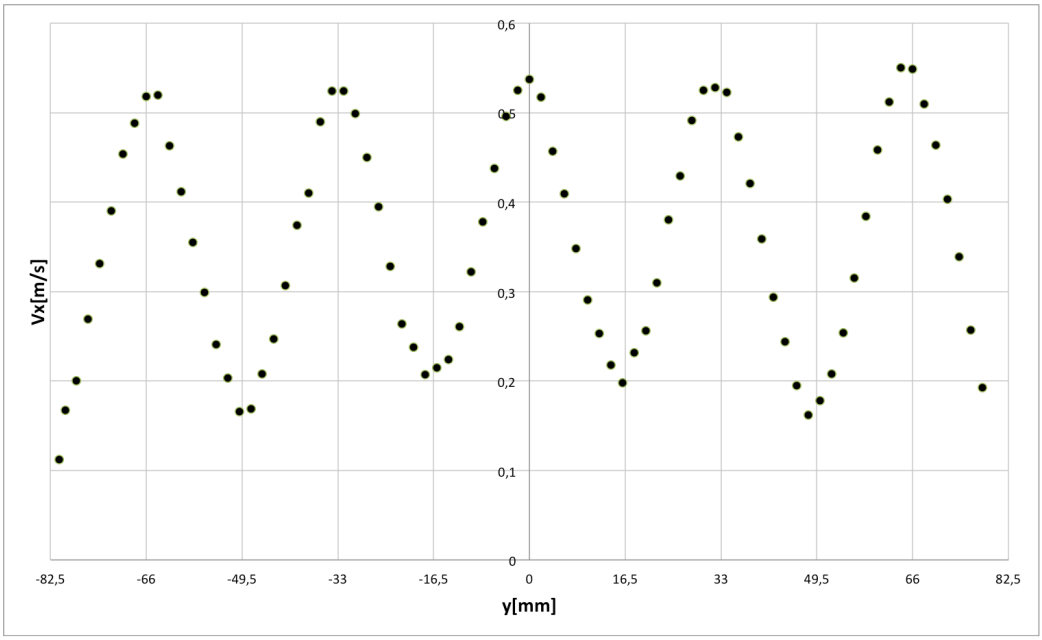

Graph. 4.7 Vx X105_Yall_Z0

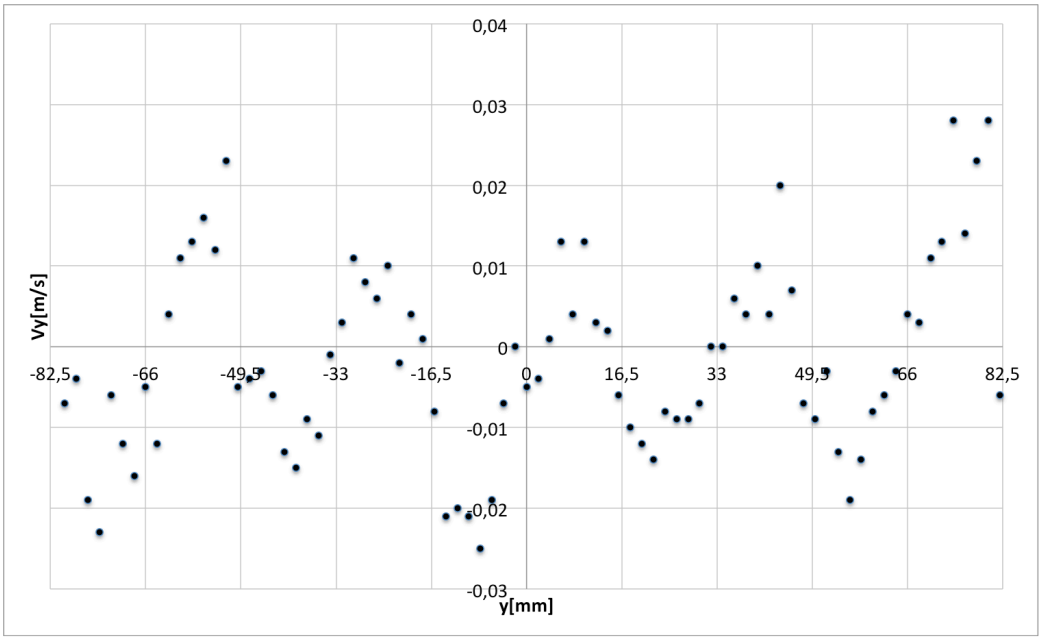

Graph. 4.8 Vy X105_Yall_Z0

$1a$	$J-2$	$J-1$	$J\,0$	$J\,1$	$J\,2$
Vertex	$-65{,}17\ mm$	$-32{,}32\ mm$	$0{,}15\ mm$	$32{,}49\ mm$	$65{,}97\ mm$
Inflection	$-65{,}24\ mm$	$-32{,}33\ mm$	$0{,}76\ mm$	$33{,}05\ mm$	$64{,}55\ mm$
Vertex error	$-0{,}83\ mm$	$-0{,}68\ mm$	$0{,}15\ mm$	$0{,}51\ mm$	$0{,}03\ mm$
Inflection error	$-0{,}76\ mm$	$-0{,}67\ mm$	$0{,}76\ mm$	$-0{,}05\ mm$	$1{,}45\ mm$

Tab. 4.3 Peak of Vx and Inflection of Vy at 1a

$5a$	$J-2$	$J-1$	$J\,0$	$J\,1$	$J\,2$
Vertex	$-65{,}79\ mm$	$-32{,}54\ mm$	$-0{,}45\ mm$	$31{,}76\ mm$	$65{,}38\ mm$
Inflection	$-63{,}67\ mm$	$-34{,}37\ mm$	$0{,}02\ mm$	$35{,}26\ mm$	$65{,}69\ mm$
Vertex error	$-0{,}21\ mm$	$-0{,}46\ mm$	$0{,}02\ mm$	$1{,}24\ mm$	$0{,}62\ mm$
Inflection error	$-2{,}33\ mm$	$-1{,}37\ mm$	$0{,}02\ mm$	$2{,}26\ mm$	$0{,}31\ mm$

Tab. 4.4 Peak of Vx and inflections of Vy in mm at 5a

The deviations have different signs, so no systematic error in the centering operation is revealed. The only signal of deflection is in the different sign of Jet-2 and Jet-1 deviation by the ones of Jet 1 and Jet 2 having the opposite behavior. This suggests the presence of a very slight deflection of the jets, which converge to the center.

SYMMETRY

It is evident looking at Graph.(4.4-8) that globally the flow develops symmetrically respect to X-axis on xy-plane and so no evident breaking are present. Additionally as shown in Graph. (4.6) and in Graph. (4.8) the expansion function has a shape of an odd function. The discrepancy of the velocity vertices and inflection points from the theory are so slight to suggest they could be generated by geometry imperfections. In order to complete the visualization of the flow field a series of data is collected along z direction in front of each jet.

Re	D	$angle\ between\ x\ and\ x^t$	$axis\ used\ for\ graphs$
12000	1	0.52°	x^t

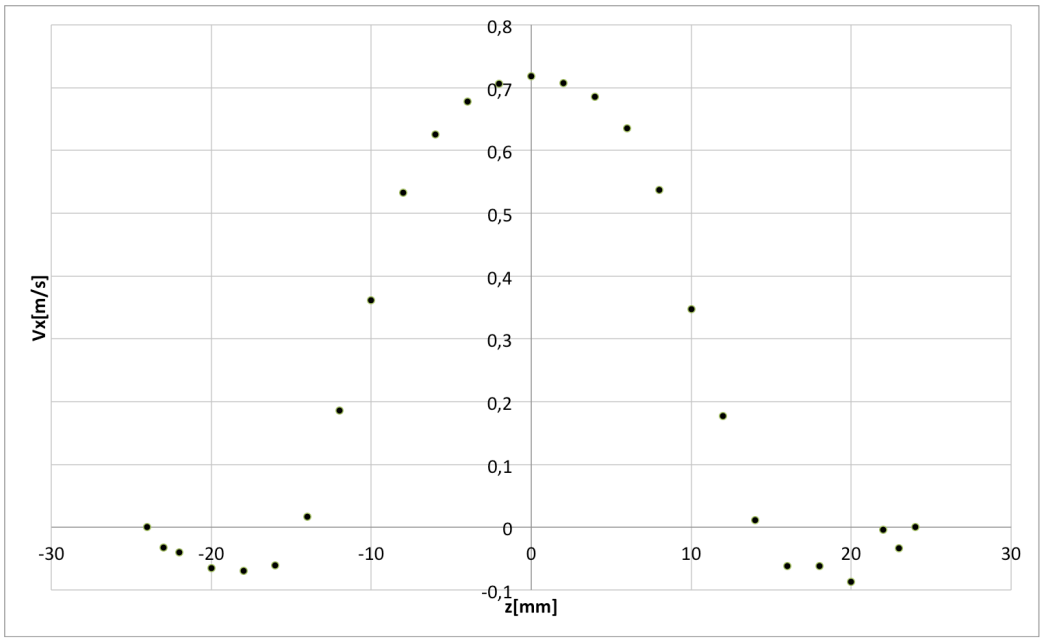

Graph. 4.9 Vx X21_Yjet0_Zall

The profile of the central jet shows a symmetrical shape and suggests the presence of a big recirculation at the top and at the bottom of the chamber (Graph. (4.9)).

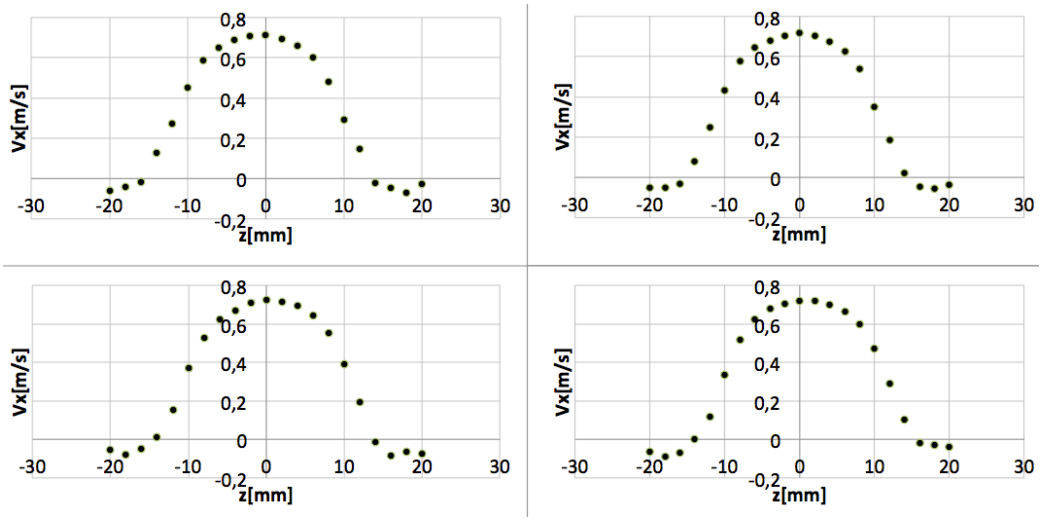

Graph. 4.10 Jet-2, Jet-1, Jet1 and Jet2 Vx profile at 1D

The remaining profiles are coincident with the one of the central jet and the peaks have the same velocity value (Graph. (4.10)) The misalignment has not yet generated its effect because the origin of the system has been chosen as z and y coordinates of the vertex of the central jet parabolic profile at $x = 21\ mm$.
Moreover the vicinity to the origin of the system could hide the asymmetries, in case they exist, because they need a certain distance from inlet in order to develop.

As we can see in Graph. (4.11) and Graph. (4.12) the border values are not the same. This information has to be associated to the deviation o$f\ x^t$ from x which at $x = 105\ mm$ is around $0.76\ mm$. Vx intersect the z-axis for z=[-22.2, +20.5] mm. Taking into account the deviation of 0,76 mm this values become z=[-21.6, 21.4] mm.

Re	D	$angle\ between\ x\ and\ x^t$	$axis\ used\ for\ graphs$
12000	1	0.52°	x^t

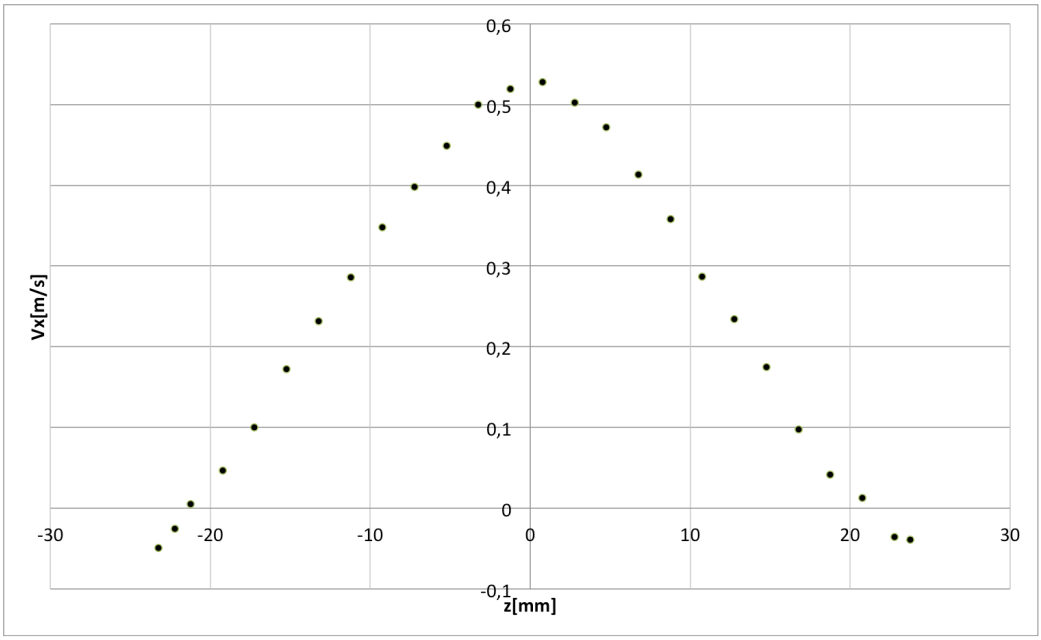

Graph. 4.11 Vx X21_YJet0_Zall

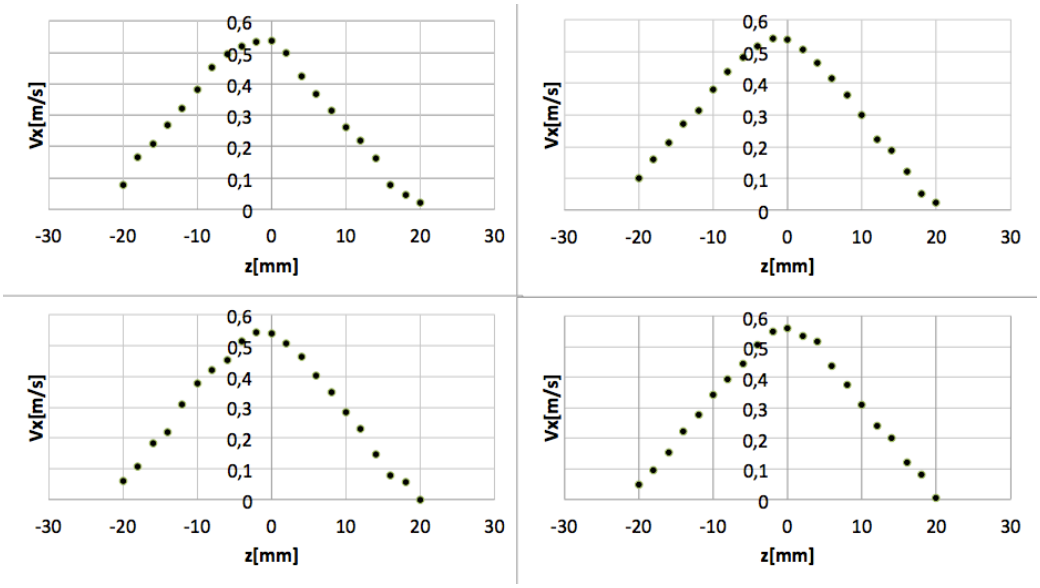

Graph. 4.12 Jet-2, Jet-1, Jet1 and Jet2 Vx profile at 5d

The flow development along the z axis suggests that there is no much difference between one jet development to the other and that is true particularly for Jet -2 and Jet 2. It is important to notice that no asymmetric Coanda effect breaks the symmetry and additionally the side walls do not affect the flow so much with the same effect and then that the geometry replicates well an infinite jet array configuration. The doubts of a slight greater Coanda effect on the top wall remains looking at the maxima of the profile represented in Fig. (4.12) which are all shifted to the negative side of the graph. However, it has to be remembered another time that its axis is x^t and so it has to be shifted on the right by 0.76 mm. This means that, if this asymmetric effect exists, it should be very slight and it should act in the same direction for all the jets. These results let us to study a quarter of the whole domain.
In order to show a qualitative and overall view of the average velocity flow map, some stream-wise velocity profiles at different diameters from the inlet are shown in Graph. (4.13-16). It is possible to see the absence of big deflection which shift velocity peaks.

Re	D	$angle\ between\ x\ and\ x^t$	$axis\ used\ for\ graphs$
10000	1	0.52°	x

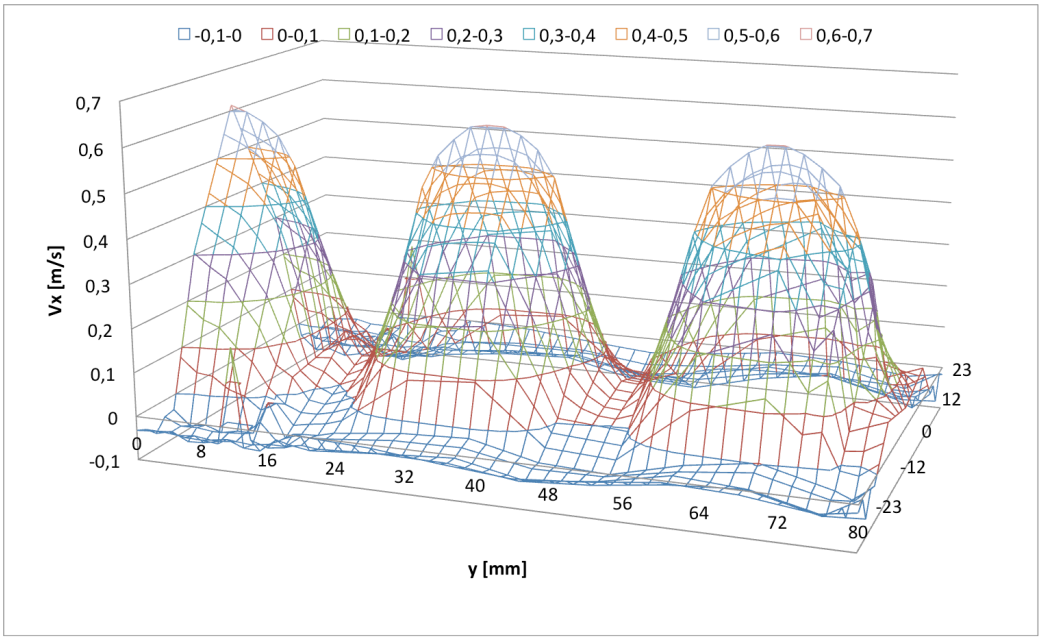

Graph. 4.13 Vx profile at 1D

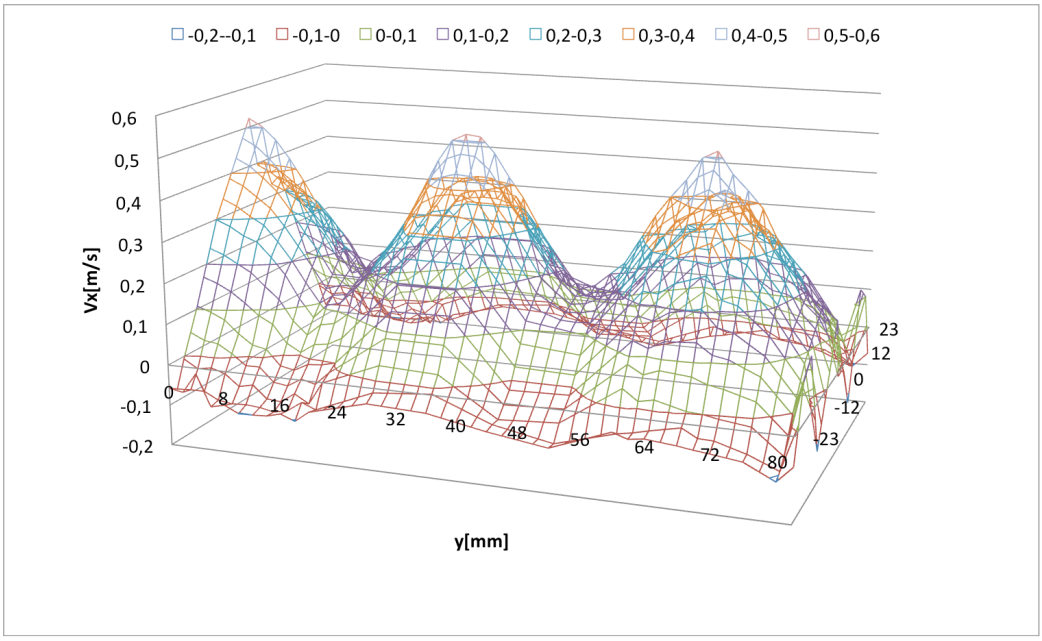

Graph. 4.14 Vx profile at 4D

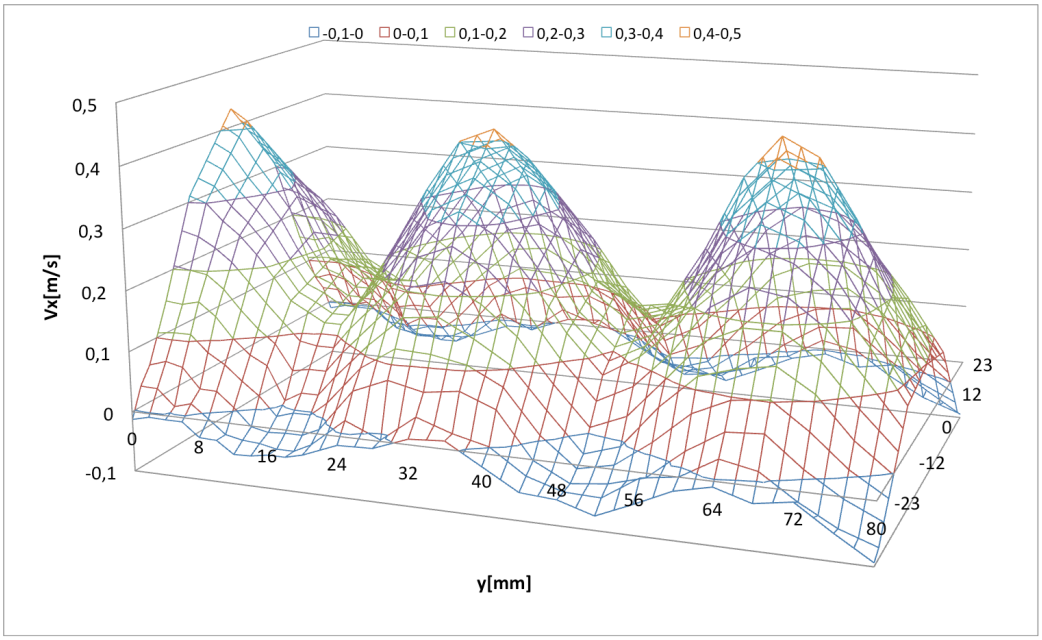

Graph. 4.15 Vx profile at 5D

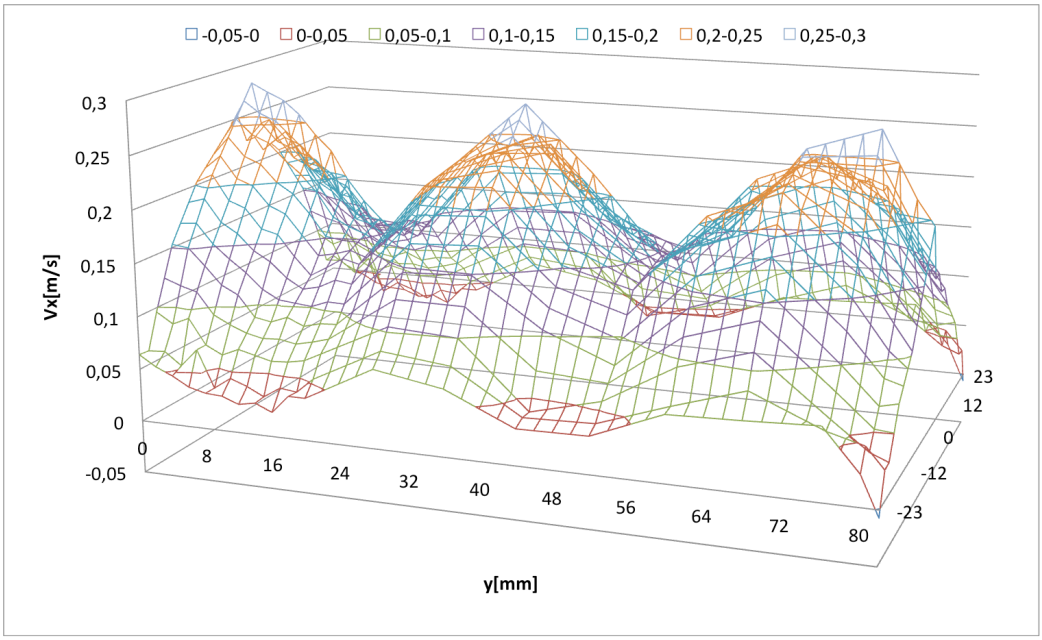

Graph. 4.16 Vx at 7D

Observing the legends of the 3D graphs it could be noticed the presence of recirculation, which, near the inlet, extends along the whole upper surface. Increasing the distance from the efflux, the recirculation disappears over and under the jets just from $x = 4a = 84\,mm$. The recirculation between the jets on the upper and on the lower surface remains till $x = 5a$ and in the corner of the plenum till $x = 7a = 147\,mm$. The Graph. (4.13-18) confirm qualitatively what shown analytically in Tab. (4.1) and Tab. (4.2). Additionally, if Coanda effect is present, it is so slight that is difficult to detect its presence.

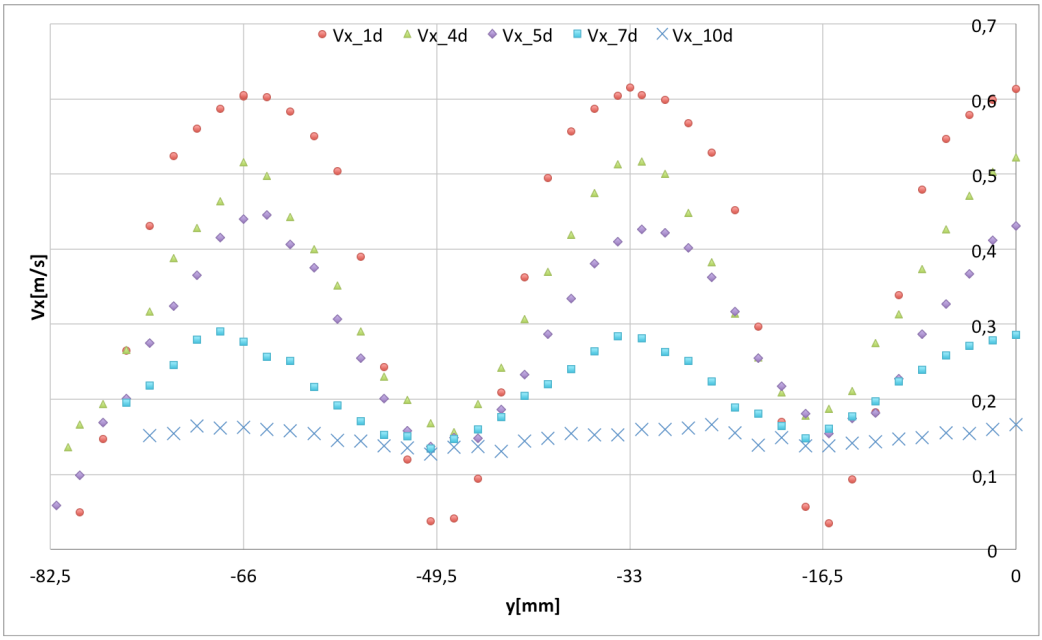

Graph. 4.17 Vx profile evolution Yminus_Z0

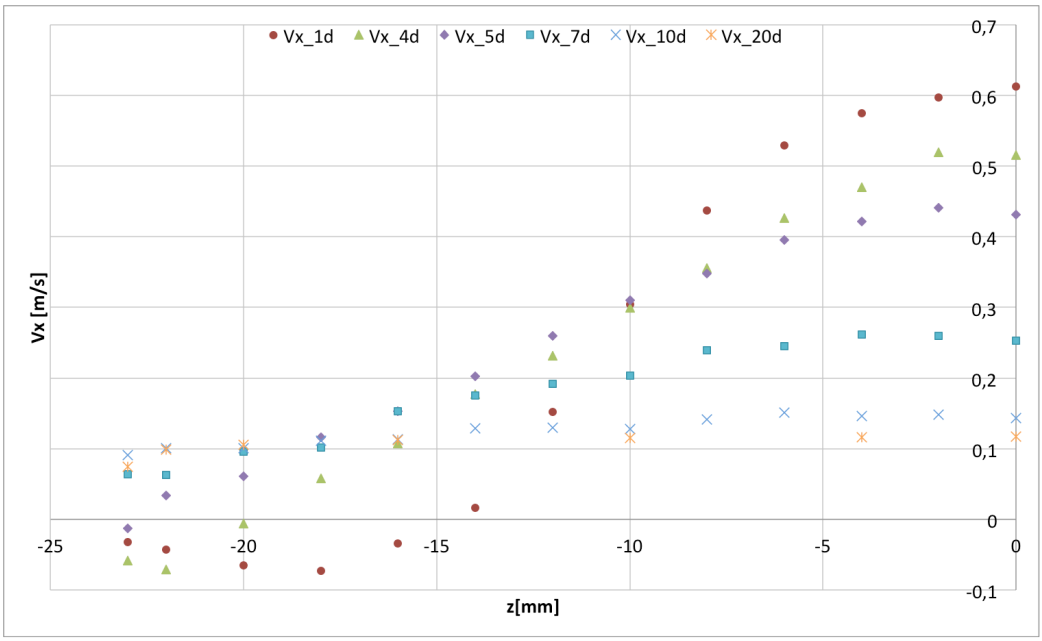

Graph. 4.18 Vx profile evolution Y0_minus

4.4.OSCILLATIONS

In order to verify the presence of "flapping", unsteady periodical solutions characterized by a peak on a certain frequency in the turbulence spectrum, a spectral analysis is performed using BSA Flow software's Advanced Spectrum task. From Nyqist theorem it is known that the sampling frequency has to double the frequency that has to be recognized by the FFT. Unfortunately the normal FFT transform needs data equi-spaced in time. This is not the case due to the random passage of the particles in the focal point and therefore the sampling frequency has to be higher. The system shows some problems to maintain the data rate higher enough due to several sedimentation zones for the glass particles along the circuit. The analysis is performed only in two points. One between the jets at a distance from the inlet of $x = 84\,mm = 4a$ and the other at $x = 147\,mm = 7a$. The literature has shown that in the case in which flapping happens, its frequency is around ${}^{V}/_{a} = {}^{m}/_{s}/_{m} = Hz$.
The bulk velocity inside the pipe could be use and so a frequency around $f \cong 25\,Hz$ is expected. The results are reported here.

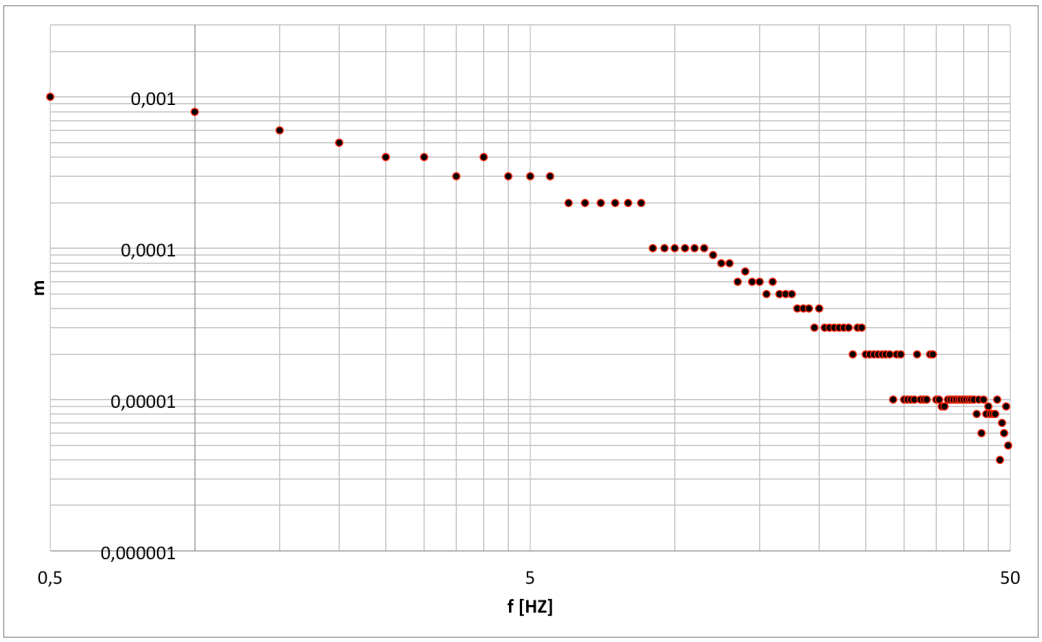

Graph. 4.19 Turbulence spectrum X84_Y10.5_Z0

$x\,[mm]$	$y[mm]$	$z[mm]$	$\#\,particles$	$\#/s$	V_x	RMS_x
84	−10.5	0	127533	195	0.264	0.107

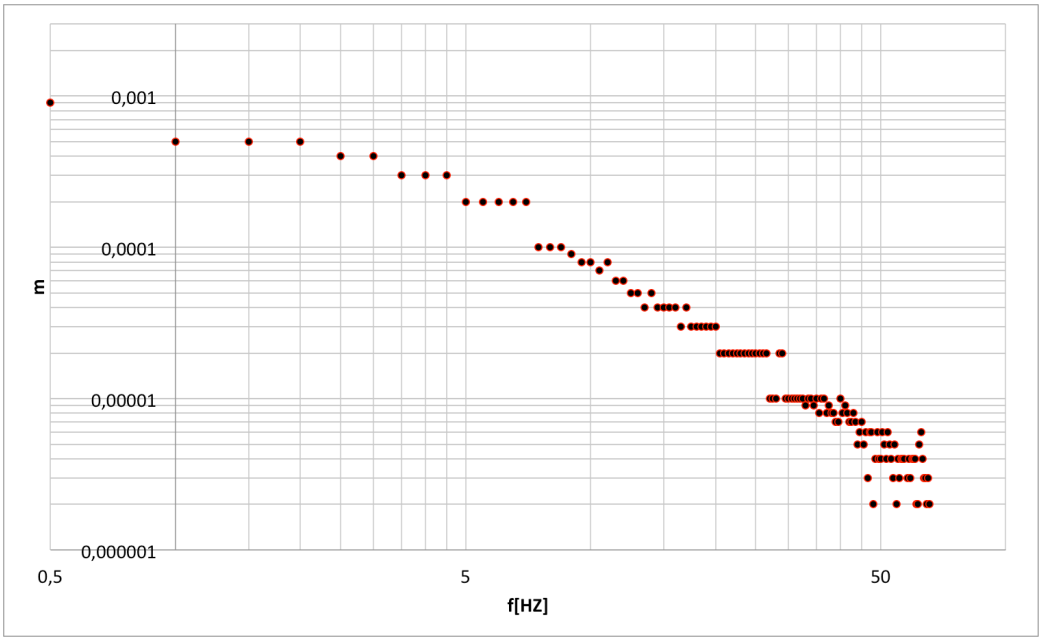

Graph. 4.20 Turbulence spectrum X147_Y0_Z0

$x\ [mm]$	$y\ [mm]$	$z\ [mm]$	$\#\ particles$	$\#/s$	V_x	RMS_x
147	0	0	127476	173	0.278	0.093

Both Graph. (4.19) and Graph. (4.20) do not show any peak, at least at frequency lower than 50 Hz.

4.5. EXPERIMENTAL VS. NUMERICAL

The experimental campaign has been conducted during four months in which a variation of the mass flow has been detected. In order to compare this data and the data of the simulations, an adimensionalization respect the bulk velocity could be very useful. Additionally, the axis are represented with positive values. The models used are

- $k-\omega\ SST$ (kw_sst)
- $k-\varepsilon\ RNG$ (ke_RNG)
- V^2f (v2f)
- $k-\varepsilon\ Low\ Reynolds\ Lam-Bremhorst$ (ke_LowRe)
- $k-\varepsilon\ Low\ Reynolds\ Launder-Sharma$ (ke_LowRe_2)

- $k-\varepsilon$ *Realizable* (Rea)
- *Non − Linear model performed by Politecnico di Milano* (NLEV)
- *Reynolds Stress Model* (RSM)
- *Large eddy simulation* (Les)

Graph. (4.21) representing V_x on X21_Yall_Z0 permits to validate the efflux profile for each model

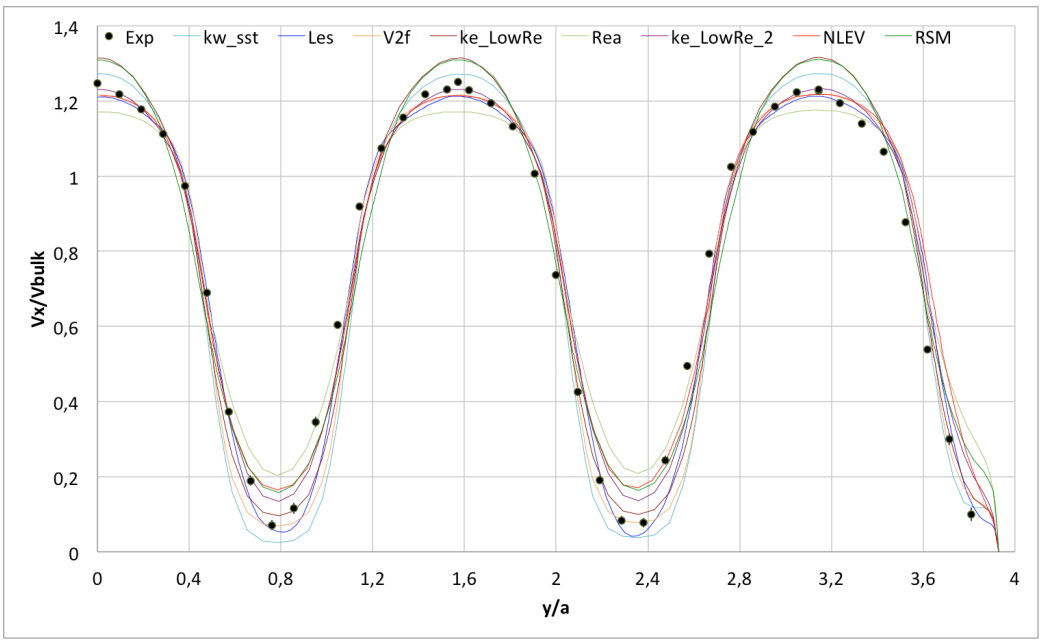

Graph. 4.21 Efflux profiles

RSM and $k-\varepsilon$ *Low Reynolds Launder − Sharma* overstimating the velocity peaks and $k-\varepsilon$ *Realizable* understimates it. The other models replicate very well the profile. Globally all the methods maintain the deviation respect to the experimental data lower than 7% of peak velocity.
It is presented a global view of simulation results for some values of interest and they are compared with experimental results and with the results of empiric laws presented in the first chapter (Tab. (4.5)).

	x_s/a	x_c/a	x_r/a
Experimental	*0,714*	*16*	5
Tanaka(7) Eq(1.23)	*5,717*	-	-
Durve (33) Eq(1.27-1.28)	*9,103*	*9,9*	-
Miozzi(24) Eq(1.16)	-	-	*5,5*
kw_sst	*0,661*	*16*	*6,8*
Rea	*0,039*	*11*	*6,6*
Damp W	*0*	*10*	*6,4*
ke_LowRe	*0,007*	*11*	*5,5*
ke_LowRe_2	*0,027*	*11*	*5,2*
RSM	*0*	*18*	*4,8*
V2f	*0,038*	*17*	*7,6*
Les	*0,579*	*16*	5,7

Tab. 4.5 Global view

The position of the stagnation point is revealed to be very close to the inlet. The reason lies in the value of $D_0/a = 1.5714$. This very low value represents the high linear density of jets, which push the recirculation against the inlet wall. This is the reason why some models do not detect recirculation at all. As in Tab. (4.5) $k-\omega\, SST$ and Les have the best prediction of stagnation point. Concerning the combination point it is important to premise the convention used to determine it. It is chosen to associate it to the value of x/a at which the spreading ratio reaches the asymptotic value of 0. As we can see in Tab. (4.5) $k-\omega\, SST, RSM, V^2f$ and Les perform very well. The others drastically anticipated this point.

Another important variable to consider is the reattachment point. Unfortunately the experimental measurements of this position are difficult to be captured. The adopted strategy to locate it consists in taking the measure of the inversion point, the one at which the recirculation ends, for Xall_Y0_Z22 and Xall_Y16,5_Z22 lines.

The reattachment point lies in the vicinity of the inversion point near the walls.

Globally, except for V^2f and $k-\omega\, SST$ which have the inversion point too downstream, all the models predict it with the same accuracy. The laws of Durve and Tanaka, fail completely the points prediction. This is an important results because shows that although the parameters with which jets phenomena

could be described are the same for every jets system, the values are very different and hardly predictable.
It is very interesting the prediction of eq.(1.16) for x_r which confirms the hypothesis of which it seems not to depend on Re_D.
It is important to notice that the position of reattachment point is not the same moving along Y (Graph. (4.22)).

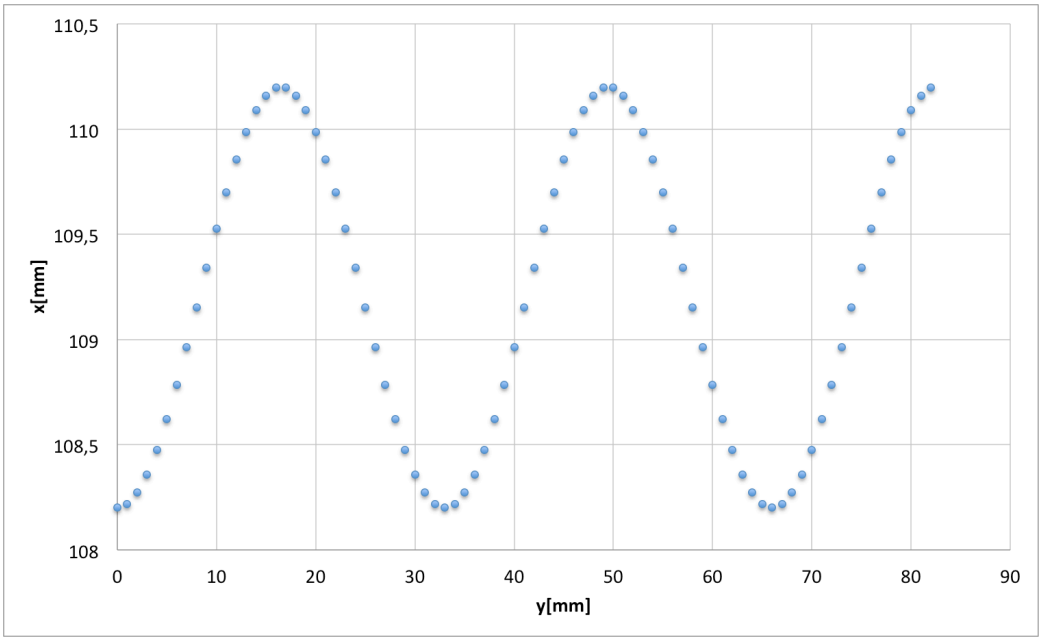

Graph. 4.22 Sinusoidal interpolation of experimental data for reattachment point

The reattachment point on the line between jets is surely downstream respect the reattachment point on the centerline.

The models which predict the core length longer present an inversion point shifted downstream due to the stronger recirculation. This is obviously necessary for the continuity equation. It is evident for $V^2 f$ as rapresented in Figure (4.2).

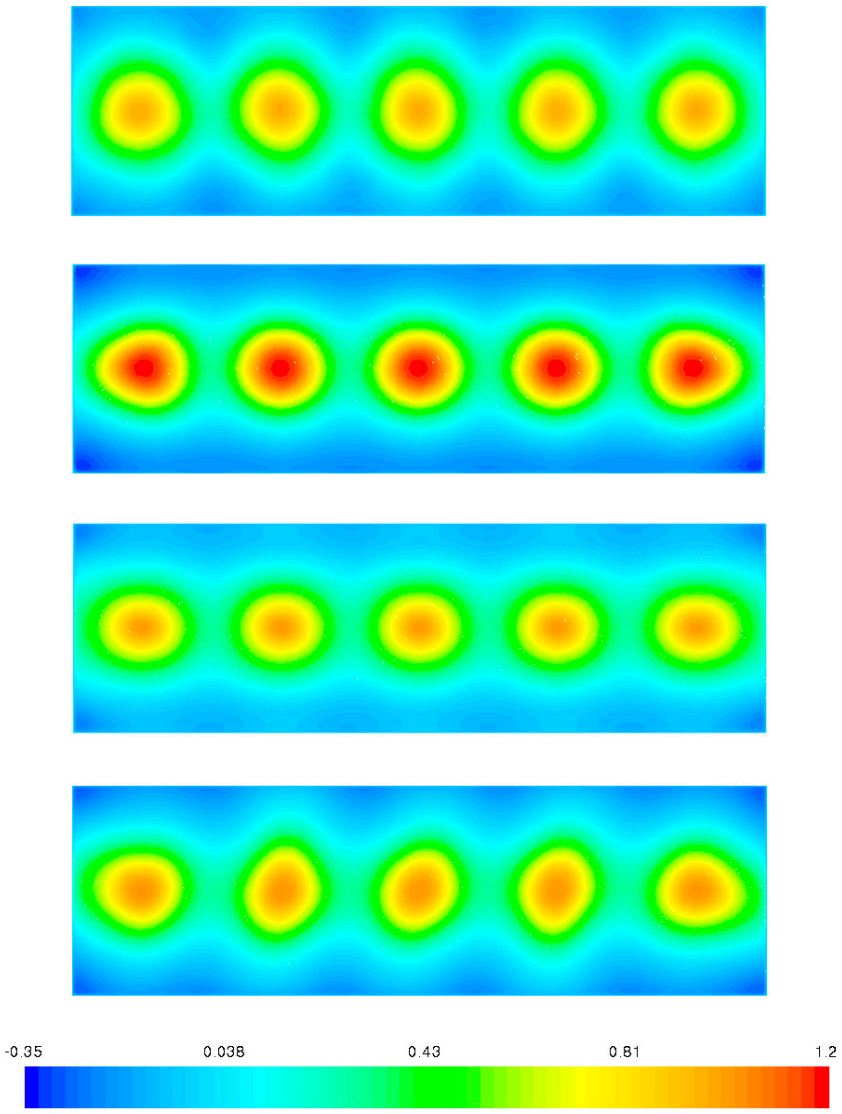

Figure 4.2 Vx contour at 4D for Les, v2f, RSM and NLEV

Concerning the decay the following regression is performed by Matlab tool (Graph. (4.23)). The functions analyzed are the eq.(1.2), the eq.(1.13) and the eq.(1.22).

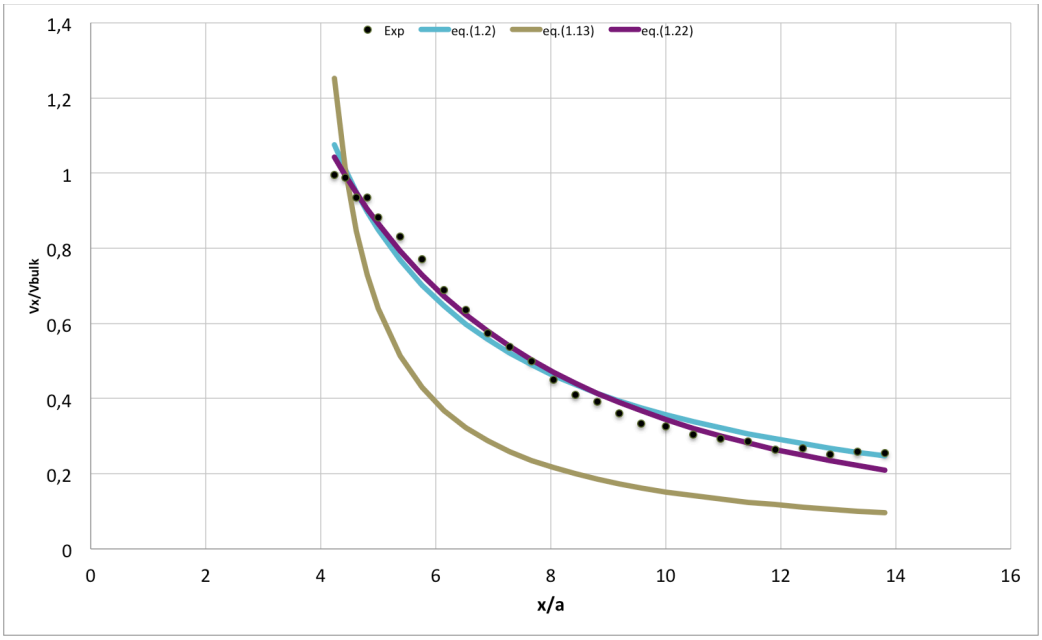

Graph. 4.23 Model fitting

The values carried out are the following:

	K	x_0/a	c
Eq.(1.2)	3.082	1,374	1
Eq.(1.13)	0.9956	3.443	1/2
Eq.(1.22)	68.42	-3.676	2.023

Tab. 4.6 Coefficient of fitting equation

Although the fitting of eq.(1.22) is very good the confidence interval reveals that this solution is very unstable and so it is not a good fitting. The fitting of eq.(13) is stable but as represented in Graph. (4.23) do not agree well with experimental data. The eq. (1.2) is still the best fitting curve.
The most synthetic parameter to evaluate if the models are predicting "well" or not the flow are the center line velocity in the stream-wise direction (Xall, Y0, Z0) and the spreading ratio (eq.(1.30)).

The experimental data show that the potential core preserves itself till $x = 42\,mm = 2a$ and the velocity becomes fully developed around $x = 325\,mm > 15a$ (Graph. (4.24)).

The spreading ratio presents two zones of interest (Graph. (4.25)). The first one is near the inlet in which its value is greater than one. This reveals a presence of a recirculation between the jets. This recirculation vanishes very quickly, because at $x = 18\,mm < a$ the value of SR is already lower than one. The second zone of interest is the last one, in which the value of SR is negative.
This fact reveals the presence of deflection. In the present case, the value is negative, but not so distant from zero. This means that the deflection is very slight as just said above. All the numerical methods shows physical, steady and symmetrical results, except for $k-\varepsilon\,RNG$ which has not reached the convergence.

The model $k-\varepsilon\,Low\,Reynolds\,Lam-Bremhorst$ predicts better than the other the potential core. Although V^2f model predicts well the first part of the core, the end is not characterized by a steep gradient and so the stream-wise velocity deviates from the experimental data, overestimating it. It can be noticed the same behavior of V^2f in $k-\omega\,SST$ for which the merging zone starts too late. However, $k-\omega\,SST$ is the only model which predicts the recirculation at the very beginning of the domain, as represented in Graph. (4.25). RSM and $k-\varepsilon\,Low\,Reynolds\,Launder-Sharma$ generally overestimate the velocity at the efflux of the pipe, but the lenght of the potential core is globally correct.

Concerning the mixing zone, almost the totality of the models over-predicts the decay rate of the velocity, except for RSM and V^2f, for which the gradient is very similar to the experimental gradient.

Although close to the inlet and at the end of the domain the prediction is globally good, it is clear how RANS models suffer when the fluid dynamics becomes complex as in the merging zone (4D-9D). Large eddy simulation predicts well the very beginning of the flow, as represented with the spreading ratio greater than one. In general the center line velocity in core region is largely better predicted by the *Les* than by the other models. However this is not sufficient for a good replication of SR in the core region. The reason lies in a bad prediction of the stream-wise velocity profile on the line Xall_Y16,5_Z22. RSM behaves better in the mixing zone, because of the greater velocity gradient of *Les* simulation.

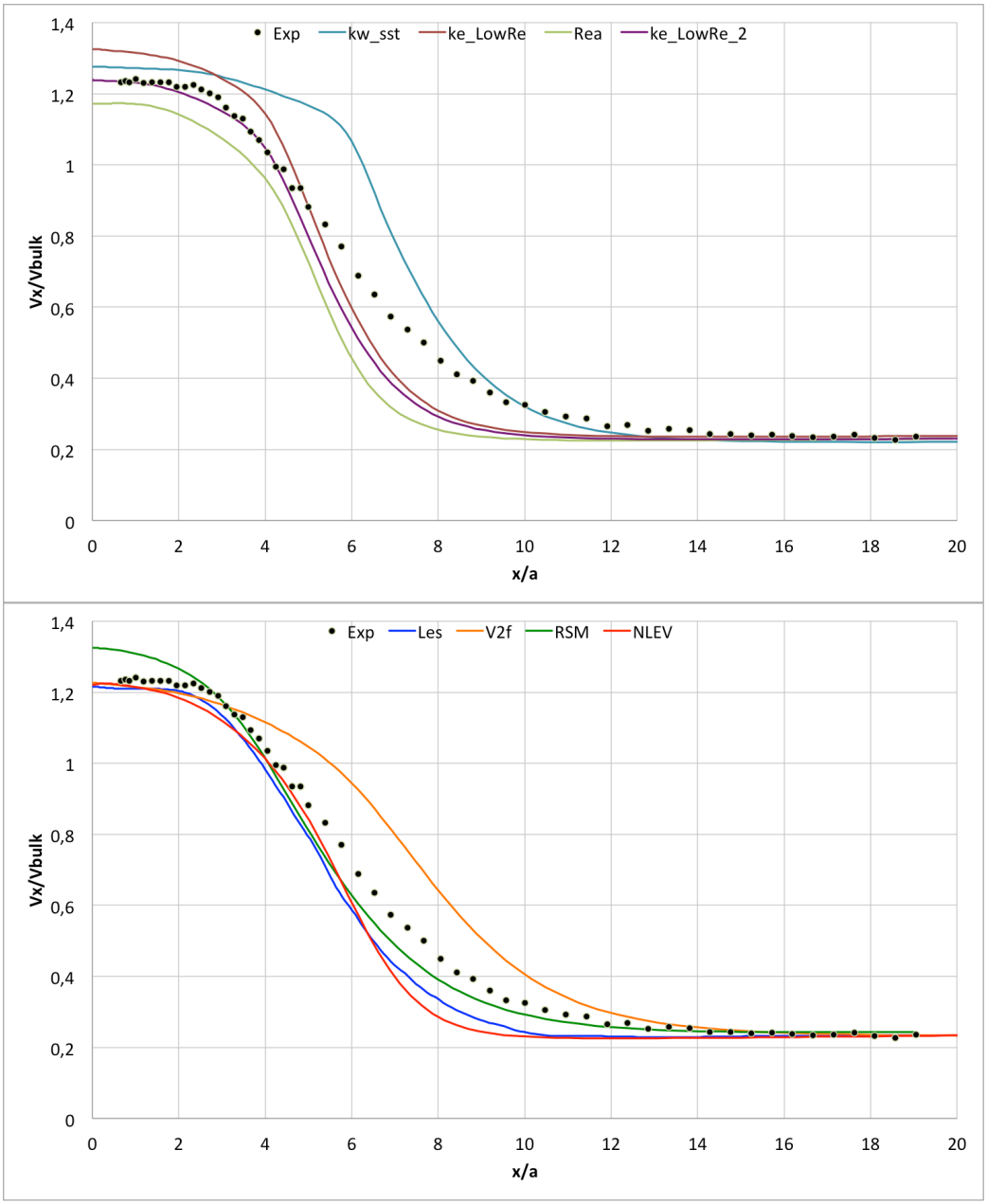

Graph. 4.24 Velocity Decay Vx Xall_Y0_Z0

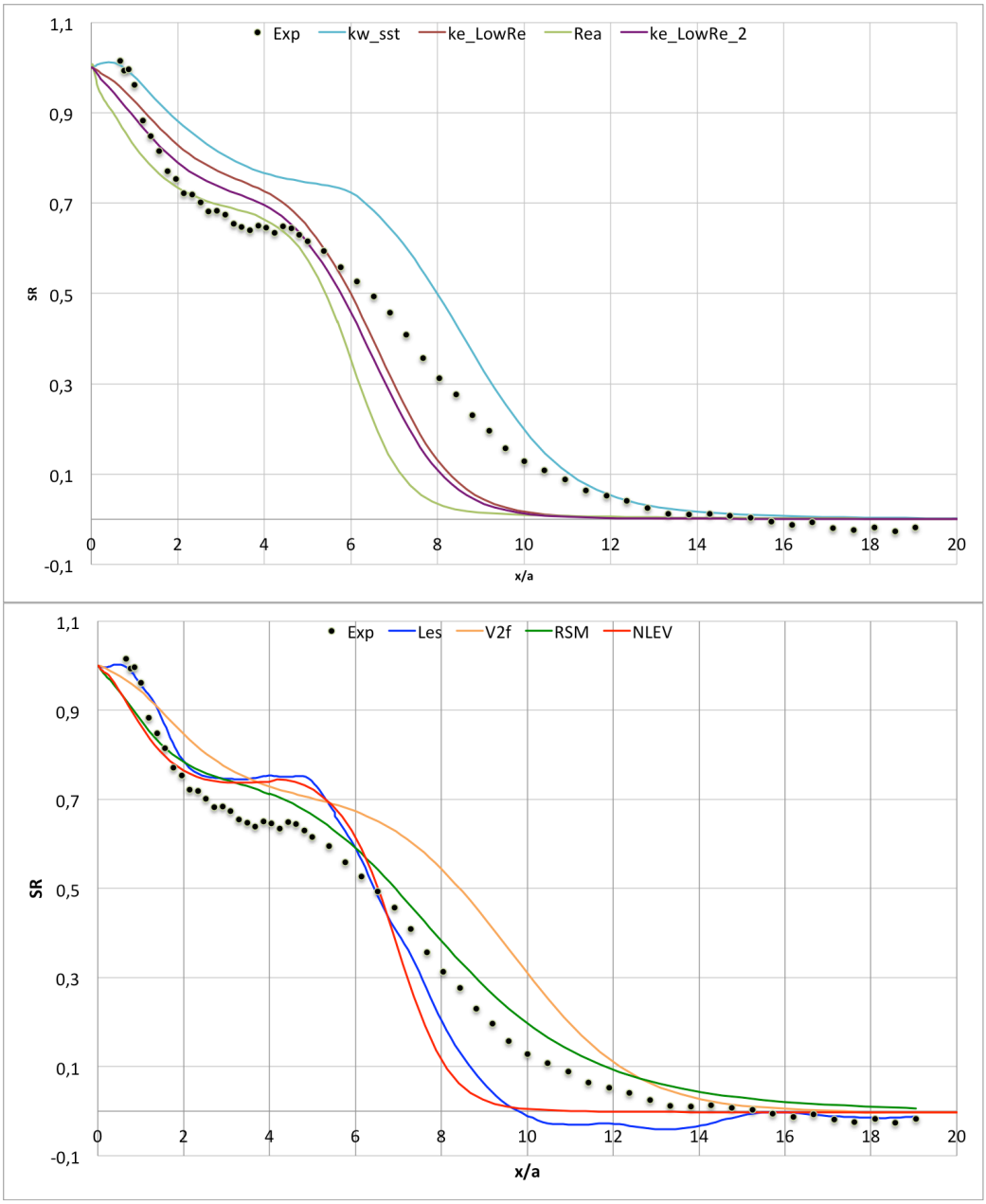

Graph. 4.25 SR

According to the fact that the jets develop in the same way, it has been chosen to compare experimental and numerical data only in the most significant lines and for the models predicting better the velocity decay and the spreading ratio. These models are:

- V^2f
- *NLEV*

- *RSM*
- *Les*

A quarter of domain is considered because of the symmetry of the flow.
Graph. (4.26-30) represents the line Yplus_Z0 and Graph.(4.31-35) represent the line Y0_Zplus.

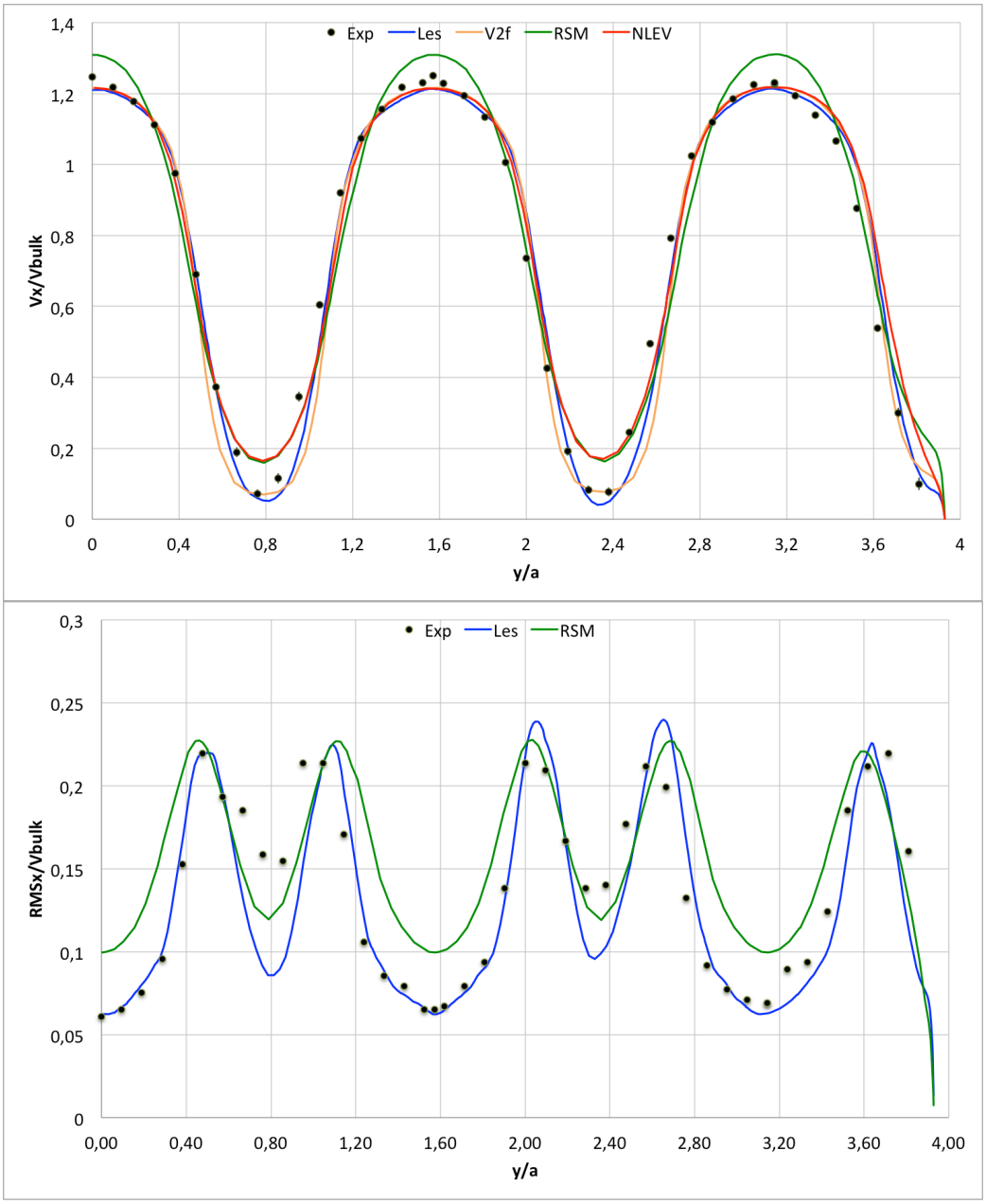

Graph. 4.26 Vx and RMSx X21_Yplus_Z0

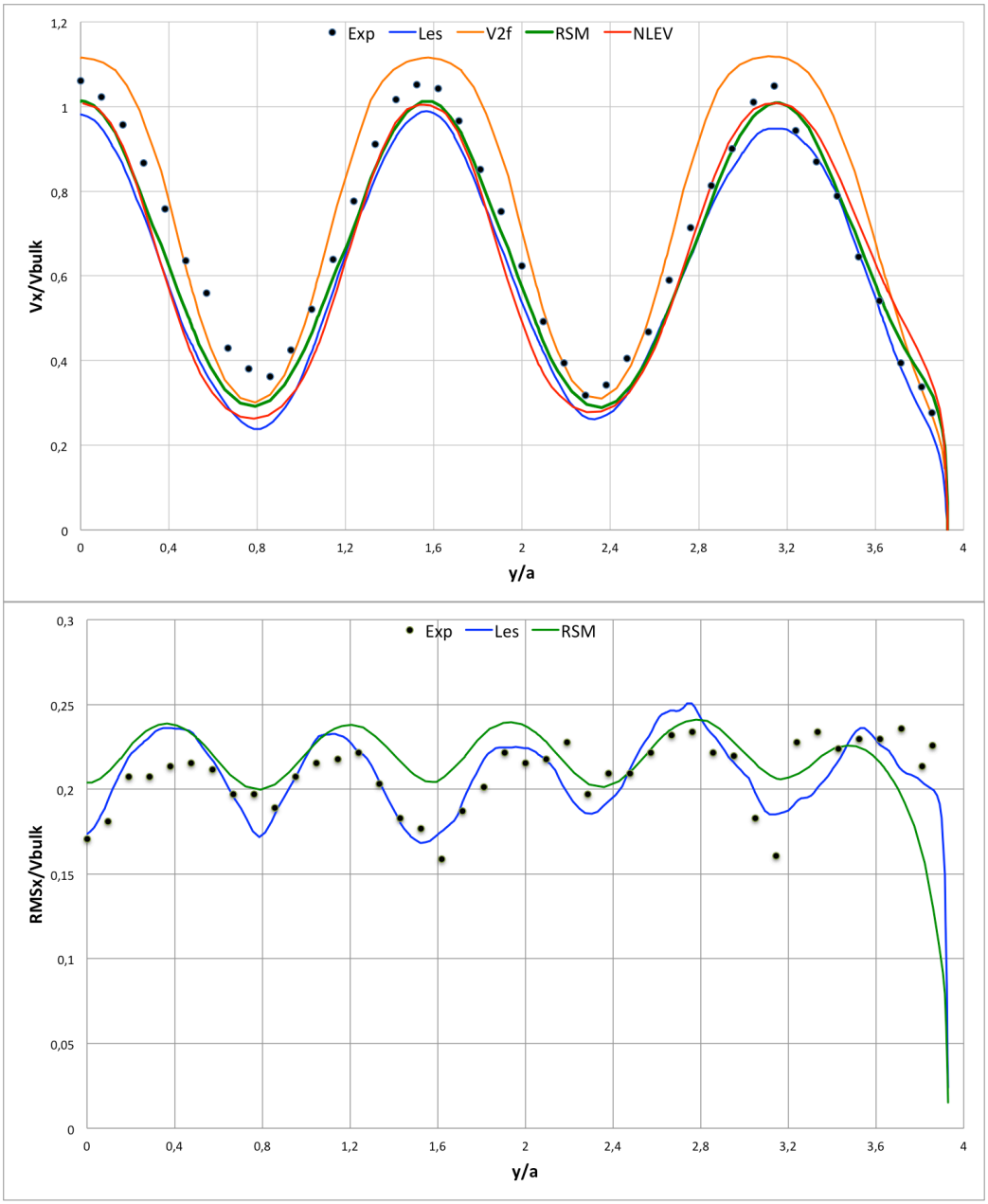

Graph. 4.27 Vx and RMSx X84_Yplus_Z0

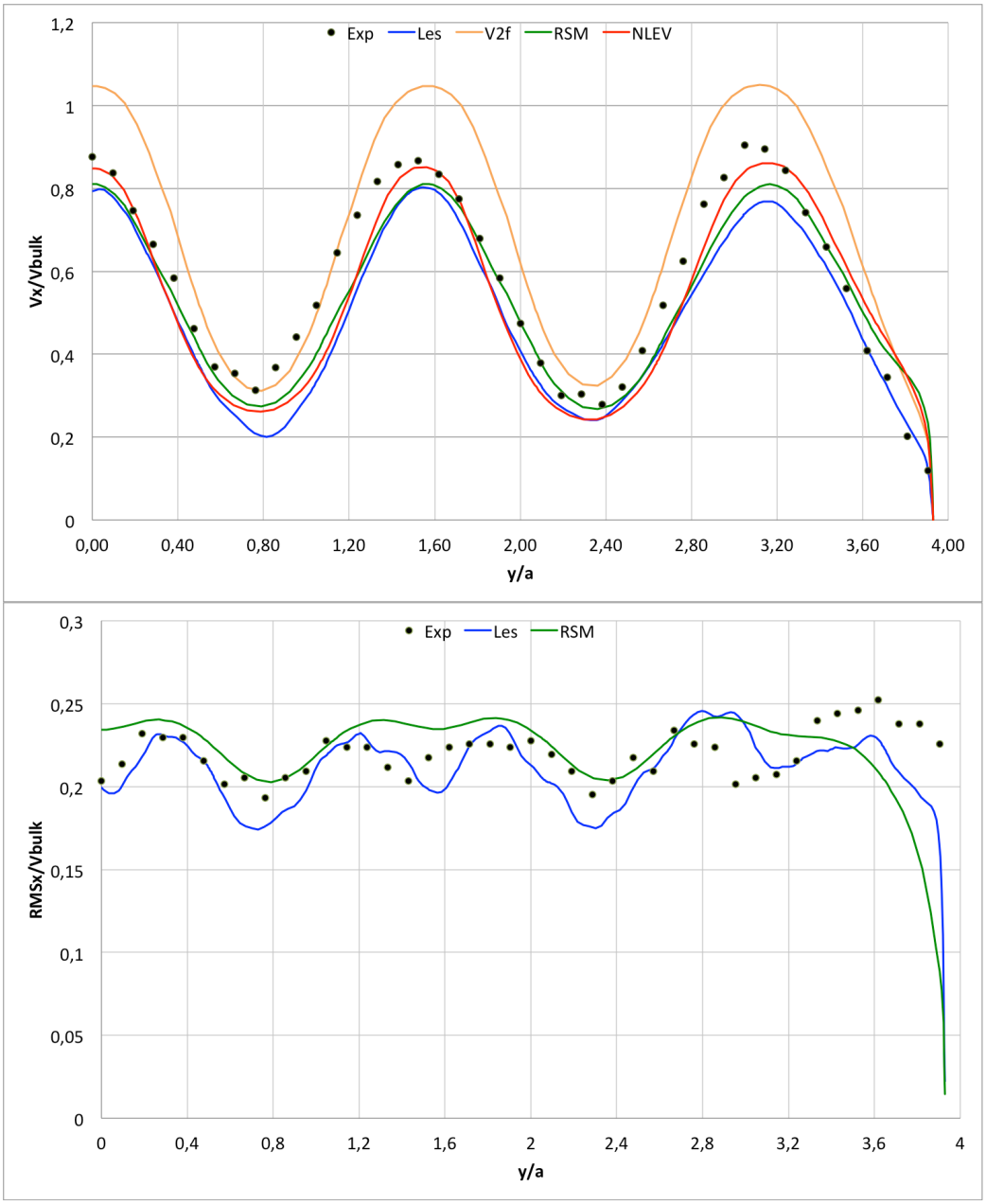

Graph. 4.28 VX and RMSx X105_Yplus_Z0

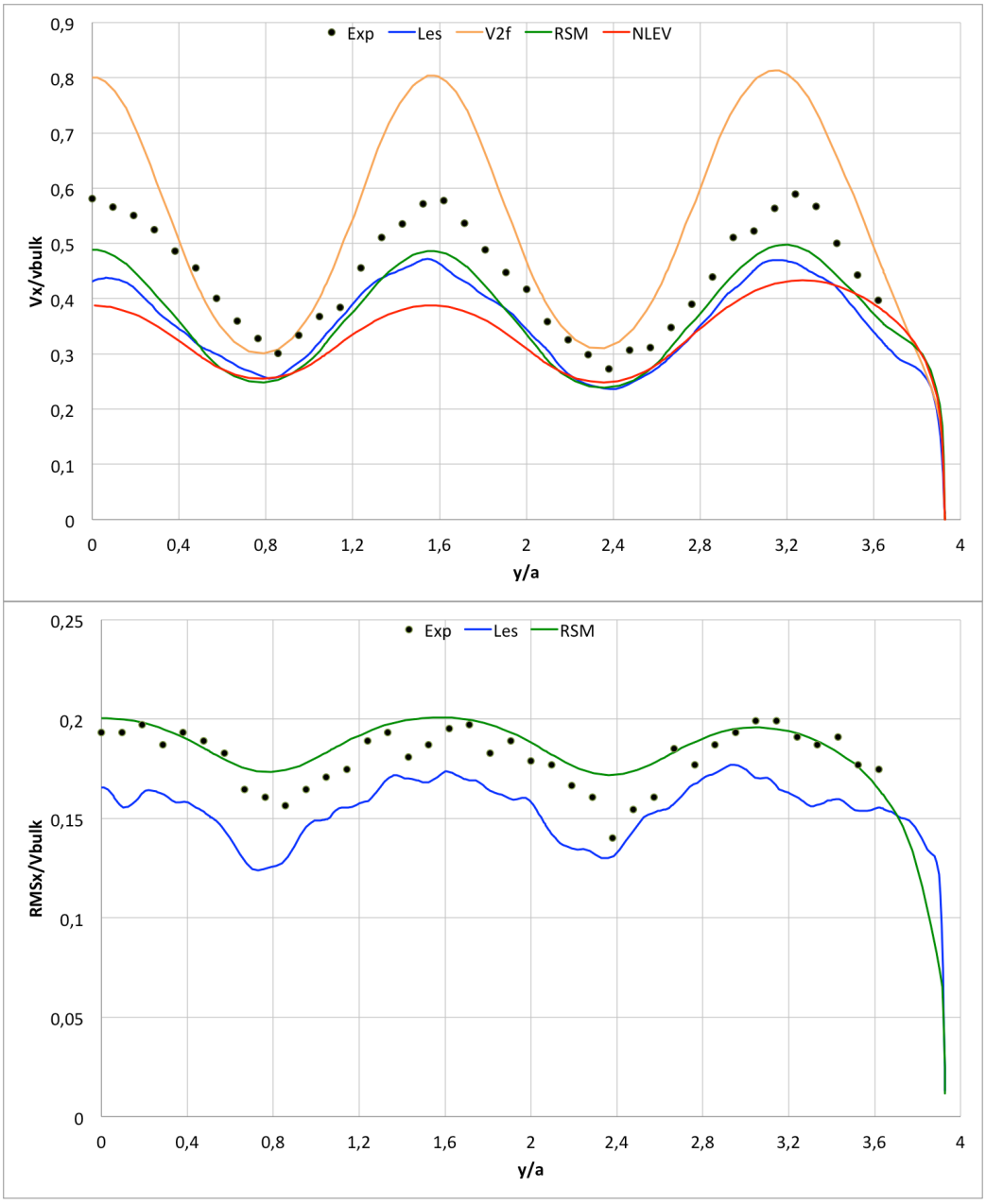

Graph. 4.29 Vx and RMSx X147_Yplus_Z0

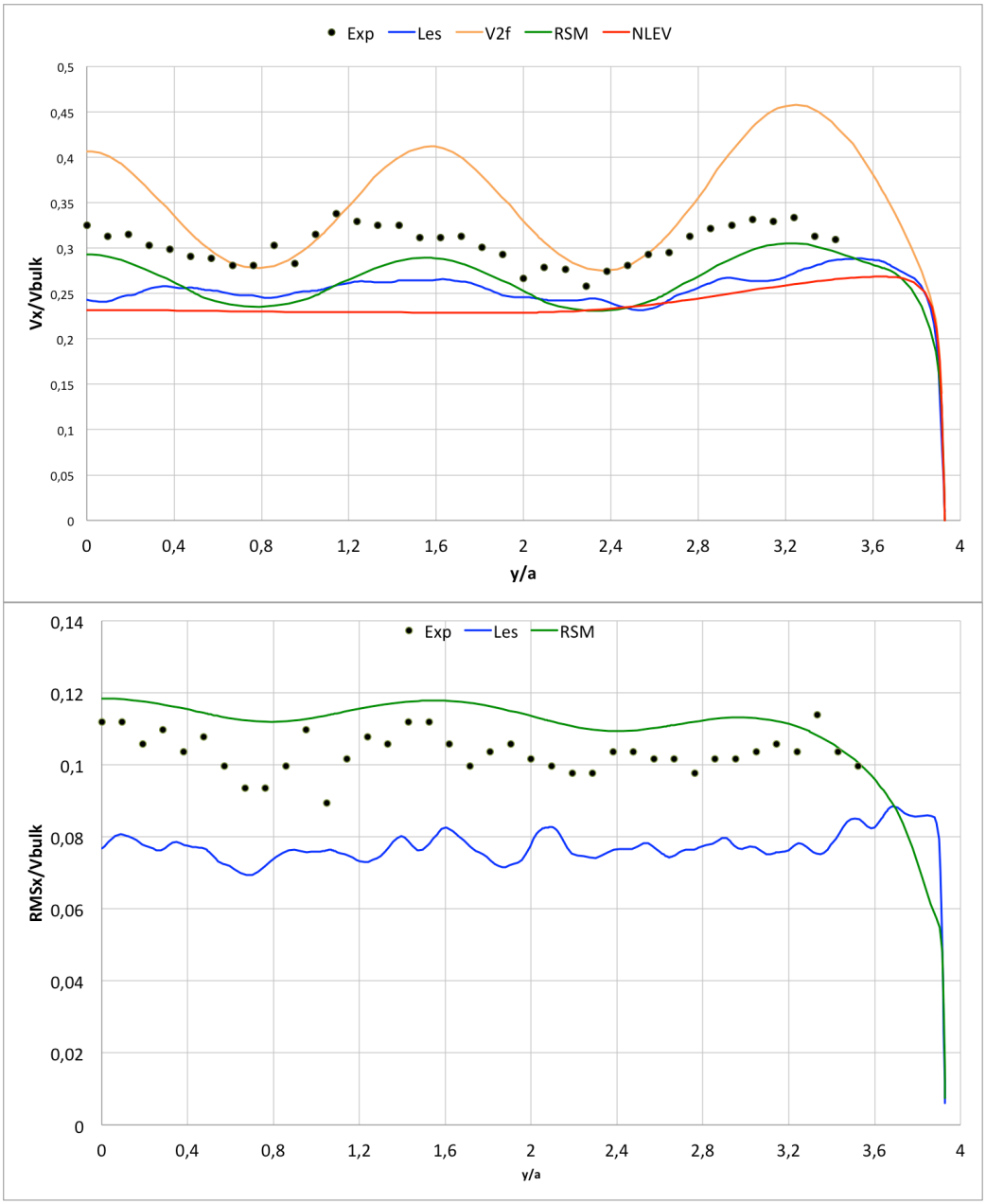

Graph. 4.30 Vx and RMSx X210_Yplus_Z0

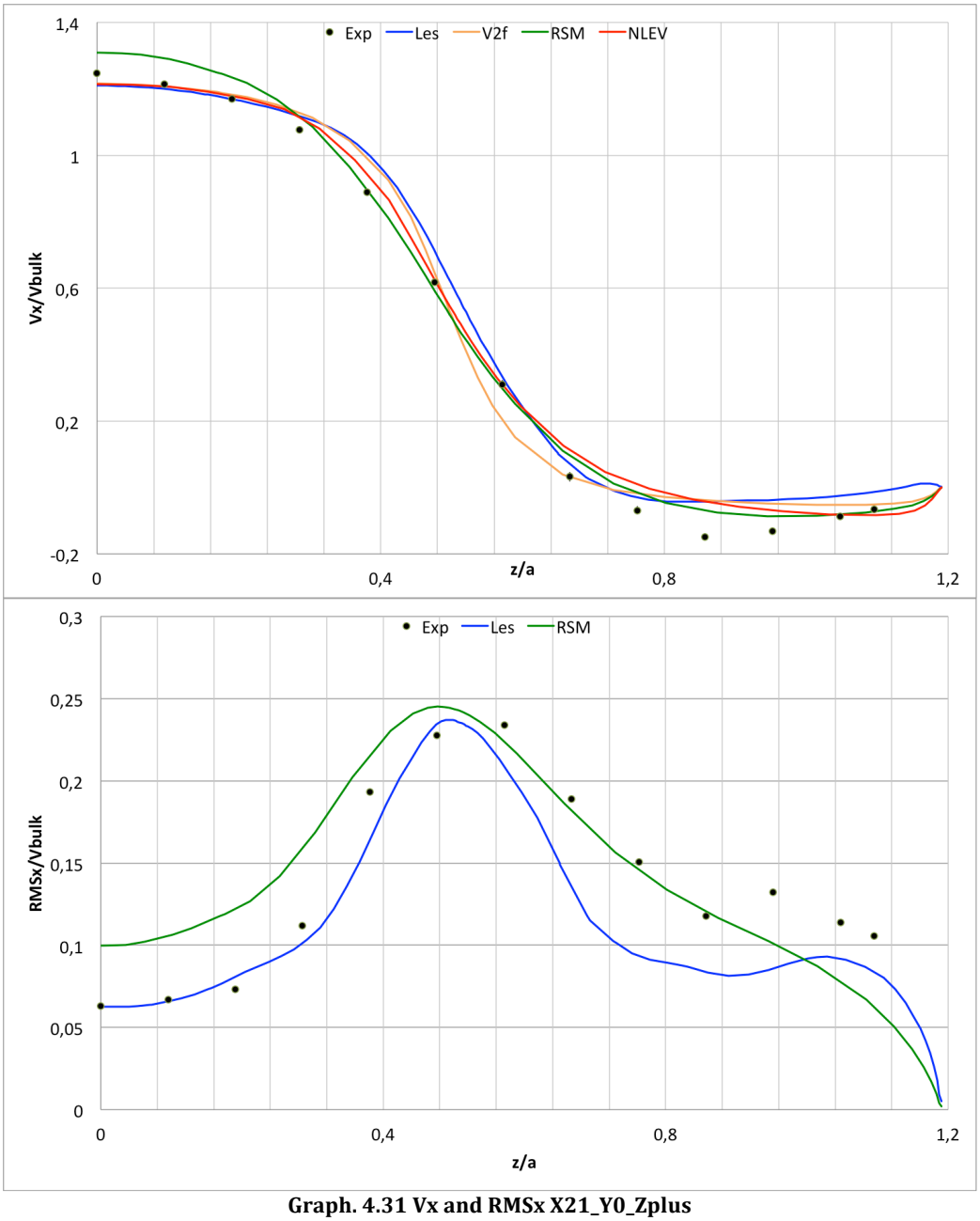

Graph. 4.31 Vx and RMSx X21_Y0_Zplus

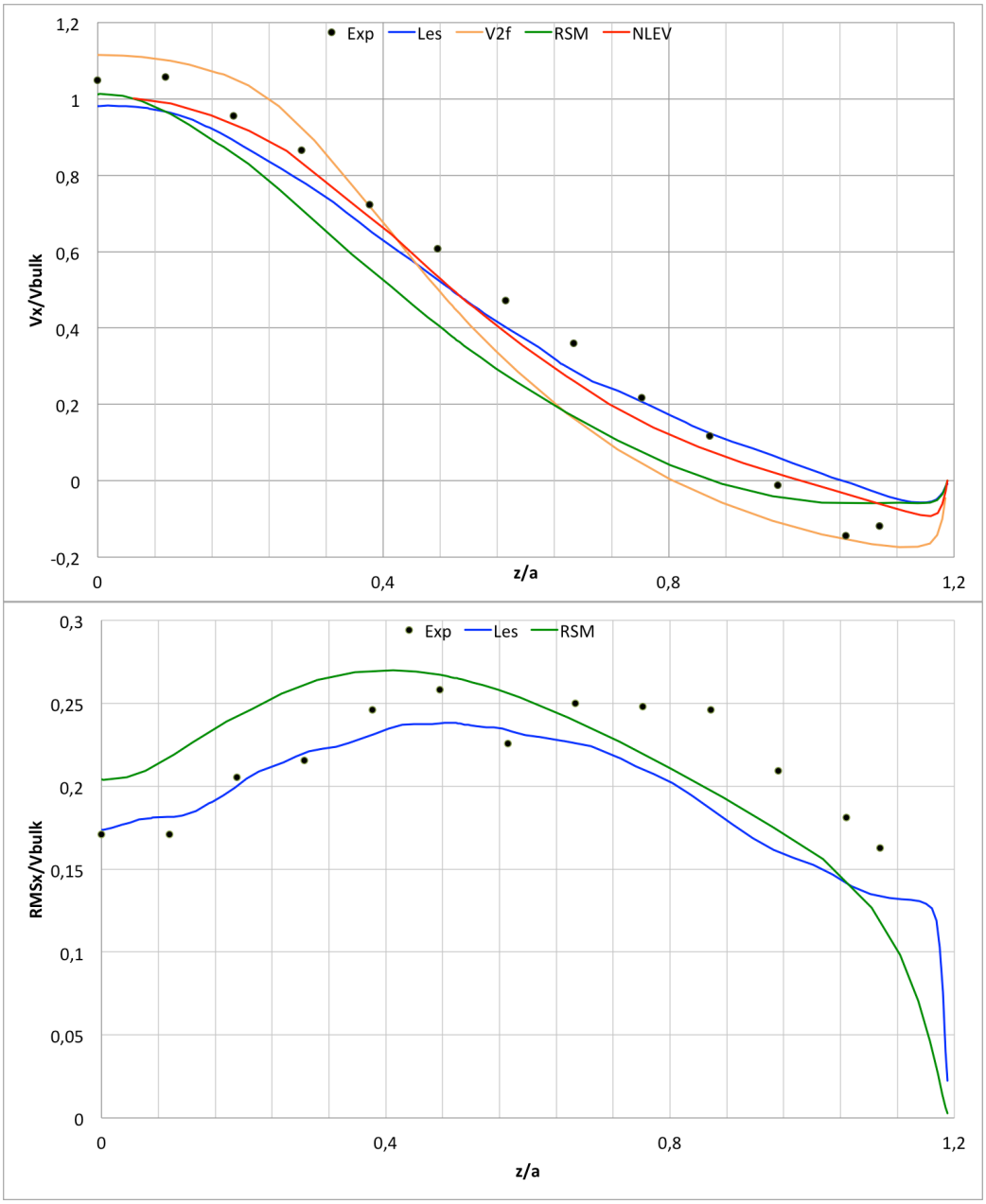

Graph. 4.32 Vx and RMSx X84_Y0_Zplus

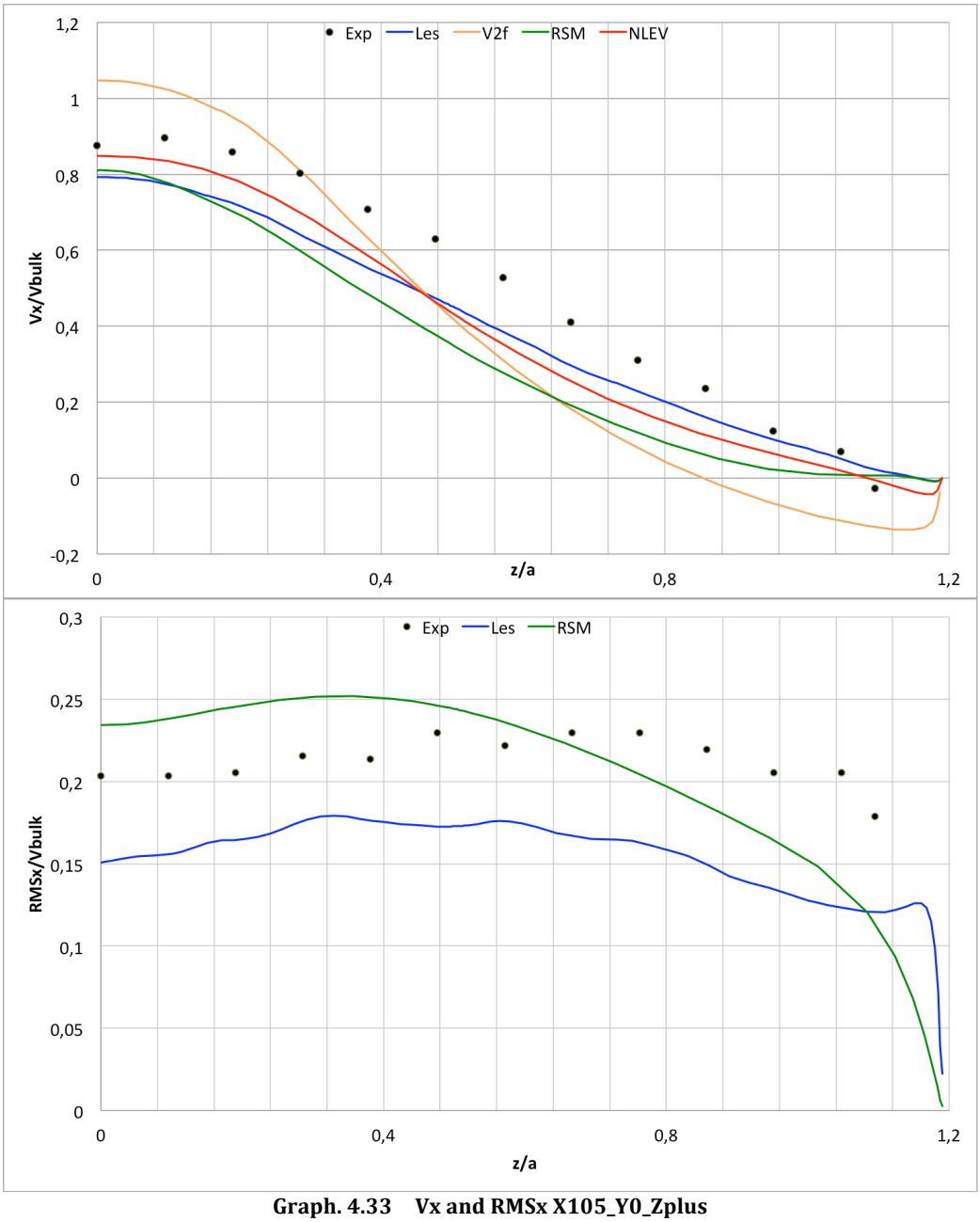

Graph. 4.33 Vx and RMSx X105_Y0_Zplus

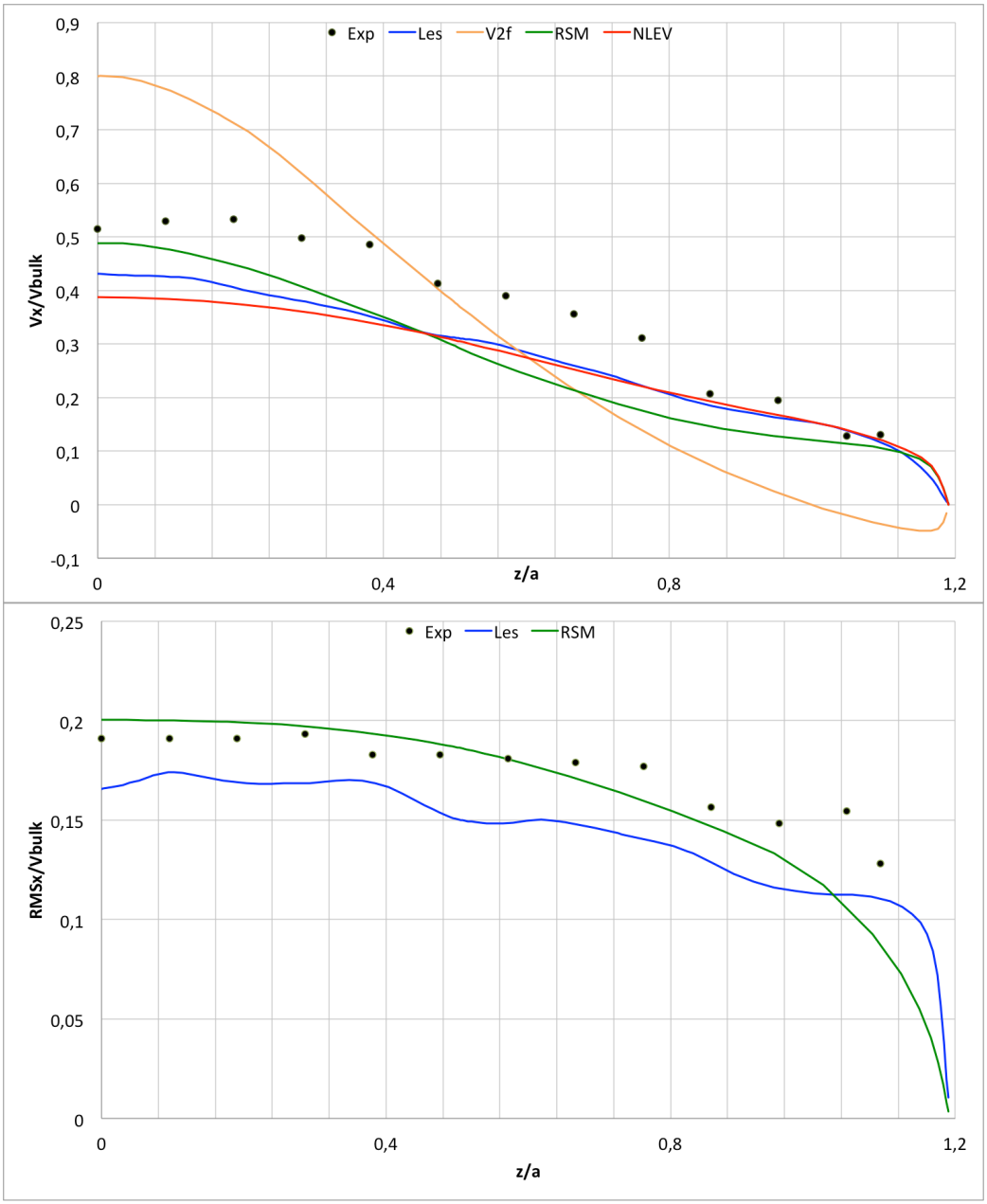

Graph. 4.34 Vx and RMSx X147_Y0_Zplus

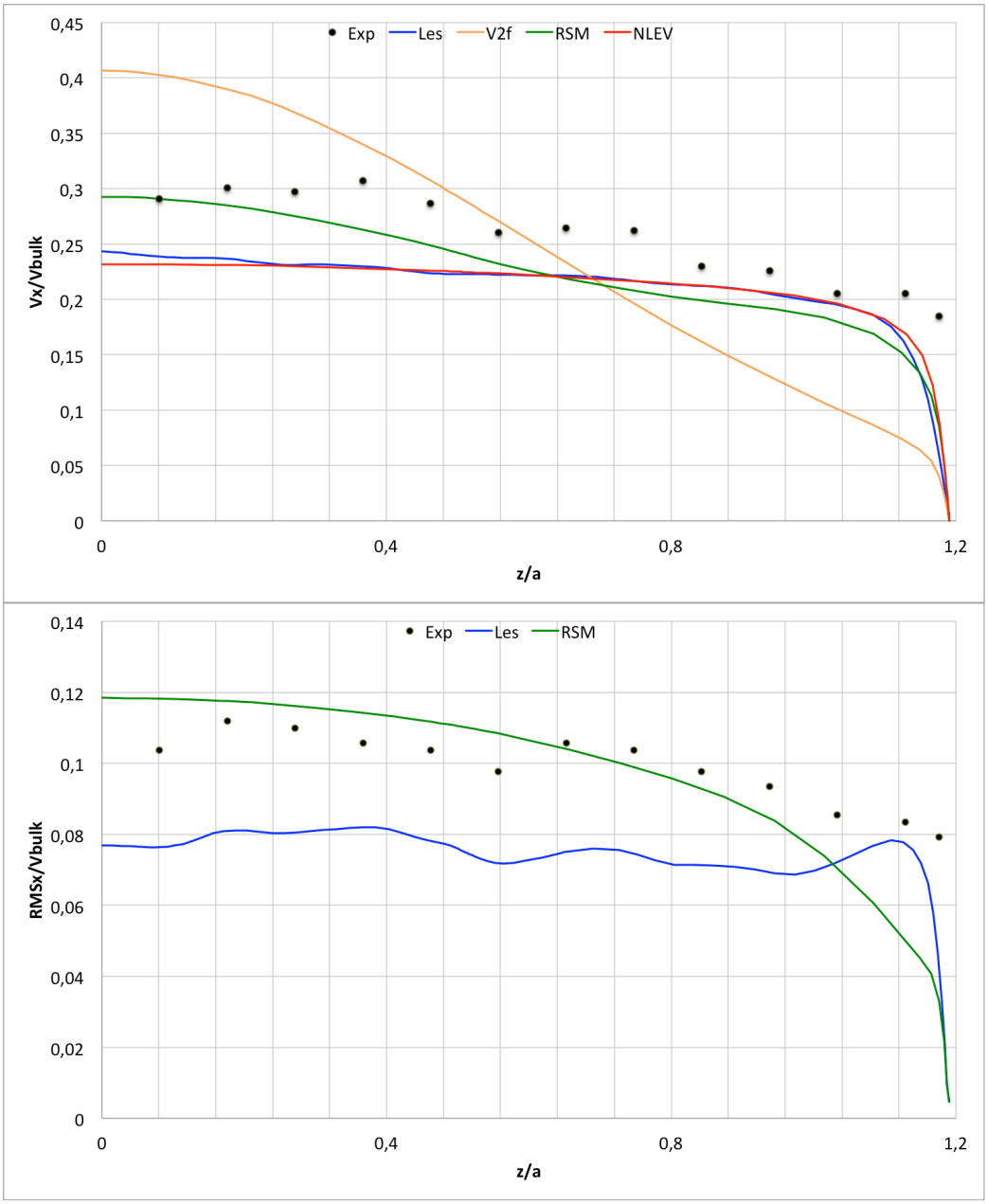

Graph. 4.35 Vx and RMSx X210_Y0_Zplus

As expected, V^2f shows a large deviation from experimental data because of the error on the prediction of potential core length and globally *RSM* and *LES* minimize the difference between experimental and numerical results.
All these models, which replicate well the velocity decay, have a good performance on the span-wise velocity which is indicative of the jet expansion and so of the diffusion.

V^2f model is able to correctly predict the span-wise velocity (y-direction) at 5D even if the profiles at 1D are not coherent with experimental data. This is confirmed by the right prediction of the velocity decay from 5D as can be observed in Graph. (4.36-37).

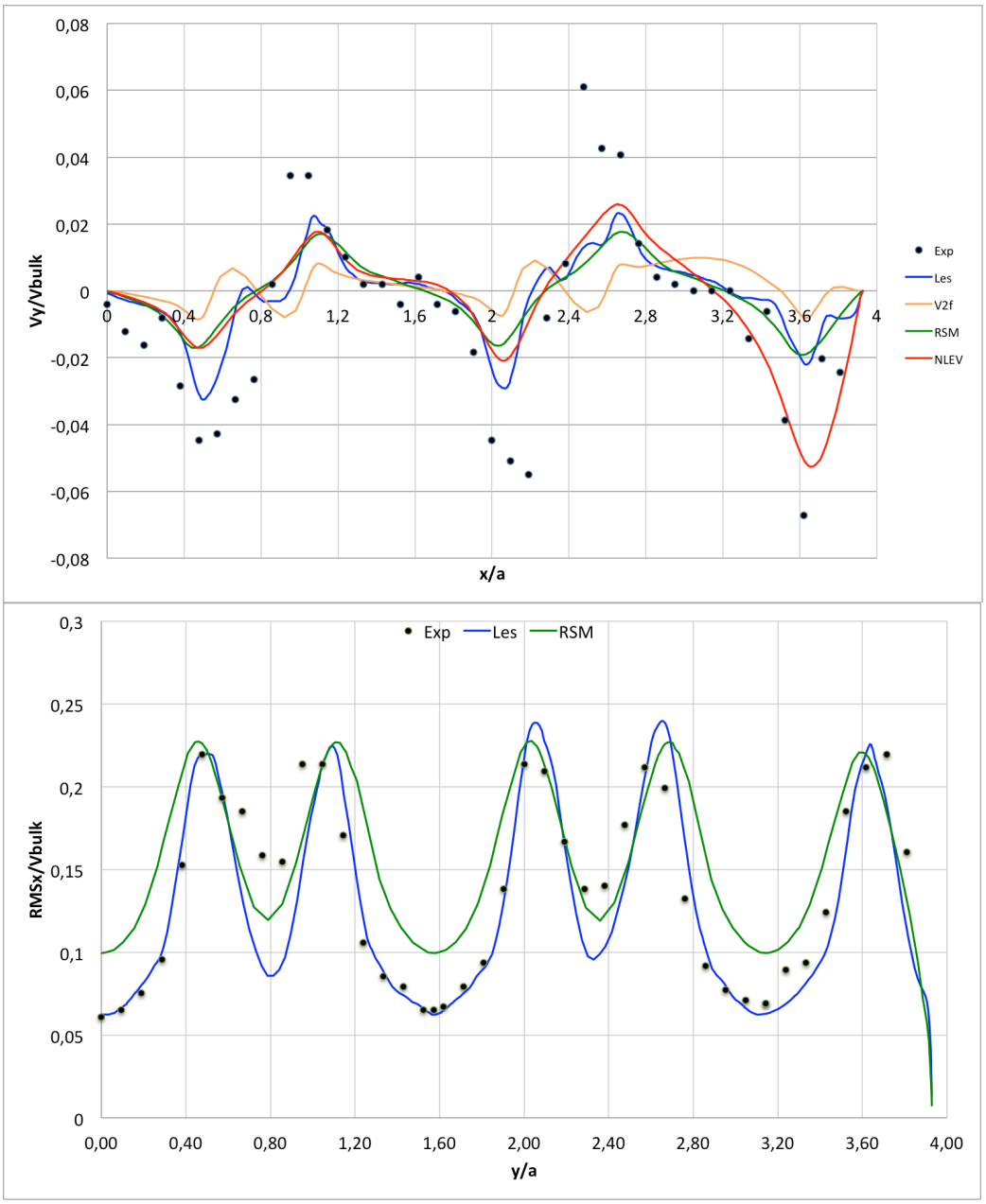

Graph. 4.36 Vy and RSMy on X_21_Yplus_Z0

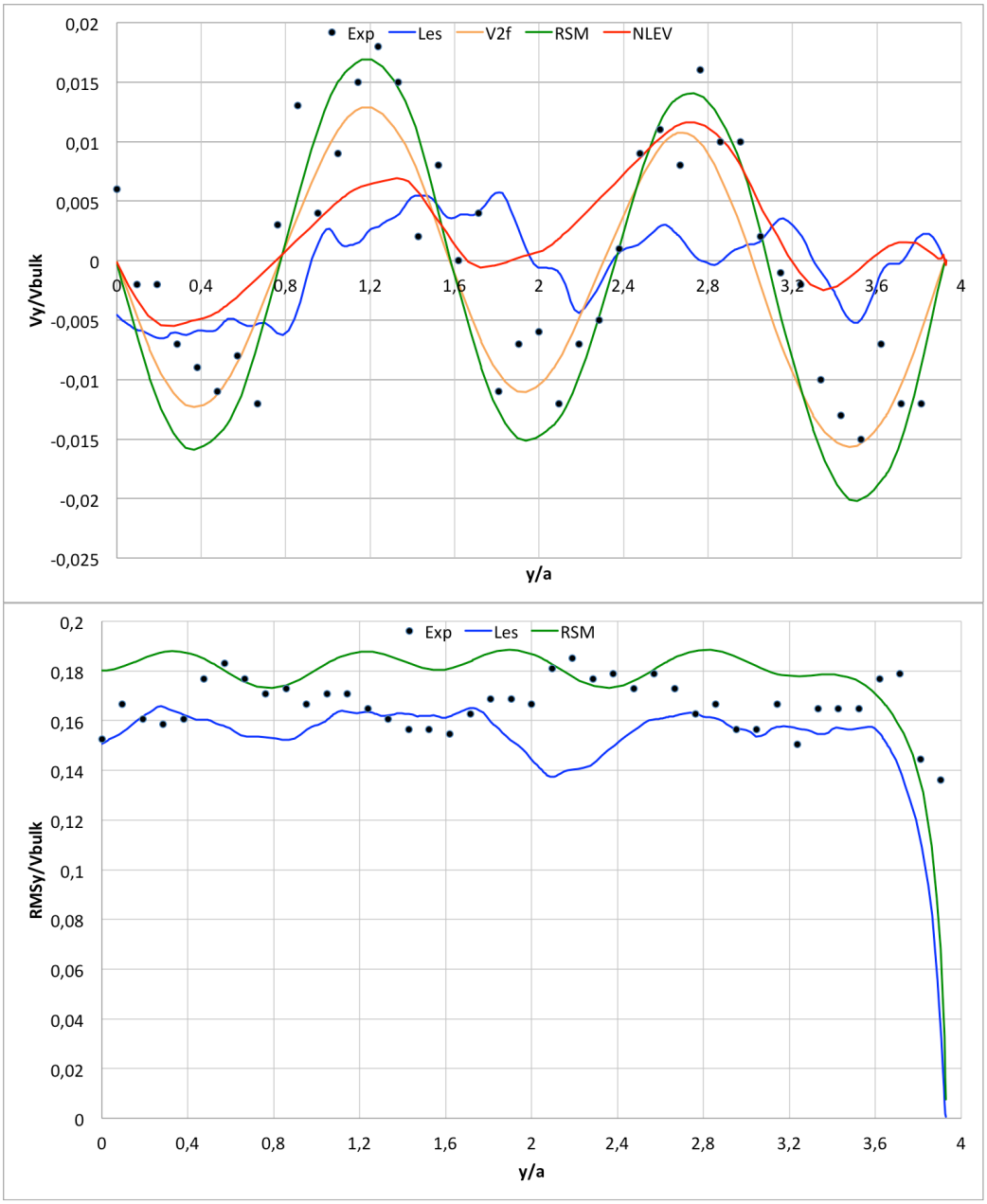

Graph. 4.37 Vy and RMSy at at X105_Yplus_Z0

Concerning the turbulence only RSM and LES provide results for RMS_i and so for the turbulence. The results show a good agreement with experimental data and except for a distance of 10D, the deviation is lower than 15% (Graph. (26-37)). Although the LES data are a little bit noisy, till 7D turbulence components match completely with the experimental results. RSM shows a large diffusion of turbulence near the wall which cause a large mismatching from the experimental data. Far from the inlet (10D) the deviation from the experimental data is lower for RSM probably due to the fact that LES reaches the equilbrium too early. Using $Q - creiterion$ for LES coherent structures could be represented. The structures do not present any strange decay before the value of 7D where the mismatching starts (Figure (4.3)). A finer grid is necessary to verify if it is not a problem of structure detection where the grid is too coarse (Graph (4.38)).

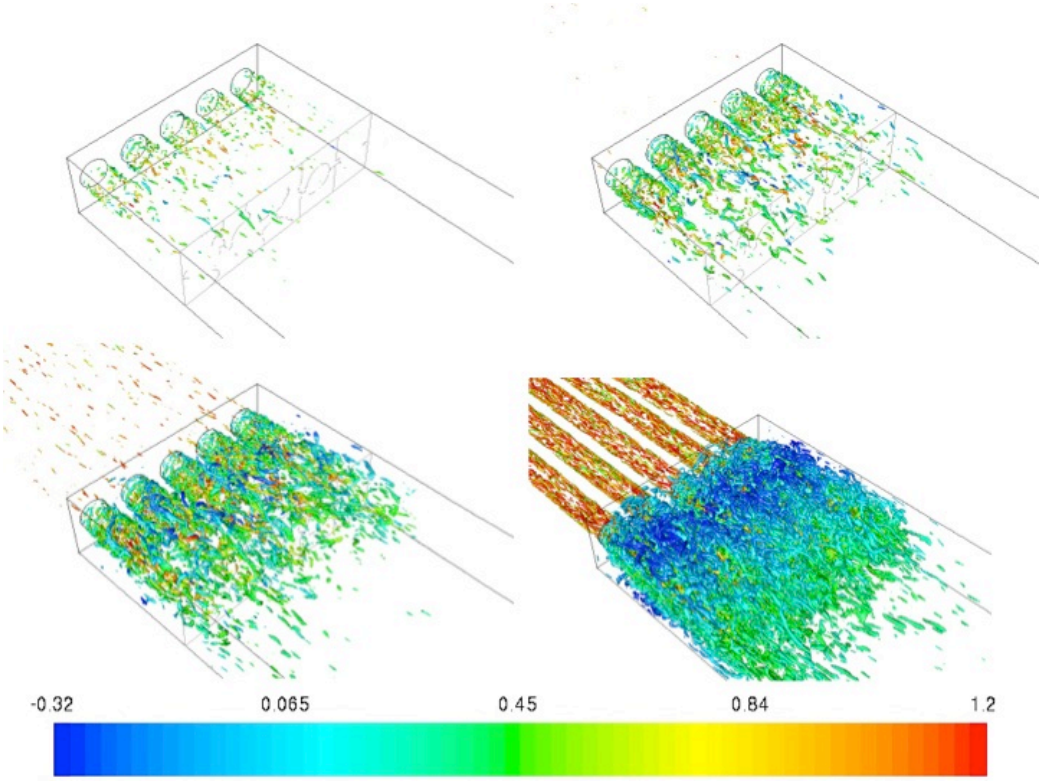

Figure 4.3 **Iso-surface of Q with value of 20000,10000 (top),5000 and 1000 (bottom).**

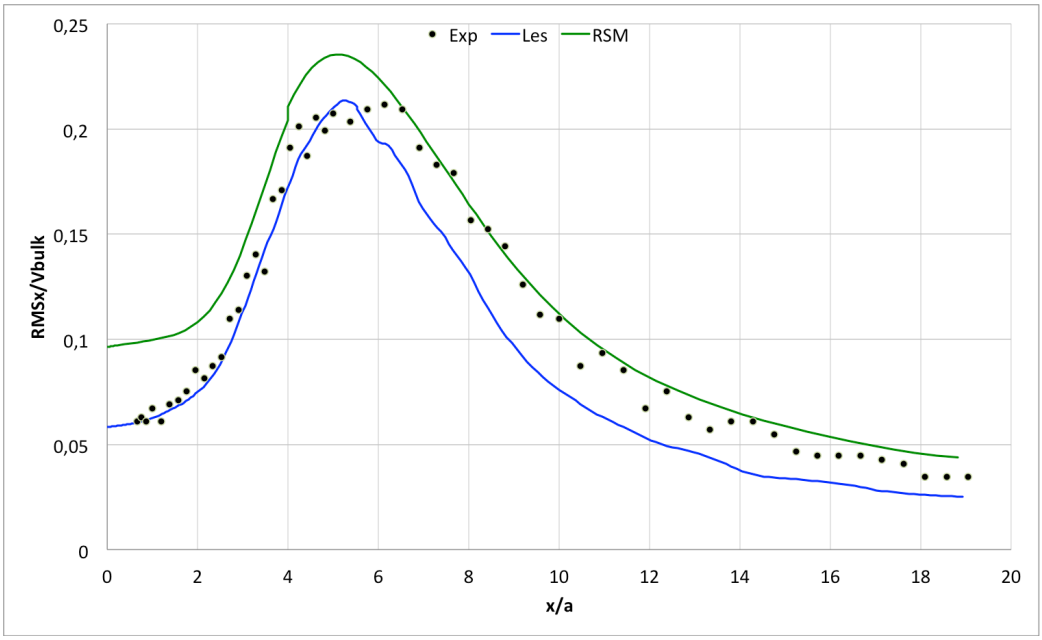

Graph. 4.38 RMSx Xall_Y0_Z0

Concerning toroidal structures, they are not clearly visible probably due to the strong interaction with the neighbor jet, however many filaments have an annulus disposition as represented in Figure (4.3) for $Q = 20000$.
This is confirmed by RMS_x of experimental data, *RSM* and *LES* (Fig.(4.4-5)).

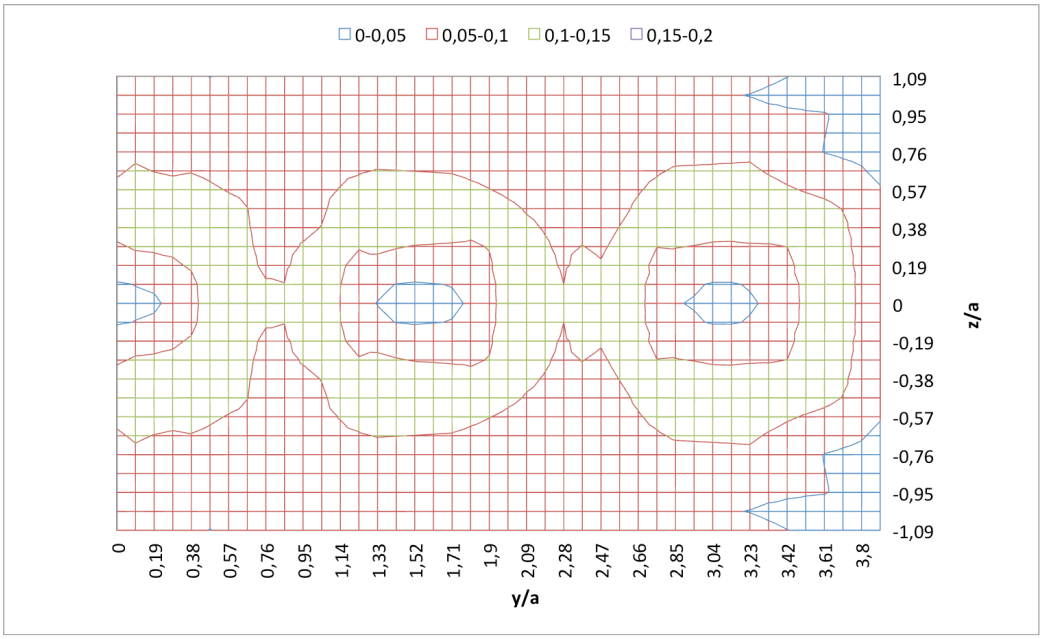

Figure 4.4 RMSx/Vbulk at 1D

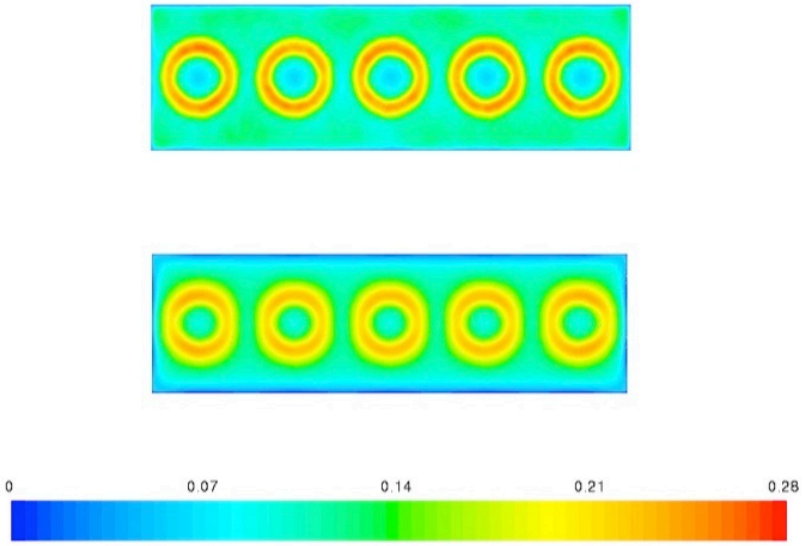

Figure 4.5 Countour of RMSx for LES (top) and RSM (bottom) at 1D

SUMMARY TABLE

$k-\omega\ SST$	Best model in predicting the initial recirculation and for the stagnation point. Over prediction of the core length and of the decay rate.
$k-\varepsilon\ RNG$	No convergence reached
V^2f	Over-prediction of the velocity on the center line but good replication of the velocity centerline gradient and of the spreading rate revealed also by the span-wise velocity replication. Combination and reattachment point are shifted downstream than experimental value. Over prediction for the recirculation extension.
$k-\varepsilon\ Low\ Reynolds$	Over prediction for the velocity decay and in general for merging zone. Over prediction for peak velocity in the pipe. Matching with experimental data for reattachment nut not for combination point.
$k-\varepsilon\ Low\ Reynolds\_2$	Over prediction for the velocity decay and in general for merging zone. Good prediction for peak velocity in the pipe. Matching with experimental data for reattachment but not for combination point.
$k-\varepsilon\ Realizable$	Mismatching with pipe peak velocity. Over prediction of velocity decay and of the punctual velocity. Good prediction for combination point.
$NLEV$	Good prediction of the core zone for the center line velocity but no prediction of stagnation point. Matching with stream-wise velocity on z-axis. Over prediction for the decay and combination point strongly anticipated.
RSM	Although the mismatching in pipe peak velocity prediction with experimental data, the best model in velocity prediction. Complete matching in center line stream wise velocity . Good prediction for spreading rate and for span-wise velocity. Fluctuations well predicted but a little bit smoother. No stagnation point predicted.
Les	Good prediction on velocity profile in the whole domain. Good prediction for reattachment, stagnation and combination point. Fluctuations perfectly predicted till 7D.

5. Conclusions

An experimental and numerical investigation on confined parallel jets has been performed. Concerning experimental results, the following have been obtained:

- The flow map shows a behavior which is coherent with the symmetric geometry configuration of the facility.
- The jet deflection, when existing, is very low and, consequently, the mass flow rate appears equally distributed along the domain.
- The geometry and the inlet conditions do not generate unstable operative conditions caused by multiple solutions.
- No oscillation till the value of 50 Hz is present.
- The decay law matches a hyperbolic law.

Concerning the numerical results compared with the experimental data:

- $k\varepsilon\ RNG$ model is the only method that has not reached the full numerical convergence.
- All the methods have shown a steady and symmetrical solution.
- No jet deflection has been detected.
- RSM, V^2f, Les and $NLEV$ have shown the best performance in decay prediction.
- The turbulent coherent structures are replicated well by *Les*. However, the level of turbulence is still high beyond $^{x}/_{a} = 7a$, but the model does not seem to be able to appreciate it.

A further investigation could be directed in the way of finding a model which could relate velocity decay K and other relevant parameters, like x_s and x_r, to geometrical and fluid dynamic operative conditions (Re_D, H and D_0).
In general, a Particle Image Velocimetry analysis could be performed in order to confirm qualitatively, but with a more global view, what revealed by LDV data.
Concerning the numerical simulations, a finer grid could be used for the *Les* analysis, in order to capture coherent structures beyond 7D.

References

1. A. P. Vourus, T. Panidis, Turbulent properties of a low Reynolds number, axisymmetric, pipe jet. *Experimental Thermal and Fluid Science* 44, 42 (2013).
2. G. Lipari, P. K. Stansby, Review of Experimental Data on Incompressible Turbulent Round Jets. *Flow, Turbulence and Combustion* 87, 79 (2011).
3. H. Fellouah, C. G. Ball, A. Pollard, Reynolds number effects within the development region of a turbulent round free jet. *International Journal of Heat and Mass Transfer* 52, 3943 (2009).
4. E. Tanaka, The interference of two-dimensional parallel jets (1st report). *Bullettin JSME* 13, 272 (1970).
5. A. Townsend, *The Structure of Turbulent Shear Flow*. (Cambridge University Press).
6. E. Tanaka, The interference of two-dimensional parallel jets (3rd report) *Bullettin JSME* 18, 1134 (1975).
7. E. Tanaka, The interference of two-dimensional parallel jets (2nd report). *bullettin JSME* 17, 920 (1974).
8. I. Wygnanski, H. E. Fielder, Some measurements in self preserving jet. *J. Fluid Mechanics* 38, 577 (1969).
9. L. Boguslawski, C. Popiel, Flow structure of the free round turbulent jet in the initial region. *J. Fluid Mechanics* 90, 531 (1979).
10. S. P. Capp, University of Buffalo (1983).
11. N. R. Panchapakesan, J.L. Lumley, Some measurements in the self preserving jet. *Journal of Fluid Mechanics* 246, 197 (1993).
12. J. Hussein, S. P. Capp, K. G. William, Velocity measurements in a high-Reynolds-number, momentum-conserving, axisymmetric, turbulent jet. *Journal of Fluid Mechanics* 258, 31 (1994).
13. T. G. Malmstrom, A. T. Kirkpatrick, B. Christensen, K. D. Knappmiller, Centreline velocity decay measurements in low-velocity axisymmetric jets. *Journal of Fluid Mechanics* 258, 31 (1994).
14. G. Xu, R. Antonia, Effect of different initial conditions on a turbulent round free jet. *Experiments in Fluids* 33, 677 (2002).
15. S. J. Kwon, W. Seo, Reynolds number effects on the behavior of a non-buoyant round jet. *Exp. Fluids* 38, 801 (2005).
16. S. B. Pope, *Turbulent Flows*. (Cambridge University Press).
17. P. E. Dimotakis, R. C. Miake-Lye, D. A. Papantoniou, Structure and dynamics of round turbulent jets. *Phys. Fluids* 26, 3185 (1983).
18. F. P. Ricou, D.B. Spalding, Measurements of entrainment by axisymmetric turbulent jets. *Journal of Fluid Mechanics* 11, 21 (1988).

19. M. Xu, A. Pollard, J. Mi, F. Secretain, H. Sadeghi, Effects of Reynolds number on some properties of a turbulent jet from a long square pipe. *Physics of Fluids* 25, 035102 (2013).
20. E. J. Smith, J. MI, G. J. Nathan, B. B. Dally, paper presented at the 15th Australasian Fluid Mechanics Conference The University of Sydney, Sydney, Australia, 13-17 December 2004.
21. J. Mi, D. S. Nobes, G. J. Nathan, Influence of jet exit conditions on the passive scalar field of an axisymmetric free jet. *Journal of Fluid Mechanics* 432, 91 (2001).
22. J. Lee, T. Lu, H. Sun, G. Miao, A novel formula to describe the velocity profile of free jet flow. *Archive of Applied Mechanics* 81, 397 (2010).
23. M. T. Kandakure, V. C. Patkar, A. W. Patwardhan, Characteristics of turbulent confined jets. *Chemical Engineering and Processing: Process Intensification* 47, 1234 (2008).
24. M. Miozzi, F. Lalli, G. P. Romano, Experimental investigation of a free-surface turbulent jet with Coanda effect. *Experiments in Fluids* 49, 341 (2010).
25. L. P. Chua, A. C. Lua, Measurements of a confined jet. *Physics of Fluids* 10, 31 (1998).
26. H. Schlichting, *Boundary layer theory*. (McGraw-Hill Inc., 1968).
27. N. K. Singh, K. Ramamurthi, Formation of Coanda jet from sharp-edged swirl nozzle with base plate. *Experimental Thermal and Fluid Science* 33, 675 (2009).
28. N. Asghar, J. C. S. Lai, paper presented at the Applications of Laser Techniques to Fluid Mechanics,10th International Symposium, Lisbon, 2000.
29. K. Murai, M. Taga, K. Akagawa, An experimental study of confluence of two dimensional jets. *Bullettin of JSME* 19, 958 (1976).
30. E. A. Anderson, R. E. Spall, Experimental and Numerical Investigation of Two-Dimensional Parallel Jets. *Journal of Fluids Engineering* 123, 401 (2001).
31. Y. F. Lin, M.J.Sheu, Investigation of two plane parallel unventilated jets. *Experiments in Fluids* 10, 17 (1990).
32. Y. F. Lin, M. J. Sheu, Interaction of parallel turbulent plane jets. *AIAA Journal* 15, 1756 (1991).
33. A. Durve, A. W. Patwardhan, I. Banarjee, G. Padmakumar, G. Vaidyanathan, Numerical investigation of mixing in parallel jets. *Nuclear Engineering and Design* 242, 78 (2012).
34. M. Nishimura, A. Tokuhiro, N. Kimura, Numerical study on mixing of oscillating quasi-planar jets with low Reynolds number turbulent stress and heat equation models. *Nuclear Engineering and Design* 202, 75 (2000).

35. R. F. Kunz, S. W. D'Amico, P. F. Vassallo, M. A. Zaccaria, LDV Measurement of Confined Parallel Jet Mixing. *Journal of Fluids Engineering* 123, 567 (2001).
36. T. P. Chiang, T. W. H. Sheu, S. K. Wang, Side wall effects on the structure of laminar flow over a plane-symmetric sudden expansion. *Computer & Fluid* 29, 467 (2000).
37. D. C. Wilcox, *Turbulence Modeling for CFD*. (DCW Industries, La Canada, 2006).
38. J. E. Bardina, O. G. Huang, T. J. Coakley, in *NASA Technical Memorandum 110446*. (Moffet Field, California, 1997).
39. T. N. Aziz, J. P. Raiford, A. A. Khan, Numerical Simulation of Turbulent Jets. *Engineering Applications of Computational Fluid Mechanics* 2, 234 (2008).
40. T. Jadhav, N. R. Panchapakesan, paper presented at the Proceedings of the 37th National & 4th International Conference on Fluid Mechanics and Fluid Power, Chennai, India, 16-18 December 2010.
41. C. Bogey, C. Bailly, Computation of the Self-Similarity Region of a Turbulent Round Jet Using Large-Eddy Simulation. *Direct and Large-Eddy SimulationVI* 10, 285 (2006).
42. S. Ghahremanian, B. Moshfegh, paper presented at the 20th AIAA Computational Fluid Dynamics Conference, Honolulu, Hawaii, 27-30 June 2011.
43. A. Balabel, W. A. El-Askary, On the performance of linear and nonlinear turbulence models in various jet flow applications. *European Journal of Mechanics - B/Fluids* 30, 325 (2011).
44. R. Mereu, E. Colombo, F. Inzoli, E. Merzari, H. Ninikata, paper presented at the ASME_ATI_UIT Conference on thermal and eviromental iussues in energy systems, Sorrento, Italy, 2010.
45. C. Y. Soong, P. Y. Tzeng, C. D. Hsieh, Numerical investigation of flow structure and bifurcation phenomena of confined plane twin-jet flows. *Physics of Fluids* 10, 2910 (1998).
46. D. Drikakis, Bifurcation phenomena in incompressible sudden expansion flows. *Physics of Fluids* 9, 76 (1997).
47. I. J. Sobey, P. G. Drazin, Bifurcation of Two-dimensional channel flows. *Journal of Fluid Mechanics* 171, 263 (2001986).
48. N. Allenborn, K. Nandakumar, H. Raszillier, F. Durst, Further contributions on the two-dimensional flow in a sudden expansion. *Journal of Fluid Mechanics* 330, 169 (1997).
49. S. Viaro, Politecnico di Milano (2012).
50. J. V. Beeck, C. Benocci. (Von Karman Institute, 2004-06).
51. P. Sagaut, *Large Eddy Simulation For Incompressible Flows*. Springer, Ed., (1998).

52. M. Lesieur, O. Metais, P. Comte, *Large-Eddy Simulations of turbulence*. (Cambridge university press, 2005).
53. R. Cucitore, M. Quadrio, A. Baron, *Eur. J. Mechanichs B/Fluids* 18, 261 (1999).
54. G. R. Tabor, M. H. Baba-Ahmadi, Inlet conditions for large eddy simulation: A review. *Computers & Fluids* 39, 553 (2010).